

**Strongly correlated spin-charge dynamics govern the
ultrafast response of ferromagnets**

by

Phoebe Marie Tengdin

B.A., Mount Holyoke College, 2013

M.S., University of Colorado, 2016

A thesis submitted to the
Faculty of the Graduate School of the
University of Colorado in partial fulfillment
of the requirements for the degree of
Doctor of Philosophy
Department of Electrical, Computer, and Energy Engineering
2019

This thesis entitled:
Strongly correlated spin-charge dynamics govern the ultrafast response of ferromagnets
written by Phoebe Marie Tengdin
has been approved for the Department of Electrical, Computer, and Energy Engineering

Prof. Margaret Murnane

Prof. Henry Kapteyn

Dr. Tom Silva

Date _____

The final copy of this thesis has been examined by the signatories, and we find that both the content and the form meet acceptable presentation standards of scholarly work in the above mentioned discipline.

Tengdin, Phoebe Marie (Ph.D., Electrical, Computer, and Energy Engineering)

Strongly correlated spin-charge dynamics govern the ultrafast response of ferromagnets

Thesis directed by Prof. Margaret Murnane

Ferromagnetic materials have strong electron correlations that drive quantum effects and make the physics that describes them extremely challenging. In particular, the electron, spin, and lattice degrees of freedom can interact in surprising ways when driven out of equilibrium by ultrafast laser excitation. In this thesis we explore several previously unexpected connections between electronic and spin systems in ferromagnetic materials. In both systems, dynamics occur at unexpectedly fast timescales, driven using femtosecond laser excitation pulses. The tools that we use to observe the exceeding fast (10s of femtosecond) dynamics are bursts of extreme ultraviolet light resonant with the M-edge of transition metals and produced via high harmonic generation. This technique has several distinct advantages over previously employed methods for studying ultrafast magnetic dynamics, and ultimately can uncover fundamentally new thing about these materials. In the first scientific result of this thesis, we combine time-resolved transverse magneto-optical Kerr effect (TMOKE) and time- and angle-resolved photoemission (ARPES) spectroscopies to show that the same critical behavior that governs the equilibrium magnetic phase transition in nickel also governs the ultrafast dynamics. When the electron temperature is transiently driven above the Curie temperature, we observe an extremely rapid change in the material response: The spin system absorbs sufficient energy within the first 20 fs to subsequently proceed through the phase transition, whereas demagnetization and the collapse of the exchange splitting occur on much longer, fluence- independent time scales of 176 fs. Following this finding, we observe that the transient electron temperature alone dictates the magnetic response of the system. The natural next question is whether or not a response on this timescale can be observed in any other materials. In the next part of this thesis I describe experiments on a half-metallic heusler compound, Co₂MnGe. Here we observe ultrafast transfer of spin polarization from one magnetic sublattice to

another within the timescale of the 55 fs laser excitation pulse. Ultrafast high harmonic pulses simultaneously probe the magnetic state of Co and Mn during laser excitation to make a surprising finding: the magnetization of Co is transiently enhanced, while that of Mn rapidly quenches. This observation marks the first direct manipulation of electron spins via light, thus providing a path towards spintronic logic devices such as switches that can operate on few femtosecond or even faster timescales.

Dedication

Stuff.

Acknowledgements

People were nice to me.

Contents

Chapter

1	Introduction	1
2	Ferromagnetism in Atoms, Molecules, and Solids	3
2.1	Introduction	3
2.2	Atom Based Description of Magnetism	4
2.2.1	Spin Dependent Atomic Hamiltonian (Pauli Equation)	4
2.2.2	Exchange Interaction	7
2.3	Electron Exchange in Molecules	10
2.3.1	Independent Electron Treatment	10
2.3.2	Heitler-London Treatment	12
2.3.3	Model Hamiltonians: Hubbard and Heisenberg models	15
2.4	Band Model of Ferromagnetism	18
2.4.1	Shortfall of the atomic picture: predicting the magnetic moment of the transition metal solids	18
2.4.2	Bragg scattering and Band structure	19
2.4.3	The Stoner Model	20
2.5	The next frontier: ultrafast laser-induced ferromagnet dynamics	23
3	Experimental Techniques	25
3.0.1	Resonant processes in magnetic materials	26

3.0.2	Intensity sum rule for charge	30
3.1	Kerr Effect	31
3.1.1	Transverse magneto-optical effect (TMOKE)	31
3.2	Interaction of matter with X-Ray radiation	32
3.3	High Harmonic Generation	32
4	Results of Nickel Experiment	33
4.1	Introduction	33
4.2	Results	34
4.3	Discussion	43
4.4	Materials and Methods	45
4.4.1	Experimental setups	45
4.4.2	Data analysis	46
4.4.3	Model of electronic and magnetic heat capacity	46
4.4.4	Statistical analysis	47
4.4.5	Details of experimental setups	47
4.4.6	Dynamics of electron temperature	51
4.4.7	Dynamics of the electron population at 1.6 eV	52
4.4.8	Dynamics of Exchange Splitting	54
4.4.9	Temperature dependence of exchange splitting in static ARPES	58
4.4.10	Method for extracting TMOKE asymmetry dynamics from HHG spectra	58
4.4.11	Momentum dependence of TMOKE Measurements	60
4.4.12	Transient electron and magnetic heat capacity	60
4.4.13	Effects of electron-phonon coupling and heat diffusion on Eq. 4.1	62
5	Quantitative Correlation of Extreme Ultraviolet Magneto-Optic and Photoemission Spectroscopies	66

6 Direct light-induced spin transfer between elemental sublattices in a spintronic Heusler material via femtosecond laser excitation	77
Bibliography	90

Tables

Table

Figures

Figure

2.1	Number of 3d and 4s electrons in the free transition metal atoms	18
2.2	Stoner Model for ferromagnetic transition metals, and illustration of terms used for the description of this model. The filled electron states (at zero temperature) below the Fermi energy E_F are shaded. The spin population with greater occupied states is called the majority band, while the population with less occupied states is called the minority band. The centers of the two bands are separated by the exchange energy Δ	21
4.1	Schematic of the critical behavior of ultrafast demagnetization in Ni. (A) After excitation by a femtosecond laser pulse above the critical fluence (F_c), the transient electron temperature (T_e) is driven above the Curie temperature (T_c), inducing high-energy spin excitations within 20 fs, which store the magnetic energy (see text). The Fermi-Dirac distributions of electrons are also plotted. Demagnetization occurs later, in 176 fs, driven by relaxation of nonequilibrium spins and the likely excitation of low-energy magnons. Full recovery of the spin system occurs within 500 fs to 76 ps, depending on the laser fluence. (B and C) Experimental setups for time-resolved ARPES and TMOKE, respectively, using ultrafast high-harmonic sources. IR, infrared.	35

4.3 Ultrafast charge dynamics in Ni. (A) Log plots of the photoemission intensity above EF for $F = 6 \text{ mJ/cm}^2$ and at different t_d , integrated from $k \approx 0.85 \text{\AA}^{-1}$ to $k \approx 1.3 \text{\AA}^{-1}$ in the momentum space. The dashed lines represent the fitting of the photoemission intensities with the Fermi-Dirac distribution convolved with experimental energy resolution (see the Supplementary Materials). Inset: Integrated photoemission intensity as a function of pump-probe time delay. The yellow dashed box illustrates the integration region of electron population in (B). (B) Dynamics of the electron temperature and the relative electron population (nn_0) within 0.2 eV above E_F as a function of t_d . The electron population is normalized to the band electron population (n_0) 0.2 eV below E_F (see the Supplementary Materials). (C) Comparison of the electron temperature [red dashed line, same as (B)] and the change of EUV transient reflectivity at a similar pump fluence. Inset: EUV transient reflectivity measurement. The resonant EUV light (65 eV) directly probes the charge dynamics around EF induced by the laser pump pulse. This measurement is averaged over k-space	39
--	----

4.4	Observation of multiple critical behaviors during ultrafast demagnetization in Ni.		
	(A) Peak electron temperature extracted 24 fs after excitation as a function of pump fluence. The open symbols represent the electron temperature extracted at different $k//$ using Tr-ARPES. The solid red line is the fit using Eq. 1 considering the transient electron and magnetic heat capacity [inset of (B)], whereas the green dashed line considers only the contribution from transient electron heat capacity (see the Supplementary Materials). The yellow-colored region (ΔF_S) is the energy transferred to the spin system within 20 fs.		
	(B) Change in the exchange splitting at 2 ps as a function of pump fluence. The red line represents a fit with an error function. The same critical fluence of $F_c \approx 2.8 \text{ mJ/cm}^2$ is observed for the exchange splitting collapse and the peak electron temperature in (A).		
	The transient electron heat capacity is plotted in the inset.		
	(C) Peak electron temperature calculated using Eq. 1 and $(C_e + C_m)$ Transient [inset of (B)] for the sample temperatures of 300 and 100 K. The red solid line is the same as in (A).		
	(D) Change of exchange splitting at 2 ps as a function of laser fluence at different sample temperatures. The solid lines represent the error function fit of the experimental results. The dashed lines align the critical fluences observed in (C) and (D) for different sample temperatures.		41
4.5	Experimental Setup.		
	(A) Experimental setup of Tr-ARPES experiment.		
	(B) Side band intensity as a function of pump-probe time delay in LAPE measurement for Tr-ARPES. The solid line is the fitting result with the Gaussian function with a FWHM of ≈ 42 fs.		50
	(C) Experimental setup of Tr-TMOKE experiment.		

4.6 Electron temperature fitting. (A) Photoemission spectrum of Ni(111) excited by 16 eV HHG photons at room temperature. The white dash-dotted lines represent the momentum range for the photoemission intensity in the analysis for the transient electron temperature. (B) and (C) Photoemission intensity and fitting results at $t_d = -500$ fs and $t_d = 24$ fs for $F \approx 6$ mJ/cm ² . The red solid lines are the fitting results using Eq. 4.4 and the blue dashed lines represent the DOS function used in the fitting. The black dashed-dot lines are the Fermi energy obtained from the fitting. (D) Photoemission intensity as a function of pump-probe time delay from the raw experimental data. (E) Same as (D), but the E_F shifts due to pump-induced space charge effects are corrected.	53
4.7 Electron population dynamics. (A) The relative change of photoemission intensity as a function pump-probe time delay, taking the intensity before pump excitation ($t_d = -500$ fs) as the reference. The yellow dashed boxes represent the two regions of energy where the changes of electron population are extracted. (B) Normalized electron population as a function of pump-probe time delay extracted from (a) and (b) regions in (A).	55
4.8 Analysis of exchange splitting. (A) and (B) Photoemission spectra of Ni(111) before ($t_d = -500$ fs) and after ($t_d = 500$ fs) pump excitation. The solid black boxes represent the regions the photoemission intensities are extracted for the analysis on the exchange splitting. (C)-(D) The photoemission intensities and the Voigt function fitting (Eq. S2) results for different pump fluences and different pump-probe time delays. The red lines are the overall fitting results. The Cyan, blue and green curves represent the extracted Voigt peaks for $m=1, 2$ (majority band) and 3 (minority band).	57
4.9 Global fitting of the exchange splitting dynamics. The global fitting results of the exchange splitting dynamics to Eq. 4.2 for a range of pump fluences ($F = 1.17$ mJ/cm ² to $F = 14.12$ mJ/cm ²).	59

4.10 Collapse of exchange splitting at the Curie temperature. (A) Static photoemission spectrum excited by He I α photons ($h\nu = 21.218$ eV) at the room temperature. Right panel: Energy distribution curve extracted at the momentum where the red dashed line is located. The exchange splitting (E_{ex}) can be clearly extracted using fitting procedure described in the previous section. (B) E_{ex} change reduces as the sample temperature increases.	59
4.11 Momentum dependence of TMOKE measurements. The TMOKE asymmetry dynamics for different crystal orientations. Inset: Illustrations of the relative orientations of the crystal cut relative to the directions of the magnetic field and light polarizations in the experimental geometry.	61
4.12 Electron and spin heat capacity. (A) The electron and magnetic heat capacity under thermal equilibrium (25). The solid line is the fitting result to Eq. (4) in the main text. (B) The transient electron and magnetic heat capacity extracted from our experimental results. The green line represents the contribution of the electron bath to the total heat capacity. The dashed line is the electron heat capacity under thermal equilibrium for comparison (25).	62
4.13 Two-temperature model. (A) The electron temperature measured using Tr-ARPES in comparison with the simulation results from TTM for the top 1nm thick layer of Ni with different pump fluence. (B) The transient EUV reflectivity results in comparison with the TTM simulation considering the average over a EUV probing depth of ≈ 10 nm. (C) The electron temperature simulated by TTM considering the situations: 1) thermally isolated, same as Eq. 4.1; 2) only heat diffusion; 3) heat diffusion + e-ph coupling. The dashed line represents the simulation results convolved with the experimental time resolution.	65

5.1 (a) Schematic of EUV ARPES and TMOKE measurements on Ni(111). The fluence profile of the laser excitation below the sample surface separates the magnetization response into two different regions (i) and (ii), depending on whether the in-situ fluence is above the critical fluence F_c . Using TR ARPES, the probed depth is on the order of a monolayer, while TR-TMOKE probes the entire laser-heated depth of ≈ 10 nm. (b) Schematic of the excitation present in the laser-induced phase transition in Ni when critical phenomena are taken into consideration [27]. When the laser fluence exceeds the critical fluence F_c , the electron temperature exceeds T_c and the sample rapidly undergoes a magnetic phase transition, as evidenced by multiple critical phenomena.	68
5.2 Change in the exchange splitting (ΔE_{ex}) in Ni measured using TR ARPES, for the absorbed laser fluence below ($0.21 \text{ mJ} = \text{cm}^2$, grey) and above ($1.7 \text{ mJ} = \text{cm}^2$, red) the critical fluence F_c . The solid lines are the fits to Eq. 5. Inset: Static ARPES spectrum plot along the Γ K direction recorded using He I_α photons.	69
5.3 Magnetization dynamics in Ni measured using TRTMOKE over a full range of laser fluences. The highest fluence is sufficient to fully suppress the sample magnetization. The data are offset for clarity. Red curves: Fits to our microscopic model which considers the critical behavior, as well as the depth-average effects in the TR-TMOKE measurements. Inset: Fluence-dependent amplitudes of the demagnetization and recovery processes directly extracted from the TR-TMOKE results. In the TR-TMOKE results, the magnetization $\langle M \rangle$ and the extracted amplitudes $\langle A_1 \rangle$, $\langle A_2 \rangle$, and $\langle A_3 \rangle$ are averaged over the entire probed depth (see text). The dashed yellow line highlights the linear relation of the amplitude $\langle A_3 \rangle$ to the absorbed fluence when the fluence is above the critical fluence.	71

- 5.4 (a) Top panel: Schematic magnetization of a ferromagnet as a function of temperature under thermal equilibrium with a single critical point (T_c). Bottom panel: Extracted amplitudes of the change of magnetization in a monolayer of Ni as a function of in-situ fluence and heat source. The correspondence of T_c to the two critical fluences (F_c and F_c') is highlighted. (b) The laser-induced magnetization variation in Ni as a function of time and depth. The black dashed lines represent the contours of equal magnetization. The white dashed lines separate different regions for the in-situ fluence relative to the two critical fluences F_c and F_c' . (c) The relative contributions of the fast ($\langle A_3 \rangle$) recovery process directly extracted from the TR-TMOKE results in Fig. 5. Inset: Potential scenarios for the coexistence of ferromagnetic and paramagnetic phases in different fluence regions. 76

6.1 (A) Representation of spin dynamics in Co ₂ MnGe. Before excitation, Mn atoms (orange arrows) have a 3x larger magnetic moment than Co atoms (blue arrows), which are 2x more abundant in the bcc lattice. The purple arrow represents the net magnetic moment of the compound. Upon excitation, the Mn moment begins to decrease and the Co magnetic moment immediately grows by 10%. This occurs within the duration of the pump pulse. Hundreds of femtoseconds later, the Mn and Co atomic spins become disordered, and the angular momentum begins to transfer to the lattice. The net magnetic moment begins to decrease. After 1-2 ps, the spins have reached their maximum quenching. (B) Schematic of the experimental apparatus. Ultrafast femtosecond infrared pulses are used to excite the sample, while the magnetization dynamics are tracked with femtosecond EUV pulses recorded on a spectrometer. (C) Density of states for each element in the half metal. Note that the minority spin channel is gapped, with no available states at the Fermi level for the minority channel. Critically, this gap is larger for Mn than for Co. After excitation, the conduction band states are hybridized, as illustrated by the shared red wavefunction.	80
---	----

6.2 Element resolved ultrafast magnetization dynamics following excitation by femtosecond laser in the (A) half-metallic B2 phase. Note that the Co magnetization increases as the Mn decreases, followed by a lag of 100 fs between the demagnetization of the Co and Mn sublattices. Inset: Dynamics of ultrafast spin transfer. Solid lines are the element specific dynamics after excitation by a 55 fs (full width half maximum) pump pulse. Dashed lines indicate the dynamics after excitation by a 90 fs pump pulse. Note that the location of the peak of the enhancement is shifted in time by 25 fs for the enhancement driven by a 90 fs pump (half the difference between the duration of the two pulses), underlining that this process is a direct optical manipulation.	82
(B) Element resolved ultrafast magnetization dynamics in the non half-metallic A2 phase. There is no enhancement of the Co magnetization. The subsequent lag in demagnetization dynamics between the Co and Mn sublattices decreases to 57 fs.	
(C) Atomic structure of compounds studied. In the B2 phase, the Co atoms have ordered so that they occupy sites at the edges of the bcc structure, while the centers are randomly interspersed between Mn and Ge. In the A2 phase, the material has formed the ordered bcc structure, but the location of the atoms within the structure are random.	
6.3 Density of states for Co ₂ MnGe in the (A) B2 and (B) A2 phases. Note that the half-metallic character is only present in the B2 phase.	85

- 6.4 The probability for exciting a spin up (majority) vs. spin down (minority) electron from the valence band in the B2 phase for different pump energies in (A) Mn sites. Note that for a 1.55 eV pump, the probability is higher for spin up electrons to be excited from Mn. (B) Probability for excitations in Co sites. In contrast to the Mn result, the probability is higher for minority electrons to be excited in Co. (C) Illustration of process that leads to direct optical transfer of spin polarization from Mn to Co. The initial state wavefunction is hybridized and composed of both Mn and Co d-states, with a larger contribution from the Mn atom. In the final state, the situation is reversed, and the Co d-states dominate. Hence, when an electron is optically excited from the initial to the final state wavefunction, this is associated with a transfer of spin polarization from Mn to Co. 86

Chapter 1

Introduction

This thesis makes the bold attempt to utilize a new and emerging technology: coherent extreme ultraviolet light generated via high harmonic generation to study the fundamental science behind magnetism. Coherent light at short wavelengths (and thus high photon energies) has proven to be extremely useful for a variety of applications and fundamental science. In this thesis, coherent light that is resonant with ferromagnetic elements is used to probe dynamics that occur at extremely short (femtosecond) timescales.

In Chapter 1, we develop the motivation for this work, based on the current state of understanding in ferromagnetism and the broader context of highly correlated condensed matter systems. Chapter 2 provides a first-order theoretical description of the modern day understanding of ferromagnetism: beginning from the atomic picture of the He atom, and proceeding to the simplest molecular description. Here we will describe the two most commonly used Hamiltonians in solid state physics: the Heisenberg and Hubbard Hamiltonians, and discuss which specific situations warrant the use of either picture. We also provide an introduction into the difficulty of solving the complicated many-body systems studied in this thesis. In Chapter 3, provides a theoretical background for the light-matter interaction in the context of magnetism in solids. We show how characterization techniques based on high harmonic generation (HHG) have the unique opportunity to uncover new insights into the physics of these challenging systems. We describe the experimental apparatus used for most of the work in this thesis, along with how we generate the very special extreme ultraviolet (EUV) light that is central to this work. Next, in Chapters 4-6 we describe

several of the experiments performed with our setup and the insights into fundamental scientific questions uncovered. We conclude with an outlook on some future experiments to be continued by the current and future members of the magnetism team in the KM Group.

Chapter 2

Ferromagnetism in Atoms, Molecules, and Solids

2.1 Introduction

The topic of magnetism is truly so broad that it is far beyond the reach of a doctoral dissertation to give a thorough theoretical grounding in the concepts involved. This fact is underlined by the lack of the existence of a complete ab-initio theory of magnetism. In addition, the topic of electron-electron correlations and how they impact the traditional understanding of condensed matter systems is a rapidly developing field that deserves a treatment of its own, but is also relevant to the materials' studied here. However, in this chapter we will attempt to outline the basic theoretical concepts that provide a qualitative understanding of magnetic phenomena.

We begin with the electronic and magnetic structure of atoms and simple molecules in order to provide an intuitive theoretical basis for the more complicated description of magnetism in solids to follow. We will show that the fundamental magnetic properties that emerge from a description of 2 electron systems such as the He atom or the H_2 molecule form the basis for our modern understanding of magnetism. Even at the molecular stage, the difficulty of treating the interactions between electrons and solving the complete Hamiltonian without significant approximations becomes apparent. Indeed, the problem quickly becomes intractable for a many-body system. However, in this section we provide several techniques and approximations for understanding the 2-electron system that have been shown to work well under various specific situations.

This section will also highlight one of the primary dilemmas in modern day magnetism research: whether to treat the electrons in the system as localized and correlated, or delocalized

and uncorrelated. We discuss which approximate solutions and the corresponding wavefunctions provide a more accurate description for the two scenarios, and which physical situations give rise to them. This key property of ferromagnets is also a topic of intense debate within the field of ultrafast ferromagnetism, and our particular studies that probe which picture is better suited for ferromagnetic nickel will be discussed in more detail in chapters 4 and 5.

The atomic and molecular description is then followed by a band theory of magnetism, first treating a single electron within a periodic potential (the crystal lattice), and progressing to the Stoner model, which forms the basis for much of our modern day understanding of magnetism.

2.2 Atom Based Description of Magnetism

We will begin from the simplest system with electron-electron interactions, the He atom, and show that the basic concept of exchange can be derived from this system, and thus arises in a very fundamental way from the interaction of two electrons in a single potential. The exchange interaction is the largest force in magnetism, and provides an origin for the observed alignment of spins in a ferromagnet.

2.2.1 Spin Dependent Atomic Hamiltonian (Pauli Equation)

Although the subject of this thesis is about strongly correlated spin-charge electron-electron interactions, we must first begin by understanding what magnetism looks like without including any strong correlations between electrons and their spins. We do this here by constructing the spin dependent atomic Hamiltonian. To properly treat the electronic and spin structure of electrons, we cannot use the Schrödinger equation, since it does not include spin. Instead, we begin from the time-independent Pauli equation (stohr ref 197):

$$[\mathcal{H}_e + \mathcal{H}_s] + \psi(r, t) E \psi(r, t) \quad (2.1)$$

with \mathcal{H}_e the term responsive for the electronic interaction at origin R=0, nuclear charge

$q_n=Ze$ and electrons have a charge $q_e=-e$:

$$\mathcal{H}_e = \sum_{i=1}^N \left(\frac{p_i^2}{2m_e} - \frac{Ze^2}{4\pi\epsilon_0|r_i|} \right) + \sum_{i < j} \frac{e^2}{4\pi\epsilon_0|r_j - r_i|} \quad (2.2)$$

The terms in this hamiltonian correspond respectively to the kinetic energy, Coulomb interaction with the nucleus, and Coulomb interaction between electrons. The last term is responsible for the exchange interaction, as we will discuss later. The second term in the Pauli equation 2.1 corresponds to the spin energy of the electrons:

$$\mathcal{H} = \frac{e\hbar}{m_e} S \cdot B^* \quad (2.3)$$

With S the atomic spin and B^* the magnetic induction. This term ultimately gives rise to the spin-orbit interaction.

In order to solve the complicated system described by this hamiltonian, we need to make some important (and hopefully justified) simplifications. We will first address H_e , which we immediately see has terms that come from the electron's interaction with the nucleus, and it's interaction with other electrons. Thus, we would like to re-write this hamiltonian in two parts: first as a spherically symmetric problem that contains only single electron operators, and will eventually lead to solutions in the form of Bohr's atomic shell model, and the second a perturbative term corresponding to two-electron operators. Although this simplification may not hold for all cases, we will attempt this anyways, in order to gain a tractable solution to the problem in certain cases.

Since the single electron Coulomb term is negative, while the two-electron term is positive, we can write the problem as a central field felt by the electron combined with a "screening" term that is felt by the electron-electron interaction.

Thus we rewrite Eqn. 2.2:

$$\mathcal{H}_e = \sum_i \mathcal{H}^0(r_i) + \mathcal{H}^1 \quad (2.4)$$

with

$$\mathcal{H}^0(r_i) = \frac{p_i^2}{2m_e} - \frac{Ze^2}{4\pi\epsilon_0|r_i|} + \frac{e^2}{4\pi\epsilon_0} \overline{\sum_{j(j \neq i)} \frac{1}{|r_j - r_i|}} \quad (2.5)$$

which is the sum of all one-electron (non-perturbative) terms (note that the last term is an average strength of the electron-electron interaction, and thus does not depend on the individual positions at a given point and time). The second (perturbative) term \mathcal{H}^1 can then be written as a difference between two large terms and is thus "small" compared to \mathcal{H}^0 :

$$\mathcal{H}^1 = \frac{e^2}{4\pi\epsilon_0} \left(\sum_{i < j} \frac{1}{|r_j - r_i|} - \overline{\sum_{i,j(i \neq i)} \frac{1}{|r_j - r_i|}} \right) \quad (2.6)$$

This formalism, called the central field Hamiltonian, decouples individual electrons from each other, positions of each electron are not correlated to the position of any other electron. We can now solve the three dimensional Schrödinger equation for \mathcal{H}^0 , and obtain the single electron eigenfunctions which are composed of a radial part and spherical harmonics:

$$\psi_{n,l,m}(r) = R_{n,l}(r)Y_{l,m}(\theta, \phi) \quad (2.7)$$

In practice, however, the solutions to this Hamiltonian are nontrivial and usually calculated self consistently by starting with an approximate parameterized solution which is then optimized according to additional criteria. Additionally, these solutions are incomplete, since they do not include spin. The complete spin-orbitals must be eigenfunctions of the central field Hamiltonian in order for us to use them as our zero-order function for the full perturbative solution of the Pauli equation (Eqn 2.1). We specify the direction of the spin relative to the z-axis, using the one electron spin functions $\alpha = (s_z = +1/2)$ and $\beta = (s_z = -1/2)$. The spin dependence is then characterized as $\chi(s_z)$ and the final one electron spin orbitals are written as:

$$\Psi(a) = \Psi(r, s) = R_{n,l}(r)Y_{l,m}(\theta, \psi)\chi(s_z) \quad (2.8)$$

Although we do not here show the solutions for these wavefunctions, this treatment of the problem for the two-electron atom should give the reader some concept for the fundamental forces

involved in the problem of magnetism, and the difficulty of finding solutions even on an atomic scale.

2.2.2 Exchange Interaction

Next, we will show how this formalism can be used to understand the exchange interaction in He, the simplest atomic species with two unpaired electrons. The Schrödinger equation for helium is represented by the Hamiltonian (for Z=2):

$$\mathcal{H}(r_1, r_2) = \frac{p_1^2}{2m_e} + \frac{p_2^2}{2m_e} - \frac{2e^2}{4\pi\epsilon_0|r_1|} - \frac{2e^2}{4\pi|r_2|} + \frac{e^2}{4\pi|r_2 - r_1|} \quad (2.9)$$

where the first four terms can be grouped together and written as the central field portion, $\mathcal{H}^0(r_1, r_2)$, while the final term is the two electron part $\mathcal{H}_{e-e}(r_1, r_2)$. This method given by Sakuri [1]. We know that the final solutions of $\mathcal{H}^0(r_1, r_2)$ must be anti-symmetric. We begin from the ground state of helium, with both electrons occupying the 1s orbital. Here the spatial wavefunction is symmetric since both electrons are in the same orbital with the quantum numbers nlm=100. Thus the spin wavefunction must be antisymmetric, with each electrons having the different spin functions α and β . The ground state wavefunction is written as:

$$\Psi_{gs}(a, b) = \Psi_{sym}(r_1, r_2)\chi_{as}(s_1, s_2) \quad (2.10)$$

$$= \frac{1}{2}[\Psi_{100}(r_1)\Psi_{100}(r_2) + \Psi_{100}(r_1)\Psi_{100}(r_2)][\alpha\beta - \beta\alpha] \quad (2.11)$$

with solutions:

$$\mathcal{H}^0(r_1, r_2)\Psi_{gs}(a, b) = E_0\Psi_{gs}(a, b) \quad (2.12)$$

that give the zeroth order ground state energy E_0 , which must be corrected by $\mathcal{H}_{e-e}(r_1, r_2)$, which can be calculated from perturbation theory:

$$E_1 = \langle \Psi_{gs}(a, b) | \mathcal{H}_{e-e}(r_1, r_2) | \Psi_{gs}(a, b) \rangle \quad (2.13)$$

The exact calculation of these energies can be found in Sakuri ([1]). The solutions are that $E_0 = -4e^2/(4\pi\epsilon_0 a_0)$ and $E_1 = +5e^2/4(4\pi\epsilon_0 a_0)$, with a_0 with Bohr radius. Notably, E_0 and E_1 have comparable sizes, and thus both need to be considered to obtain an energy that compares well to the experimental one of 79.01 eV. This calculation of the ground state energies can actually be carried out without the inclusion of spin (it enters in only in the anti-symmetrization of the spin states).

However, the importance of the anti-symmetrization requirement and inclusion of spin really comes into play for the calculation of excited states in helium. This calculation will give us a fundamental insight into the concept of exchange.

We begin with one electron in the 1s orbital, $nlm=100$ and the second electron in an excited state that has a general form of nlm . For this second electron, the central field wavefunction can either be symmetric or antisymmetric. For the antisymmetric case, we have the singlet excited state:

$$\Psi_{es}^S(a, b) = \frac{1}{\sqrt{2}}[\Psi_{100}(r_1)\Psi_{nlm}(r_2) + \Psi_{100}(r_2)\Psi_{nlm}(r_1)]\chi_{as}(s_1, s_2) \quad (2.14)$$

where the spin contribution $\chi_{as}(s_1, s_2)$ is given as:

$$\chi_{as}(s_1, s_2) = \frac{1}{\sqrt{2}}[\alpha\beta - \beta\alpha] \quad (2.15)$$

And in the antisymmetric space case we have the triplet excited state:

$$\Psi_{es}^T(a, b) = \frac{1}{\sqrt{2}}[\Psi_{100}(r_1)\Psi_{nlm}(r_2) + \Psi_{100}(r_2)\Psi_{nlm}(r_1)]\chi_{sym}(s_1, s_2) \quad (2.16)$$

and the triplet state spin wavefunction $\chi_{sym}(s_1, s_2)$ given as

$$\chi_{sym}(s_1, s_2) = \begin{cases} \alpha\alpha \\ \frac{1}{\sqrt{2}}[\alpha\beta + \beta\alpha] \\ \beta\beta \end{cases}$$

The two solutions 2.14 and 2.16 have degenerate energies: $E_{es} = E_{100} + E_{nlm}$. However, the perturbative contribution to the two states is not identical. For the singlet (antiparallel spin alignment) state we have:

$$E_{e-e}^S = \langle \Psi_{es}^S(a, b) | \mathcal{H}^1(r_1, r_2) | \Psi_{es}^S \rangle = I + J \quad (2.17)$$

and for the triplet (parallel alignment):

$$E_{e-e}^T = \langle \Psi_{es}^T(a, b) | \mathcal{H}^1(r_1, r_2) | \Psi_{es}^T \rangle = I - J \quad (2.18)$$

and the energy splitting between the two states is given by:

$$E_{e-e}^S - E_{e-e}^T = 2J \quad (2.19)$$

To understand this splitting we need to know what the energies I and J correspond to. These can be evaluated using the orthogonality of the radial, angular and spin wavefunctions. The electron-electron Hamiltonian $\mathcal{H}(r_1, r_2)$ does not depend on spin, and thus the matrix elements of 2.17 and 2.18 are determined by the orthogonality of α and β . We have $\langle \pm \frac{1}{2} | \pm \frac{1}{2} \rangle = 1$ and $\langle \pm \frac{1}{2} | \mp \frac{1}{2} \rangle = 0$ and we can obtain:

$$I = \int \int |\Psi_{100}(r_1)|^2 \frac{e^2}{4\pi\epsilon_0 r_{12}} |\Psi_{nlm}(r_2)|^2 dr_1 dr_2 \quad (2.20)$$

$$J = \int \int \Psi_{100}(r_1) \Psi_{nlm}(r_2) \frac{e^2}{4\pi\epsilon_0 r_{12}} \Psi_{100}^*(r_2) \Psi_{nlm}^*(r_1) dr_1 dr_2 \quad (2.21)$$

Finally these expressions have a physical meaning. The term I is the Coulomb integral, and it is the electrostatic Coulomb repulsion between the electron densities $|\Psi_{100}(r_1)|^2$ and $|\Psi_{nlm}(r_1)|^2$

and has a positive sign, which is opposite to the negative attractive force of the electron-nuclear Coulomb force. The second quantity J is the exchange integral, and it represents the energy cost associated to switching two electron's quantum states with each other. In the singlet state the spatial wavefunction is symmetric and thus electrons will be closer together, giving it an electrostatic repulsion that is larger than in the triplet state, where the wavefunction is antisymmetric and electrons will be farther apart. Thus the effect of electrostatic repulsion is greater in the singlet state and it will be higher in energy, and this energy difference is the $\Delta E = 2J$, the singlet-triplet splitting.

We see now that the exchange interaction arises from two main factors: the Coulomb repulsion between two electrons, and the requirement of a total antisymmetric wavefunction, due to the Pauli exclusion principle. With these two ingredients we can understand the concept of exchange interaction, and furthermore we can distinguish between systems for which symmetrization leads to either parallel or antiparallel spins. For He, J is positive, and the spins point into the same direction, parallel to each other. However for H_2 , J is negative, giving rise to antiparallel alignment of spins.

2.3 Electron Exchange in Molecules

We now take the next step and move to a description of the exchange interaction in molecules, beginning from the simplest case, an H_2 molecule.

2.3.1 Independent Electron Treatment

We begin with the independent electron (IE) approximation; first considering a one-electron H_2^+ model and then adding a second electron. The Hamiltonian for the H_2^+ molecule is:

$$\mathcal{H}(r) = \frac{p^2}{2m_e} - \frac{e^2}{4\pi\epsilon_0} \frac{1}{|r - R_1|} + \frac{e^2}{4\pi\epsilon_0} \left[-\frac{1}{|r - R_1|} + \frac{1}{R_1 - R_2} \right] \quad (2.22)$$

here the first two terms are the central field hamiltonian for a single hydrogen atom: \mathcal{H}_{atom} , and the coordinates R_1 and R_2 correspond to the positions of the ions in the H_2^+ atom. Solutions

of this equation can be obtained from the solutions of the Schrödinger equation for separate H atoms. The one-electron atomic wavefunctions for the H atoms are given as $\phi_1(r)$ and $\phi_2(r)$ and from these we can construct normalized molecular orbital wavefunctions from linear combinations of these single electron solutions. We first define an overlap integral O:

$$O = \langle \phi_1 | \phi_2 \rangle \quad (2.23)$$

And then we construct the linear combination atomic orbitals (LCAO) or tight-binding wavefunctions (bonding and anti-bonding):

$$\Psi_B(r) = \frac{1}{\sqrt{2(1+O)}}(\phi_1(r) + \phi_2(r)) \quad (2.24)$$

$$\Psi_{AB}(r) = \frac{1}{\sqrt{2(1-O)}}(\phi_1(r) - \phi_2(r)) \quad (2.25)$$

These two wavefunctions have the eigenvalues:

$$\epsilon_B = \frac{E_0 + E_{12}}{1 + O} \quad (2.26)$$

$$\epsilon_{AB} = \frac{E_0 + E_{12}}{1 - O} \quad (2.27)$$

With the quantities E_0 and E_{12} the atomic energy and interaction energy, respectively:

$$E_0 = \langle \phi_1 | \mathcal{H}(r) | \phi_1 \rangle = \langle \phi_2 | \mathcal{H}(r) | \phi_2 \rangle \quad (2.28)$$

$$E_{12} = \langle \phi_1 | \mathcal{H}(r) | \phi_2 \rangle = \langle \phi_2 | \mathcal{H}(r) | \phi_1 \rangle \quad (2.29)$$

If the atoms are pushed very close together, the overlap becomes unity, and the bonding function becomes the ground state function, however as the distance between atoms becomes large, the interaction energy and overlap integral decay exponentially to zero, and the two energies become proportional to each other with opposite sign.

2.3.2 Heitler-London Treatment

Now, we consider the two-electron H_2 molecule. The Hamiltonian is written as:

$$\mathcal{H}(r_1, r_2) = \frac{p_1^2}{2m_e} - \frac{e^2}{4\pi\epsilon_0} \frac{1}{|r_1 - R_1|} + \frac{p_2^2}{2m_e} - \frac{e^2}{4\pi\epsilon_0} \frac{1}{|r_2 - R_2|} \quad (2.30)$$

$$+ \frac{e^2}{4\pi\epsilon_0} \left[-\frac{1}{|r_1 - R_2|} - \frac{1}{|r_2 - R_1|} + \frac{1}{|r_1 + r_2|} + \frac{1}{|R_1 - R_2|} \right] \quad (2.31)$$

This Hamiltonian contains terms for the kinetic energy of each electron, the individual electron-nucleus Coulomb terms, and finally a term for the electron-electron interactions. In order to find a solution, we can first try an independent electron model, drop the electron-electron interaction term: $\mathcal{H}_{e-e} = -e^2/4\pi\epsilon_0|r_1 - r_2|$. Re-written in this way we have:

$$\mathcal{H}(r_1, r_2) = \frac{p_1^2}{2m_e} - \left[\frac{e^2}{4\pi\epsilon_0} \frac{1}{|r_1 - R_1|} + \frac{1}{|r_1 - R_2|} \right] \quad (2.32)$$

$$+ \frac{p_2^2}{2m_e} - \left[\frac{e^2}{4\pi\epsilon_0} \frac{1}{|r_2 - R_2|} + \frac{1}{|r_2 - R_1|} \right] \quad (2.33)$$

$$+ \frac{e^2}{4\pi\epsilon_0} \frac{1}{|R_1 - R_2|} \quad (2.34)$$

Now the solutions of this Hamiltonian can be expressed as one electron LCAO wavefunctions as outlined in the previous section. However, we are still missing one more piece, the symmetrization postulate for a two-electron system. We can use the spin wavefunctions described in section 2.2.2 to write the two electron singlet ground state:

$$\Psi^S(r_1 s_1; r_2 s_2) = \frac{1}{\sqrt{2}} [\Psi_B(r_1)\Psi_B(r_2) + \Psi_B(r_2)\Psi_B(r_1)] \chi_{as}(s_1, s_2) \quad (2.35)$$

And the triplet state solution is created from the singlet spin state and the products of both bonding and antibonding LCAO wavefunctions:

$$\Psi^T(r_1 s_1; r_2 s_2) = \frac{1}{\sqrt{2}} [\Psi_B(r_1)\Psi_{AB}(r_2) - \Psi_B(r_2)\Psi_{AB}(r_1)] \chi_{sym}(s_1, s_2) \quad (2.36)$$

Next we insert Eqns. 2.24 and 2.25 into Eqns. 2.35 and 2.36 and renormalize by the double overlap integral S :

$$S = \langle \phi_1(r_1)\phi_2(r_2) | \phi_1(r_2)\phi_2(r_1) \rangle \quad (2.37)$$

we can rewrite the singlet state solution as:

$$\Psi_{IE}^S = \frac{1}{2\sqrt{1+S}} [\phi_1(r_1)\phi_2(r_2) + \phi_2(r_1)\phi_1(r_2)][\alpha_1\beta_2 - \beta_1\alpha_2] \quad (2.38)$$

$$+ \frac{1}{2\sqrt{1+S}} [\phi_1(r_1)\phi_1(r_2) + \phi_2(r_1)\phi_2(r_2)][\alpha_1\beta_2 - \beta_1\alpha_2] \quad (2.39)$$

and the triplet state as:

$$\Psi_{IE}^T = \frac{1}{\sqrt{2(1-S)}} [\phi_2(r_1)\phi_1(r_2) - \phi_1(r_1)\phi_2(r_2)]\chi_{sym} \quad (2.40)$$

Now we need to check that these states behave in a physically reasonable manner when the limits of the atoms being close together or far apart are investigated. When the atoms are pushed together, the IE two-electron singlet state 2.39 behaves correctly , since its components are LCAO functions that reduce to the He^+ ion limit. However, in the other limit of large distances between ions, $|Psi_{IE}^S\rangle$ does not behave in a reasonable manner, because there exists two ionic states $\phi_1\phi_1$ and $\phi_2\phi_2$ which each have two electrons on the same atom, and these have equal probability with the states $\phi_1\phi_2$ and $\phi_2\phi_1$ which have a single electron in each atom. When pulled apart, the wavefunction does not reduce to the limit of two H atoms, but rather a 50/50 mixture of atoms and ions. Additionally, at large distances, the triplet state would actually be the ground state, since its expectation value does not have the additional contribution from the ionic states.

Both these inconsistencies can be overcome by the Heitler-London approximation:

$$\Psi_{HL}^S = \frac{1}{2\sqrt{1+S}} [\phi_1(r_1)\phi_2(r_2) + \phi_2(r_1)\phi_1(r_2)][\alpha_1\beta_2 - \beta_1\alpha_2] \quad (2.41)$$

However, we must recognize that this approximation will not be good for tight bonds, since we have seen that the IE wavefunction does reduce to the correct form for this case. At the same

time, it turns out that at the equilibrium molecular distance, the Heitler-London wavefunction is a better approximation for H_2 .

Now we want to find the energies associated with the singlet and triplet HL wavefunctions, in order to express the singlet-triplet and bonding-antibonding splitting in closed form. We do this by connecting the total Hamiltonian for \mathcal{H}

$$E^S = \frac{\langle \Psi_{HL}^S | \mathcal{H}(r_1, r_2) | \Psi_{HL}^S \rangle}{\langle \Psi_{HL}^S | \Psi_{HL}^S \rangle} = 2E_0 + \frac{C + X}{1 + S} \quad (2.42)$$

and

$$E^T = \frac{\langle \Psi_{HL}^T | \mathcal{H}(r_1, r_2) | \Psi_{HL}^T \rangle}{\langle \Psi_{HL}^T | \Psi_{HL}^T \rangle} = 2E_0 + \frac{C - X}{1 - S} \quad (2.43)$$

With S the double overlap function given by 2.37, and E_0 is the atomic energy of the H atom:

$$E_0 = \langle \phi_1(r_1) | \mathcal{H}_{atom}^1 | \phi_1(r_1) \rangle = \langle \phi_2(r_2) | \mathcal{H}_{atom}^2 | \phi_2(r_2) \rangle \quad (2.44)$$

and C the Coulomb integral,

$$C = \langle \phi_1(r_1) \phi_2(r_2) | \mathcal{H}' | \phi_1(r_1) \phi_2(r_2) \rangle \quad (2.45)$$

and X the exchange integral

$$X = \langle \phi_1(r_1) \phi_2(r_2) | \mathcal{H}' | \phi_1(r_2) \phi_2(r_1) \rangle \quad (2.46)$$

Note that the exchange term X links two electron terms where each electron is attached to different nuclei and thus it falls off exponentially similar to the overlap function, and more rapidly than the Coulomb interaction C . This means that magnetism of solids is primarily due to short-range interactions. Finally, the singlet-triplet splitting is:

$$E^S - E^T = 2J = 2 \frac{X - SC}{1 - S^2} \quad (2.47)$$

The Heitler-London function Ψ_{HL}^S is the prototypical quantum mechanical description for correlated or localized electrons, because of the importance of the singlet-triplet correlation for bonding. At the same time, the independent electron function Ψ_{IE}^S is the prototype for independent, delocalized, or itinerant electrons. In practice, this is accomplished when the field experienced by a single electron can be well approximated by a spatial average over the positions of all the other electrons in the system. This approach is put into practice by the Hartree-Fock method and underlies density functional theory (DFT).

2.3.3 Model Hamiltonians: Hubbard and Heisenberg models

Due to the difficulties of establishing a first-principles theory as illustrated above, another common technique is to utilize model Hamiltonians to understand the experimental properties of magnetic systems. The most well-known of these models are the Heisenberg and Hubbard models. In the Heisenberg model, the spin is explicitly included, and has been used extensively to model the behavior of ferromagnets in 1,2, and 3 dimensions. The Hubbard model, in contrast, has no explicit inclusion of the spin, but has particular importance in describing the splitting electronic states in correlated materials. This model provides the transition between an independent electron model and a model that includes correlated electrons. We will discuss these models in the context of the H_2 molecule, where the two models can be solved exactly.

2.3.3.1 Heisenberg Hamiltonian

This model requires the existence of two states; the singlet and triplet states, in order to couple the two spins with correct degeneracy and relative energy. These energies are given by Eqns. 2.35 and 2.36, and there are three terms responsible for the energies of these states. Therefore we write the effective Hamiltonian in terms of these energies:

$$\mathcal{H}_{eff} = 2\mathcal{H}_0 + \mathcal{H}_{coul} + \mathcal{H}_{exch} \quad (2.48)$$

E_0 is the expectation value of the atomic central field Hamiltonian \mathcal{H}_0 , Coulomb energy C

is the expectation value of \mathcal{H}_{coul} and $\pm X$ are the singlet and triplet expectation values of \mathcal{H}_{exch} . To explicitly include spin in this model, we use the model Hamiltonian,

$$\mathcal{H}_{exch} = A s_1 \cdot s_2 \quad (2.49)$$

where A is a constant, and the spins $s=1=\pm 1/2$ and $s_2=\pm 1/2$ couple to the total spin as $S=s_1+s_2$, with $S^2=(s_1)^2+(s_2)^2+2s_1 \cdot s_2$ and the combination results in a triplet $S=1$ or singlet $S=0$ state. Using the operator expectation values, it can be shown that the triplet state has an energy of $s_1 \cdot s_2 = 1/4$, while the singlet has energy $s_1 \cdot s_2 = -3/4$.

Extending the two-electron Heisenberg Hamiltonian from two spins to a many-electron system is done:

$$\mathcal{H}_{eff} = - \sum_{i \neq j}^N J_{ij} s_i \cdot s_j = -2 \sum_{i < j}^N J_{ij} s_i \cdot s_j \quad (2.50)$$

with an exchange integral defined similar to the atomic case,

$$J_{ij} = \int \int \Psi_i(r_1) \Psi_j(r_2) \frac{e^2}{4\pi\epsilon_0 r_{12}} \Psi_i^*(r_2) \Psi_j^*(r_1) dr_1 dr_2. \quad (2.51)$$

There are several key points we need to summarize about the Heisenberg model. First, the coupling energy is positive for ferromagnetic coupling and negative for antiferromagnetic, with different ground states (singlet or triplet), respectively. The coupling of individual spins, located on the same atom, is called the intra-atomic exchange, while coupling of atomic moments on different atoms is the inter-atomic exchange. Finally, when reduced to a single dimension, the Heisenberg Hamiltonian becomes the famous Ising model:

$$\sum_{i < j}^N J_{ij} (s_z)_i (s_z)_j \quad (2.52)$$

2.3.3.2 Hubbard Hamiltonian

In the Hubbard model, the magnetic ground state is found via a balance of two competing energies. Spin enters into the model only through the Pauli principle. The two balanced forces are the hopping energy and the Coulomb energy. The hopping energy is the motion of electrons of the same spin between different atoms, and favors delocalized, band-like behavior. On the other hand, the Coulomb energy is experienced by electrons of different spins, and keeps electrons apart and confined to different atoms. This force drives the formation of localized moments.

For the H_2 atom, the Hubbard Hamiltonian is written as:

$$\mathcal{H}_{eff} = 2\mathcal{H}_0 + \mathcal{H}_{Hub} \quad (2.53)$$

with \mathcal{H}_{Hub} :

$$\mathcal{H}_{Hub} = -t \sum_{\sigma=\downarrow,\uparrow} (c_{1\sigma}^\dagger c_{2\sigma} + c_{2\sigma}^\dagger c_{1\sigma}) + U(n_{1\uparrow}n_{1\downarrow} + n_{2\uparrow}n_{2\downarrow}) \quad (2.54)$$

where the $c_{i\sigma}^\dagger$ and $c_{i\sigma}$ are the creation and annihilation operators for electrons with spin σ on atom i , and thus the first term describes the motion of the electron hopping from site to site. The operator $n_{i\sigma} = c_{i\sigma}^\dagger c_{i\sigma}$ is the number operator that counts the occupation on atom i for a given spin σ . For H_2 we have: $\langle \sigma | n_{i\sigma} | \sigma \rangle = 1$ and $\langle \sigma | n_{i\sigma} | \sigma' \rangle = \langle \sigma' | n_{i\sigma} | \sigma \rangle = 0$. Thus this term describes the interaction of electrons with opposite spin on the same atom.

One notable detail about the Hubbard Hamiltonian is that the hopping operator only moves spins between atomic sites, but cannot flip them. The Hamiltonian actually acts only on the spatial part of the wavefunctions via coordinate changes but does not affect the spins, in contrast to the Heisenberg Hamiltonian. However, the concept of hopping quickly transfers to a band model of solid, and in fact a version of this model called the Bose-Hubbard model is commonly used as a first-order quantum mechanical description of solids. The discussion of band theory quickly brings us to the next step in our description of magnetism, which is the inclusion of the crystal lattice.

	K	Ca	Sc	Ti	V	Cr	Mn	Fe	Co	Ni	Cu	Zn
N_{3d}	0	0	1	2	3	5	5	6	7	8	10	10
N_{4s}	1	2	2	2	2	1	2	2	2	2	1	2
N_{3d+4s}	1	2	3	4	5	6	7	8	9	10	11	12

Figure 2.1: Number of 3d and 4s electrons in the free transition metal atoms

2.4 Band Model of Ferromagnetism

Here we discuss the effects of the bonds between atoms in solids, in the specific context of the 3d transition metals.

2.4.1 Shortfall of the atomic picture: predicting the magnetic moment of the transition metal solids

In the atomic picture, the spin and orbital magnetic moments of atoms are multiples of the Bohr magneton according to $m = (2s+1)\mu_B/\hbar$. Thus an initial guess for the magnetic moments for the transition metals would be even multiples of μ_B . The magnetic moment could be determined by the number of unpaired electrons in each atom's shell. The number of 3d and 4s electrons in the transition metal atoms are given in Fig. 2.1.

For example, in Fe, there is a possibility of 12 electrons occupying the 4s and 3d orbitals, and only 8 electrons occupying these positions, giving rise 4 unfilled "holes", for which situation Hund's rule would predict a magnetic spin moment of $\mu_s=4\mu_B$ for Fe, and similarly $3\mu_B$ for Co and $2\mu_B$ for Ni.

However, if the spontaneous magnetization M of Fe, Co and Ni is measured and divided by the number of atoms, the resulting values are $m_{exp} = 2.215 \mu_B$ for Fe, $1.715 \mu_B$ for Co, and $0.616 \mu_B$ for Ni. The sizes of these values immediately illustrates that the atomic picture cannot provide an accurate description of the magnetism of solids. In the next section, we will take a different approach, accounting for the itinerant nature of the electrons, and treating the effects of bonding

of the atoms in a metal lattice.

2.4.2 Bragg scattering and Band structure

Before we introduce a model that includes magnetism in the context of a crystalline lattice, we will first introduce the language of band structure and the effect of periodic boundary conditions on the solutions of Schrödinger's equation for electrons in a periodic potential such as a crystalline lattice of ions. We begin with Bragg reflection of the electron from the lattice.

The most important consequence of Bragg reflection in our discussion is that it leads to the presence of an energy gap. In the 1-D case, the Bragg equation becomes:

$$\begin{aligned} 2dsin\theta &= n\lambda \\ k &= n\pi/a \end{aligned} \tag{2.55}$$

The first reflection occurs at $k = +/- \pi/a$ and the first energy gap is there as well. Other energy gaps occur for the other positive and negative integral values of n .

Reflection at $k = +/- \pi/a$ arises because the wave reflected from the $(p +/- 1)$ st atom interferes constructively with the original wave at the p th atom. The region in k space between $+/- \pi/a$ is the first Brillouin zone.

At $k = +/- \pi/a$ the stationary state wave functions are not traveling waves as for the free particle model, but the solutions at these particular k values are made up equally of waves traveling to the right and the left: standing waves. For $k = +/- \pi/a$ we have two independent standing wave solutions:

$$\begin{aligned} \Psi_1 &\approx \sin(\pi x/a) \approx (e^{i\pi x/a} - e^{-i\pi x/a}) \\ \Psi_2 &\approx \cos(\pi x/a) \approx (e^{i\pi x/a} + e^{-i\pi x/a}) \end{aligned} \tag{2.56}$$

These solutions are made up of equal parts waves traveling to the right and left. Moreover, these solutions correspond to different values of the potential energy of the particle, owing to the positional shift between the two wavefunctions. Ψ_1 distributes charge preferentially midway between ion cores, while Ψ_2 distributes charge preferentially on the ion cores. On calculating

average values of the potential energy over the three charge distributions, we expect the potential energy of Ψ_1 to be greater than that of a plane wave while that of Ψ_2 to be less than that of a plane wave.

If the potential energies of the states Ψ_1 and Ψ_2 differ by an amount ΔE , we have an energy gap of width ΔE . The physical reason for the gap is this: If wave functions at values of k far removed from the Brillouin zone boundaries $+/- \pi/a$ may be represented by plane waves e^{ikx} , then in forming a solution of the wave equation as the boundaries are approached and Bragg reflection becomes imminent the wave gradually becomes an admixture of the wave $e^{i[k-(2\pi/a)]x}$, until at the zone boundary $k = +/- \pi/a$ and the solution is $e^{i\pi x/a} +/- e^{-i\pi x/a}$.

2.4.3 The Stoner Model

The problem of predicting the value of the magnetic moment for transition metals was solved by developing a band theory for magnetic systems, which was done in 1935 by Mott, Slater, and Stoner [stohr 27-31]. This model is called the Stoner model.

In this model, the bonding interaction in the 3d electrons causes a smearing of the energy into a band. The periodicity condition of the lattice leads to the characteristic periodic variations and as seen above, their band width increases with the inverse lattice constant. For our first description of the Stoner model, we can consider the average finite energy width of the valence band states and approximate the density of states as a simple semicircle as shown in Fig. 2.2.

Here we introduce the terminology of majority and minority charge carriers. The electrons with spin states corresponding to the larger electron population are the "majority band" while those with the smaller population are the "minority band". This terminology will be extensively used in Section 6, since the distinction between minority and majority carriers becomes especially important for the special class of ferromagnets called half-metals studied in this project.

Next we proceed to derive an expression for the magnetic moment that is relevant for both electron and hole pictures. From the spin resolved density of states we can compute the number of

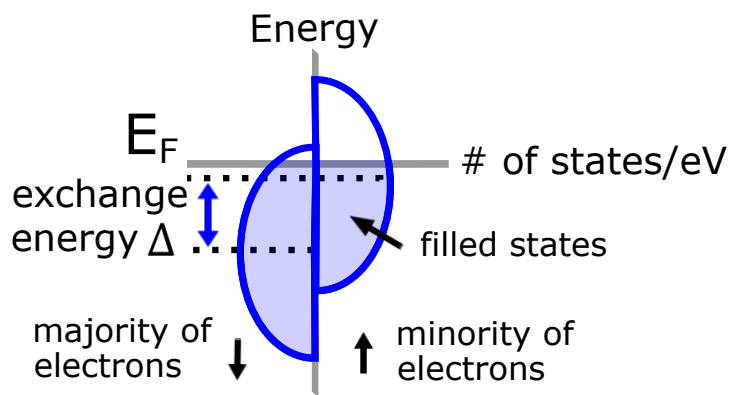


Figure 2.2: Stoner Model for ferromagnetic transition metals, and illustration of terms used for the description of this model. The filled electron states (at zero temperature) below the Fermi energy E_F are shaded. The spin population with greater occupied states is called the majority band, while the population with less occupied states is called the minority band. The centers of the two bands are separated by the exchange energy Δ .

spin states in the majority and minority bands by energy integration:

$$N_e^{maj} = N_e^\downarrow = \int_{-\infty}^{E_F} D^\downarrow(E) dE \quad (2.57)$$

From electromagnetic theory, the atomic magnetic moment is given by $m = -2\mu_B s/\hbar$ with s having the units of $[\hbar]$. The absolute value of m can be found via the expectation of the electron spin operator $\langle s_z \rangle$ according to the expression $-m = -2\mu_B \langle s_z \rangle / \hbar$. Using the convention that the spin up states are labeled $|\uparrow\rangle = |+\rangle$ with eigenvalue $s_z = +\hbar/2$ and the spin down states $|\downarrow\rangle = |-\rangle$ with eigenvalue $s_z = -\hbar/2$, we have for s_z ,

$$\langle s_z \rangle = \left\langle +\frac{1}{2}|s_z| + \frac{1}{2} \right\rangle N_e^{min} + \left\langle -\frac{1}{2}|s_z| - \frac{1}{2} \right\rangle N_e^{maj} \quad (2.58)$$

$$= \frac{\hbar}{2}(N_e^{min} - N_e^{maj}) = \frac{\hbar}{2}(N_e^\uparrow - N_e^\downarrow) \quad (2.59)$$

and we have the maximum number of electrons in the d shell: $(2s+1)(2l+1) = 10$. We also have $N_e + N_h = 10$. Thus the number of holes in the minority band $N_h^{min} = N_h^\uparrow$ and for the majority band $N_h^{maj} = N_h^\downarrow$ is $N_e^\downarrow + N_h^\downarrow = 5$ and $N_e^\uparrow + N_h^\uparrow = 5$ and thus,

$$\langle s_z \rangle = \frac{\hbar}{2}(N_e^\uparrow - N_e^\downarrow) = -\frac{\hbar}{2}(N_h^\uparrow - N_h^{maj}). \quad (2.60)$$

And finally we can conclude that the magnetic moment $-m$ is given by the difference in the number of electrons or holes in the majority and minority bands, according to,

$$|m| = \mu_B(N_e^{maj} - N_e^{min}) = \mu_B(N_h^{min} - N_h^{maj}). \quad (2.61)$$

When finally including these numbers, we find that in the band picture, the number of majority and minority states is a non-integer, and thus the magnetic moments are noninteger multiples of the Bohr magneton as experimentally measured. This simple relation between electron and hole moments is exact only if the band states are well defined in their energy spread about the Fermi level. In reality, there is hybridization between the d states and the s-p states such that even

10 eV above the Fermi level, there is some small d character in the s-p bands. Thus the number of d holes and the magnetic d moment is slightly reduced relative to the values expected from the filled electron states (cite stohr 240,241).

Since we now have a value for the magnetic moment, the exchange energy can also be written as an "exchange field", an effective magnetic field that splits the levels and can be used to describe the origin splitting as $\Delta = 2m\dot{H}_{ex}$. In addition, it exerts a torque $T = m \times H_{ex}$ on the electron spins. This gives us a surprisingly giant value for the effective exchange field of 10^3 T. The size however gives us a quantitative understanding for the giant strength of the magnetic interaction in 3d ferromagnets. It is important to keep in mind that this exchange field does not act on the orbital moment or the nuclear magnetic moment, and thus the effect of the exchange interaction on the spin system is separate from the orbital system. The two systems can interact, but only via the (much weaker) spin-orbit interaction.

Although the Stoner model does a good job of predicting the magnetic moments of the transition metals by accounting for the bonds between atomic sites, there are some major shortfalls with the model. In particular, when attempting to calculate the Curie temperature for the transition metals, one comes up with a number several thousands of kelvin higher than experimentally measured. This is because the Stoner model fails to account for interactions between electron spins directly. It is basically an extension of the Hubbard model to band theory rather than the Heisenberg model.

2.5 The next frontier: ultrafast laser-induced ferromagnet dynamics

As a ferromagnetic metal approaches the Curie temperature, it reaches a critical point where the magnetic properties of the material change dramatically. Under equilibrium conditions, this ferromagnetic-to-paramagnetic phase transition is associated with critical phenomena, characterized by a vanishing of the spontaneous magnetization as well as a divergence of the magnetic heat capacity and susceptibility (1). A faster route to change the magnetization is to use femtosecond laser irradiation: Since the first experimental observation of ultrafast laser-induced demagnetiza-

tion (2), femtomagnetism has been a subject of intense experimental and theoretical studies.

When a ferromagnetic metal is heated with a femtosecond laser pulse, the energy directly couples into the electron bath, creating an out-of-equilibrium electron distribution. This electron energy distribution quickly thermalizes (within tens of femtoseconds) to a hot Fermi-Dirac energy distribution. In most past work, the laser- induced demagnetization process was described as a sequence of events where the energy of the hot electron bath transfers first to the spin and later to the lattice degrees of freedom. This cascade of energy relaxation processes is used to explain why ultrafast demagnetization occurs over a range of time scales from approximately 100 to 500 fs (2, 3). These multiple time scales observed in past experiments obscured any contributions from critical phenomena. Although there is still no consensus on the important microscopic mechanisms that drive ultrafast demagnetization, or their relevant time scales, a number of microscopic models have been proposed. These are based on spin-flip scattering (38) that transfers spin angular momenta during the demagnetization process, as well as laser-induced polarized (911) or unpolarized (12, 13) spin currents that can also lead to ultrafast demagnetization.

We note that the ability to manipulate the magnetic state on femtosecond timescales is important both scientifically and technologically. Although ferromagnetic metals are some of the simplest materials that exhibit strong interactions between the electron, spin, and lattice degrees of freedom, there is yet no comprehensive theory that describes their non- equilibrium behavior. Past work concluded that many different timescales were associated with laser-induced magnetic dynamics and that these depended on the pump fluence [16,28] and sample geometry [29,30]. This made it challenging to develop complete theories and compare with experiments. In contrast, by showing the essential contribution of critical behavior associated with a magnetic phase transition, we reveal that only a few characteristic timescales are needed to fully explain ultrafast demagnetization in Ni.

Chapter 3

Experimental Techniques

In the previous chapter we provided a microscopic description of ferromagnetism and the motivation for how certain properties of ferromagnets arise. In this section, we will proceed to treat the interaction of light with these properties and explain how light can be used as a sensitive probe for magnetism.

Although visible light interacts with magnetism in materials in a non-resonant fashion, the resonant interaction of high energy light with the core level electrons in a ferromagnet provides a much stronger and more detailed source of information about the material. Traditionally, the 2p core level shells have been probed using light from synchrotrons and free electron lasers. The physics that describes these resonances is almost identical to the physics that occurs when light resonant at the 3p level shells is used. In this thesis, we generate light resonant with the 3p level electrons via the process of high harmonic generation. This technique has the advantages that the temporal duration of the probe is < 10 fs and carries a broad comb of energies, that can be resonant with multiple chemical elements simultaneous.

The resonance associated with the 3p core level electrons in transition metals is commonly referred to as the M-edge, while the 2p level resonance is called the L-edge. In this section, we will explain how the resonance at the L-edge can be used to directly measure the magnetic moment of a material. This description also applies to light resonant at the M-edges. Additionally, we will focus on circularly polarized light, because it provides an intuitive and convenient basis for our discussion. However, all of the experiments performed in this thesis were in fact carried out using

linearly polarized light. This is possible because linear polarization is also a combination of right and left circularly polarized light, and for certain geometries, the microscopic physics that we will discuss here leads directly to a complex dielectric permittivity tensor that interacts with linearly polarized light in a useful fashion.

3.1 Resonant processes in magnetic materials: determining the X-ray absorption intensity

In this thesis, two different resonant processes are used to monitor fundamental changes in magnetic materials after ultrafast laser excitation. The first is to directly monitor the charge response using the change in absorption of the resonant extreme ultraviolet light, and the second is to monitor the change in magnetic moment using the magneto-optical Kerr effect. In this section, we theoretically derive the origin for each of these effects, starting the sum rule for charges and how the absorption intensity for a transition from a core to valence band depends directly on the number of holes in the valence band. Using this information it is a straightforward extension to see how circularly polarized light is also sensitive to the number of spin up and spin down electrons in the valence band as well. This information can then be used to monitor the magnetic moment of the material and is the fundamental basis for the magneto-optical effects employed in this thesis.

3.1.1 Transition matrix element for atoms

We begin from the most basic quantum mechanical expression available to describe polarization dependent X-ray absorption and resonant scattering. We want to calculate the intensity of a strong resonance such as the $2p_{3/2}, 2p_{1/2} \rightarrow 3d$ transition.

The transition matrix elements can be written (by quantizing the electromagnetic field) in the general form:

$$M = \langle b | \mathbf{p} \cdot \boldsymbol{\epsilon} e^{i\mathbf{k} \cdot \mathbf{r}} | a \rangle \quad (3.1)$$

with \mathbf{p} the electron momentum vector, $\boldsymbol{\epsilon}$ the unit photon polarization vector, and \mathbf{k} the photon

wave vector. We can simplify this expression by taking the dipole approximation, which is well justified in both the soft x-ray (L-edge) and extreme ultraviolet (M-edge) regimes. This is simply the assumption that size of the absorbing atomic shell is small relative to the X-ray wavelength, so that the electric field that drives the electronic transition is constant over the atomic volume. In the photon energy range $\hbar\omega \leq 1,000$ eV, with a wavelength $\lambda > 1.2$ nm with transitions from the 2p core shell of radius $|r| \approx 0.01$ nm so that $|r| \approx 0.01$ nm $< \lambda/2\pi \approx 0.2$ nm. Given that the wavelength of EUV is an order of magnitude larger, while the 3p shell is only marginally larger in spatial extent to the 2p shell, it is reasonable to use the dipole approximation for our discussion here. In this approximation we have:

$$M = \langle b|\mathbf{p} \cdot \boldsymbol{\epsilon}(1 + ik \cdot r + \dots)|\rangle \approx \langle b|\mathbf{p} \cdot \boldsymbol{\epsilon}|a\rangle = im_e\omega \langle b|\mathbf{r} \cdot \boldsymbol{\epsilon}|a\rangle \quad (3.2)$$

with m_e the electron rest mass, and $\omega = \omega_b - \omega_a$ the photon frequency for the transition from state $|a\rangle$ to state $|b\rangle$. The X-ray absorption cross section can be written:

$$\sigma^{abs} = 4\pi^2 \frac{e^2}{4\pi\epsilon_0\hbar c} \hbar\omega |\langle b|\boldsymbol{\epsilon} \cdot \mathbf{r}|a\rangle|^2 \delta[\hbar\omega - (E_b - E_a)] \rho(E_b) \quad (3.3)$$

with the density of final states per unit energy $\rho(E_b)$ depends on the normalization of the electronic wavefunctions $|a\rangle$ and $|b\rangle$. When these functions have been volume normalized to unity, the following expression can be obtained:

$$I_{res} = A |\langle b|\boldsymbol{\epsilon} \cdot \mathbf{r}|a\rangle|^2 \quad (3.4)$$

with the proportionality A given as

$$A = 4\pi^2 \frac{e^2}{4\pi\epsilon_0\hbar c} \hbar\omega = 4\pi^2 \alpha_f \hbar\omega \quad (3.5)$$

and the dimensionless fine structure constant α_f

$$\alpha_f = \frac{e^2}{4\pi\epsilon_0\hbar c} = \frac{1}{137.04} \quad (3.6)$$

The resonance intensity I_{res} has dimensions of [length² × energy].

Now the calculation of the transition matrix element depends on the initial and final state wavefunctions $|a\rangle$ and $|b\rangle$ which, in the one electron picture, consist of the core level and valence electron wavefunctions, respectively.

In a one-electron picture an "initial" state wavefunction for a core shell n with angular momentum c is given by

$$|a\rangle = |R_{n,c}(r); c, m_c, s, m_s\rangle \quad (3.7)$$

with $R_{n,c}(r)$ the radial component of the core shell with the principle quantum numbers n and orbital quantum number c , $|s = 1/2, m_s\rangle$ the spin state of the electron. The final state can also be written as

$$|b\rangle = |R_{n',l}(r); l, m_l, s, m'_s\rangle \quad (3.8)$$

$R_{n',l}$ is the radial component of the valence state of shell n' with angular momentum l . These final states are determined by the empty states in the l subshell. Thus we need to calculate the transition matrix element

$$\langle b | P_\alpha^q | a \rangle = \langle R_{n'l}(r); l, m_l, s, m'_s | P_\alpha^q | R_{n,c}(r); c, m_c, s, m_s \rangle \quad (3.9)$$

with the direction and polarization dependent dipole operator P_α^q written in the general form:

$$P_\alpha^q/r = \sum_{p=0,\pm 1} e_{\alpha,p}^q C_p^{(1)} = e_{\alpha,1}^q C_1^{(1)} + e_{\alpha,0}^q C_0^{(1)} + e_{\alpha,-1}^q C_{-1}^{(1)} \quad (3.10)$$

where $C_q^{(1)}$ are the Racah operators for spherical harmonics, and the coefficients $e_{\alpha,p}^q$ may be imaginary with $\sum_p |e_{\alpha,p}^q|^2 = 1$. for a transition from a core shell with angular momentum c to an

unfilled valence shell with angular momentum l we then have:

$$\langle b|P_\alpha^q|a\rangle = \delta(m_s', m_s) \langle R'_n, l|r|R_{n,c}(r)\rangle \sum_{m_c, m_l, p} e_{\alpha, p}^q \langle l, m_l|C_p^{(1)}|c, m_c\rangle \quad (3.11)$$

Several things become immediately apparent from this description. First, the dipole operator does not act on spin, and thus only spin conserving transitions are allowed. Next, the polarization dependence is entirely contained in the angular part of the wavefunction. And finally, the radial part determines the angle integrated transition strength. It is also the part of the wavefunction responsible for the elemental specificity of X-ray absorption spectroscopy. Even though the final valence state has a relatively large radial wavefunction, the radial extent of the transition matrix element between the 2p and 3d states is relatively localized. This localization leads to some fundamental differences between x-ray absorption spectroscopy and optical spectroscopy.

In general, optical transitions occur only between empty and filled valence states, and thus are not localized on any specific atom, but instead the intensity of the transition is determined by the group theoretical symmetry of the valence state of the crystal or molecule.

The angular part of the transition matrix element has the form $\langle l, m_l|C_q^{(1)}|c, m_c\rangle$, and the nonzero matrix elements here dictate the dipole selection rules.

3.1.2 Transition matrix elements for atoms in solids

The next step is to continue the calculation of the transition matrix elements for a real system, namely that of atoms in a solid, as measured experimentally in this thesis. To do this, we need to use realistic initial and final state wavefunctions. Fortunately, the wavefunctions of bonded atoms can be constructed from linear combinations of the atomic wavefunction.

Within this approximation, called the tight binding model, we can write the wavefunctions for the electrons as:

$$|\Psi_i(\mathbf{k}, r)\rangle = |R_{n,L}(r)|\phi_i(\mathbf{k})\rangle \quad (3.12)$$

$$= |R_{n,L}(r)\rangle \sum_{M=-L}^{+L} a_{i,M}(\mathbf{k}) |LM\chi^+\rangle + b_{i,M}(\mathbf{k}) |LM\chi^-\rangle \quad (3.13)$$

with energy $E_i(k)$, the X-ray absorption transition intensity can be written,

$$I_\alpha^q = A \sum_{E_i > E_F; i, \mathbf{k}, m, j} |\langle \Psi_i(\mathbf{k}, r) | P_\alpha^q | \Phi_m^j(r) \rangle|^2 \quad (3.14)$$

$$AR^2 \sum_{E_i > E_F; i, \mathbf{k}, m, j} |\langle \phi_i(\mathbf{k}) | \sum_{p=0\pm 1} e_{\alpha,p}^q C_p^{(1)} |cm\chi^j\rangle|^2 \quad (3.15)$$

and by using the fact that the dipole operator does not act on spin we can write the transition intensity:

$$I_\alpha^q = AR^2 \sum_{E_i > E_F; i, \mathbf{k}, m} |\sum_{p,M} a_{i,M}(\mathbf{k}) e_{\alpha,p}^q \langle LM | C_p^{(1)} | cm \rangle|^2 + |\sum_{p,M} b_{i,M}(\mathbf{k}) e_{\alpha,p}^q \langle LM | C_p^{(10)} | cm \rangle|^2 \quad (3.16)$$

3.1.3 Intensity Sum Rule for Charge

The sum rule for charge states that the transition intensity is proportional to the total number of empty d states N_h when a sum is taken over the $2p_{3/2}$ and $2p_{1/2}$ contributions. By separating the diagonal and cross terms in Eqn. 3.16 we have:

$$I_\alpha^q = AR^2 \sum_{E_i > E_F; i, \mathbf{k}, m} \sum_{p,M} [|a_{i,M}(\mathbf{k})|^2 + |b_{i,M}(\mathbf{k})|^2] |e_{\alpha,p}^q|^2 |\langle LM | C_p^{(1)} | cm \rangle|^2 \quad (3.17)$$

$$+ AR^2 \sum_{E_i > E_F; i, \mathbf{k}, m} \sum_{p \neq p', M \neq M'} e_{\alpha,p}^q (e_{\alpha,p'}^q) * \langle LM | C_p^{(1)} | cm \rangle \langle LM' | C_{p'}^{(1)} | cm' \rangle * \quad (3.18)$$

$$\times [a_{i,M}(\mathbf{k})(a_{i,M'}(\mathbf{k})) * + b_{i,M}(\mathbf{k})(b_{i,M'}(\mathbf{k})) *] \quad (3.19)$$

from here we can perform orientation average by summing over the three orthogonal polarization states $q = 0, \pm 1$ or over crystal dimensions $\alpha = x, y, z$. The cross term then vanishes and the polarization averaged transition intensity is now:

$$\langle I \rangle = \frac{1}{3} AR^2 \sum_{E_i > E_F; i, \mathbf{k}, M} (|a_{i,M}(\mathbf{k})|^2 + |b_{i,M}(\mathbf{k})|^2) \sum_{p,m} |\langle LM | C_p^{(1)} | cm \rangle|^2 \sum_{q \text{ or } \alpha} |e_{\alpha,p}^q|^2 \quad (3.20)$$

where the first sum is the number of holes in the material, the second sum is characterized by $L/2L+1$, and the final sum in the term is equal to 1. Finally, then we have the transition intensity for a core to valence $nc \rightarrow nc'$ can be written as

$$\langle I \rangle = AR^2 \frac{L}{3(2L+1)} N_h \quad (3.21)$$

with $A = 4\pi^2 \hbar \omega / 137$ and R is the radial $nc \rightarrow n'L$ matrix element.

This relation is called the intensity sum rule for charge and allows us to directly relate the intensity of an electronic transition to the number of valence holes in the electronic ground state.

3.1.4 X-ray Magnetic Circular Dichroism

It is now a reasonable extension to think that if we could make the absorption of photons spin dependent, we could measure a intensity difference corresponding to the difference between spin up and spin down electrons, which is directly proportional to the magnetic moment, as shown in Chapter 2.

For simplicity, we will assume a one-electron picture that corresponds to the Stoner splitting as derived in the previous chapter. For the XMCD effect to have a maximum, the magnetization direction \mathbf{M} of the sample and the photon spin or angular momentum \mathbf{L}_{ph} should be collinear.

3.2 Kerr Effect

As outlined in the previous section, when linearly polarized light reflects from a magnetized solid it is modified in two ways: first the direction of polarization is rotated over an angle Θ_K , and secondly the phase of the light is modified so that it becomes elliptically polarized. When the magnetization is applied in a transverse geometry (see Fig. ref), the amplitude of the light is modified as well. It is this effect, that we will employ for the majority of the work in this thesis, due to the fact that changes in intensity are much simpler to monitor in the EUV light regime than changes in the polarization of the light.

3.2.1 Transverse magneto-optical effect (TMOKE)

We now consider the interaction of magnetic media magnetized in the transverse direction (see fig ref) with linearly polarized light. In the s- and p- polarization basis (E_s, E_p), we write the incident electric field \vec{E}_i , i.e. the time- and space- independent part of the (plane wave) radiation as

$$\vec{E}_i = \begin{pmatrix} E_s \\ E_p \end{pmatrix} = \begin{pmatrix} \cos(\theta) \\ \sin(\theta) \end{pmatrix} E_0 \quad (3.22)$$

with E_0 the amplitude of the incoming electric field vector. In the following, we set E_0 to 1. Θ is the angle of the linearly polarized radiation relative to the s-polarization direction. The reflected field \vec{E}_r can be related to the incident field through the Fresnel reflection matrix $\hat{\mathbf{r}}$ as

$$\vec{E}_r = \hat{\mathbf{r}} \vec{E}_i = \hat{\mathbf{r}} \begin{pmatrix} \cos(\theta) \\ \sin(\theta) \end{pmatrix}. \quad (3.23)$$

Now this matrix depends on the magnetization direction of the solid and can be written when \vec{m} lies in the (x,y) plane as,

$$\hat{\mathbf{r}}(\vec{m}) = \begin{pmatrix} r_{ss} & r_{sp} \\ r_{ps} & r_{pp} \end{pmatrix} = \begin{pmatrix} r_{ss}^{(0)} & r_{sp}^{(1)} m_y Q \\ -r_{sp}^{(1)} m_y Q & r_{pp}^{(0)} + r_{pp}^{(1)} m_x Q \end{pmatrix} \quad (3.24)$$

with the magneto-optical Voigt constant $Q = i\epsilon_{xy}/\epsilon_{xx}$ and the subscripts (0) and (1) indicate the coefficients in terms independent and linear in Q , respectively. Note that for the special case of the magnetization lying entirely in the x direction, the dielectric tensor will cause only the p-polarized light to be directly affected by the magnetization. In this work and many others, it is common to define an experimentally measurable quantity, the magnetic asymmetry:

$$A = \frac{R_+ - R_-}{R_+ + R_-} \quad (3.25)$$

where R_+ is the reflected intensity when the sample is fully magnetized in one direction

(arbitrary), and R_- the reflected intensity when the sample is fully magnetized in the other direction. When the magnetization lies only along the x-direction ($m_x=1$, $m_y=0$), then the asymmetry depends on the angle of incidence of the light and the material's Voigt constant as:

$$A = \frac{m_x(1 - \cos 2\theta)\text{Re}(r_{pp}^{(0*)} r_{pp}^{(1)} Q)}{|r_{pp}^{(0)}|^2 \sin^2 \theta + |r_{ss}|^2 \cos^2 \theta} \quad (3.26)$$

3.3 Interaction of matter with X-Ray radiation

Erskine and Stern (cite 1975) first proposed the use of X-rays resonant with the core level to valence band transitions to measure magneto-optical properties in the transition metals. The first X-ray magneto-optical effects were then discovered in 1986 and 1987 (Laan and Schutz).

3.4 High Harmonic Generation

Chapter 4

Results of Nickel Experiment

In this chapter we describe the comparison between time resolved transverse magneto optical Kerr effect and angle resolved photoemission. By combining time- and angle-resolved photoemission with time-resolved transverse magneto-optical Kerr spectroscopies, we show that the same critical behavior also governs the ultrafast magnetic phase transition in nickel.

4.1 Introduction

Here, we present clear evidence that critical behavior on a new ultrafast 20 fs time scale governs laser induced demagnetization in nickel. We show this by correlating time- and angle-resolved photoelectron spectroscopy (Tr-ARPES) with Tr-TMOKE spectroscopy, as well as with EUV transient reflectivity, all using tabletop high-harmonic sources (14). Through fluence and temperature dependent studies, we make several surprising observations. First, we observe critical behavior as the spin system undergoes a transient magnetic phase transition: As the laser fluence approaches a critical fluence F_c of ≈ 2.8 mJ/cm², corresponding to a hot electron temperature approaching the Curie temperature (631 K), significantly more laser energy is required to increase the peak electron temperature, indicating a divergence in the heat capacity of the spin system. Second and very surprisingly, the spin system absorbs sufficient energy within the first 20 fs to subsequently proceed through the phase transition. This defines a new time scale in the process of ultrafast demagnetization. Demagnetization (measured using TMOKE) and the collapse of the exchange splitting (measured using ARPES) both occur on much longer and similar timescales of

176 fs, independent of the laser fluence. Third, the recovery dynamics of the exchange splitting also exhibit a critical behavior, changing from a full recovery within 500 fs when pumped at fluences below F_c to a much longer 76-ps recovery above F_c . These critical phenomena indicate that the transient electron temperature alone dictates the magnetic response.

We note that our findings are in contrast to past work assuming that the electron bath alone absorbs the laser energy, which is then slowly transferred to the spin system throughout the demagnetization process (3, 5, 8, 15). Instead, our results imply that the ultrafast demagnetization of a ferromagnetic metal is driven by a highly nonequilibrium process that takes place within the first 20 fs, with sufficient energy transfer from the optical excitation to the spin system to subsequently proceed through the transient magnetic phase transition (see Fig. 1). This ultrafast, highly nonequilibrium process can likely be driven by superdiffusive spin currents (10, 11) or spin mixing via spin-orbit coupling (1618). Then, demagnetization of the sample occurs on a longer time scale of 176 fs, likely mediated by processes such as low-energy magnon generation.

4.2 Results

The observed critical behavior in laser-induced ultrafast demagnetization in nickel is shown schematically in Fig. 4.2A. Our time-resolved ARPES and TMOKE measurements were both performed using 780-nm laser-driven EUV high-harmonic generation (HHG) probe beams, as shown in Fig. 4.2 (B and C) (see Materials and Methods). For all measurements, the sample used is a 400-nm Ni(111) single-crystalline film grown on an $\alpha - Al_2O_3(0001)$ substrate (19). The Ni film thickness is much greater than both the pumping (13 nm) and probing depth (1 nm for ARPES; 10 nm for TMOKE) to avoid any influence of the substrate, capping layer, or multilayer structure (1113, 20).

The characteristic dynamics of Ni demagnetization measured by TMOKE, as well as of the exchange splitting (E_{ex}) measured by ARPES, are plotted in Fig. 4.2A as a function of pump-probe time delay (t_d). The TMOKE asymmetry A_s (see Materials and Methods) at 360 fs before the pump pulse arrives and 500 fs after the pump pulse arrives is plotted in Fig. 4.2B, where a clear

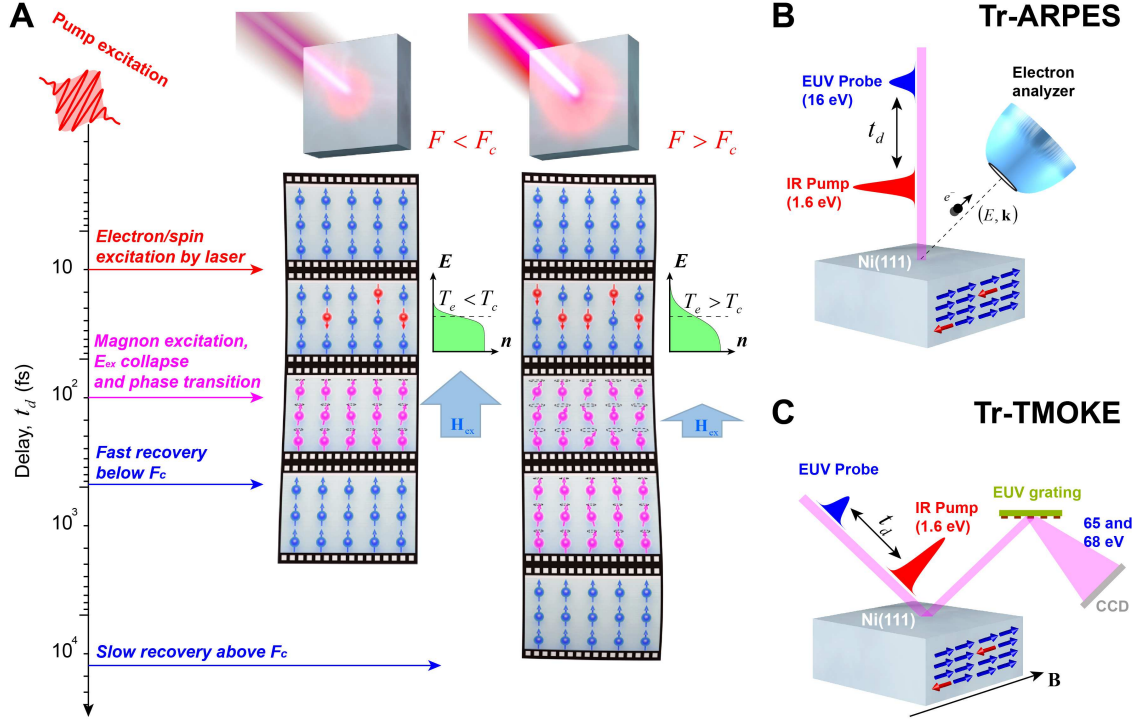


Figure 4.1: Schematic of the critical behavior of ultrafast demagnetization in Ni. (A) After excitation by a femtosecond laser pulse above the critical fluence (F_c), the transient electron temperature (T_e) is driven above the Curie temperature (T_c), inducing high-energy spin excitations within 20 fs, which store the magnetic energy (see text). The Fermi-Dirac distributions of electrons are also plotted. Demagnetization occurs later, in 176 fs, driven by relaxation of nonequilibrium spins and the likely excitation of low-energy magnons. Full recovery of the spin system occurs within 500 fs to 76 ps, depending on the laser fluence. (B and C) Experimental setups for time-resolved ARPES and TMOKE, respectively, using ultrafast high-harmonic sources. IR, infrared.

reduction of the asymmetry can be observed after laser excitation. Tr-TMOKE is a momentum-averaged measurement, as shown in the Supplementary Materials. For ARPES, the photoelectron spectra along the Γ - K direction at room temperature are shown in Fig. 4.2C. Before the pump pulse excites the sample ($t_d = 500$ fs), the exchange splitting (E_{ex}) between the majority and minority bands of Ni can be observed at momentum $k_{||} \approx 1.05\text{\AA}^{-1}$, where the d band crosses the Fermi energy (EF)(21, 22). The exchange splitting E_{ex} reduces after laser excitation, as indicated by the spectrum taken 500 fs after the pump pulse and the extracted photoemission intensity. The values of E_{ex} are obtained by fitting the extracted spectra with multiple Voigt functions (see Fig. 4.2C and the Supplementary Materials).

The dynamics of the exchange-splitting change (ΔE_{ex}) and TMOKE asymmetry (A_s) can be generally fit by an exponential decay and bi-exponential recovery function (see Materials and Methods). We find that the dynamics of ΔE_{ex} can be described by a set of time constants, with a dramatic change in recovery times above a critical laser fluence. For all pump laser fluences (below or above the critical fluence), the collapse of the exchange splitting exhibits a constant and fluence-independent time scale of 176 ± 27 fs. For fluences below a critical laser fluence of $F_c = 2.8\text{mJ/cm}^2$, the magnetic response exhibits a fast recovery ($\tau_{recover1} = 537 \pm 173$ fs). For fluences above F_c , the magnetic response exhibits the same fast recovery as well as a slower recovery ($\tau_{recover2} = 76 \pm 15$ ps; see the Supplementary Materials). These characteristic time constants are obtained using a global fitting scheme (see the Supplementary Materials). We note that the minima of dynamics shown in Fig. 4.2A depend on the ratio of demagnetization and fast recovery amplitudes. Although they appear at different time delays for different fluences, the extracted time constants (and characteristic time scales of the processes) are the same.

To correlate the dynamics of the exchange-splitting collapse ΔE_{ex} (probed by ARPES) with the laser-induced demagnetization of the sample, we analyze TMOKE measurements taken at similar pump fluences. We find that the time scale of demagnetization measured using TMOKE is the same as the exchange-splitting collapse measured using ARPES and that both are independent of the pump laser fluence (Fig. 4.2D). This is consistent with the conclusion that the collapse of

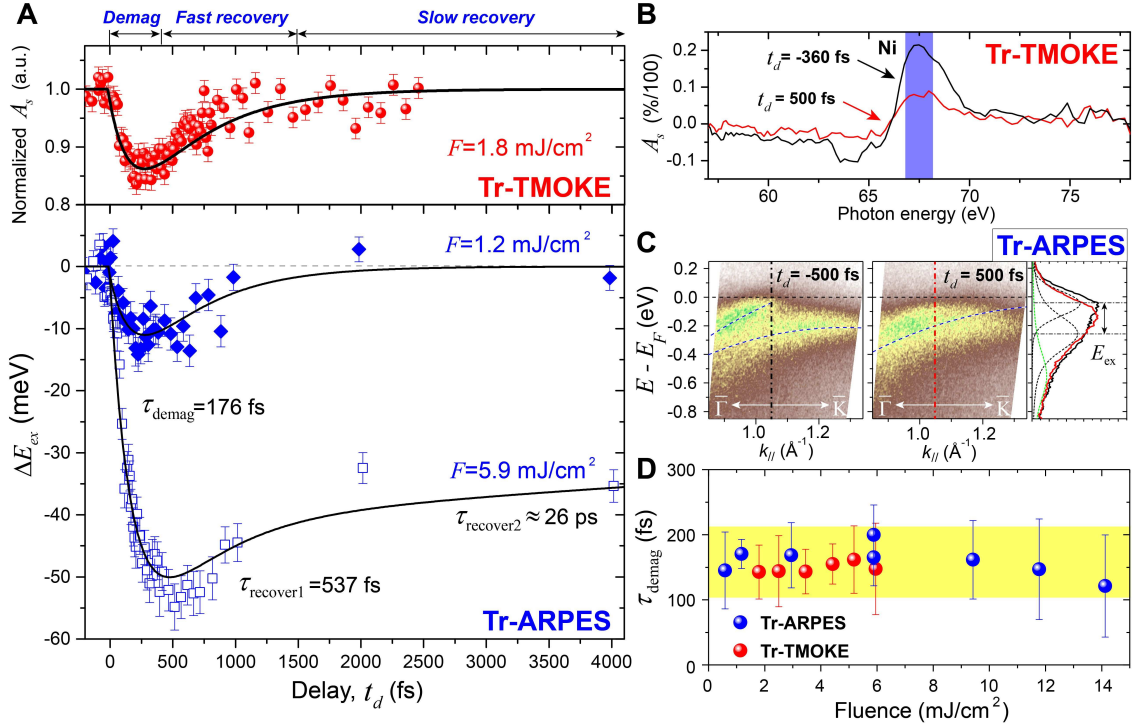


Figure 4.2: Magnetization dynamics in Ni. (A) Change of the TMOKE asymmetry and exchange splitting reduction ΔE_{ex} as a function of time delay for different laser fluences. The solid lines represent fitting results, from which we extract the three characteristic times for demagnetization (τ_{demag}), fast recovery ($\tau_{recover1}$), and slow recovery ($\tau_{recover2}$) (see Materials and Methods). The fit to TMOKE (upper panel) and ARPES (lower panel and lower fluence) yields the same fluence-independent time constants. a.u., arbitrary units. (B) Typical TMOKE asymmetry before ($t_d = 360 \text{ fs}$) and after ($t_d = 500 \text{ fs}$) excitation with a pump fluence $F = 6 \text{ mJ/cm}^2$. (C) Photoelectron spectra of Ni(111) along the Γ - K direction before ($t_d = 500 \text{ fs}$) and after ($t_d = 500 \text{ fs}$) laser excitation, showing the collapse in the exchange splitting E_{ex} after excitation (blue dashed lines). The dashed-dotted lines represent the momentum at which photoemission intensities are extracted. The photoemission intensities are plotted in the right panel with E_{ex} extracted from a Voigt function fit to the data (dashed lines; see the Supplementary Materials). (D) Constant, fluence-independent demagnetization time observed for different laser fluences for both ARPES and TMOKE.

E_{ex} obtained in Tr-ARPES directly represents the quenching of the magnetization in the material, although the dynamics are obtained at a specific momentum.

In time-resolved ARPES, the dynamic electron temperature can be directly extracted by analyzing the photoemission intensity distribution above E_F . In Fig. 4.3A, we plot the photoemission intensity from above E_F at different time delays, for a fluence of 6 mJ/cm². Before the pump pulse arrives ($t_d = 500$ fs), the photoemission intensity corresponds to a Fermi-Dirac distribution across E_F at room temperature. The electron temperature reaches its maximum value at 24 fs after the peak of the pump pulse and then rapidly decreases due to cooling to the lattice. By 2 ps after excitation, the electron temperature is close to room temperature, as evidenced by the fact that the slope of photoemission intensity as a function of energy is very close to that obtained in the ground state ($t_d = 500$ fs) (Fig. 4.3A). The electron temperature can be reliably extracted by fitting the photoemission intensity with the Fermi-Dirac function convolved with the experimental energy resolution (see the Supplementary Materials). The time evolution of the electron temperature after laser excitation is plotted in Fig. 4.3 (B and C). These results are further corroborated by the dynamics of electron population at 0.2 eV (Fig. 4.3B) and the transient EUV reflectivity measurements performed at similar laser fluences (Fig. 4.3C). These measurements probe the charge dynamics around E_F averaged over the entire Brillouin zone, by exciting the 3p core level electrons of Ni to electronic states around E_F (see inset of Fig. 4.3C). The agreement between the transient electron temperatures extracted from both ARPES and EUV reflectivity measurements suggests that the measured electron dynamics across E_F are uniform throughout k-space. The short electron thermalization time in Ni is not surprising if we consider that the lifetime of photoexcited electrons at 1.6 eV above E_F is extremely short (1 fs) (23), indicating very strong electron-electron interactions (see the Supplementary Materials) (24).

In Fig. 4.4A, we plot the maximum electron temperature extracted around 20 fs, which is the characteristic time scale for the rise of the electron temperature after excitation, as a function of the laser pump fluence. Here, we observe the first critical behavior: The increase of the electron temperature is strongly suppressed around the critical fluence $F_c \approx 2.8$ mJ/cm², indicating that a

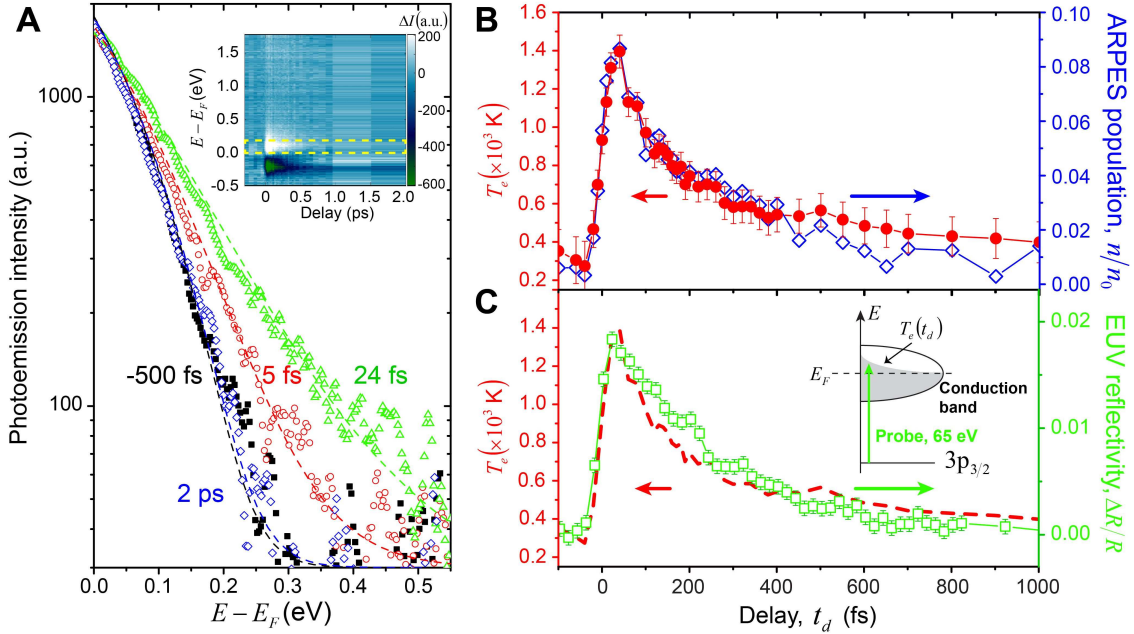


Figure 4.3: Ultrafast charge dynamics in Ni. (A) Log plots of the photoemission intensity above EF for $F = 6 \text{ mJ/cm}^2$ and at different t_d , integrated from $k \approx 0.85\text{\AA}^{-1}$ to $k \approx 1.3\text{\AA}^{-1}$ in the momentum space. The dashed lines represent the fitting of the photoemission intensities with the Fermi-Dirac distribution convolved with experimental energy resolution (see the Supplementary Materials). Inset: Integrated photoemission intensity as a function of pump-probe time delay. The yellow dashed box illustrates the integration region of electron population in (B). (B) Dynamics of the electron temperature and the relative electron population (n/n_0) within 0.2 eV above E_F as a function of t_d . The electron population is normalized to the band electron population (n_0) 0.2 eV below E_F (see the Supplementary Materials). (C) Comparison of the electron temperature [red dashed line, same as (B)] and the change of EUV transient reflectivity at a similar pump fluence. Inset: EUV transient reflectivity measurement. The resonant EUV light (65 eV) directly probes the charge dynamics around EF induced by the laser pump pulse. This measurement is averaged over k-space

significant amount of energy is transferred into the spin system within 20 fs, preventing a further increase in electron temperature. The critical behavior of the peak electron temperature (Fig. 4.4A) can be explained by the divergence of the heat capacity of the strongly coupled electron and spin systems in Ni.

To a first-order approximation, the maximum temperature that the electrons can reach (T_{max}) at the sample surface with a given pump fluence (F) can be calculated as:

$$\text{??} \frac{F(1-R)}{\delta} = \int_{T_e^{max}}^{T_B} [C_e(T) + C_m(T)]dT \quad (4.1)$$

where R is the reflectivity, d is the penetration depth, T_B is the ground state sample temperature, and C_e and C_m are the heat capacities of the electron and spin systems of Ni, respectively. It is well known that the magnetic heat capacity C_m diverges when the temperature approaches the Curie temperature to fulfill the energy required for the ferromagnetic-to-paramagnetic phase transitions under thermal equilibrium conditions (1, 25). Here, we model $C_e(T) + C_m(T)$ using a power-law function and fit the measured peak electron temperature as a function of pump fluence to Eq. (see Materials and Methods and the Supplementary Materials). The fitting results are shown as the solid line in Fig. 4.4A, which essentially captures the critical behavior of the peak electron temperature observed in our experiments. The parameters for the optimum fitting are listed in Table 1, whereas the corresponding transient heat capacity is plotted in the inset of Fig. 4.4B. We find that the divergence in the heat capacity around the critical temperature (T_c) can quantitatively explain the critical behavior observed in the electron temperature. T_c obtained for the ultrafast transient phase transition is very close to the Curie temperature (see Table 1), which further corroborates that the critical phenomena we observed are related to the intrinsic magnetic properties of Ni. The peak electron temperatures with the contribution of electron heat capacity alone are plotted as the dashed line in Fig. 4.4A (see Materials and Methods and the Supplementary Materials). We estimate that there is an energy of $\Delta E_s = \frac{\Delta F_s(1-R)}{\delta} \approx 105$ meV per unit cell transferred to the spin bath within 20 fs. This energy is enough to go through the magnetic phase transition because it is even higher than the energy required under thermal equilibrium conditions (68 meV per unit

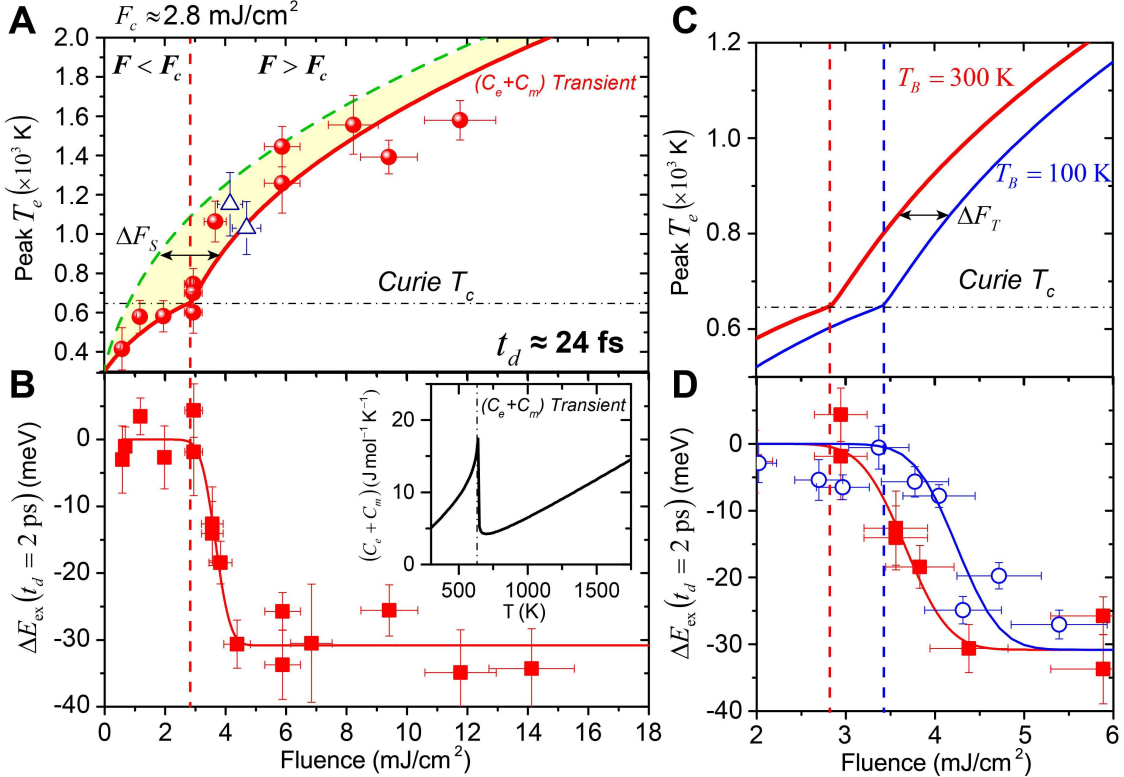


Figure 4.4: Observation of multiple critical behaviors during ultrafast demagnetization in Ni. (A) Peak electron temperature extracted 24 fs after excitation as a function of pump fluence. The open symbols represent the electron temperature extracted at different $k//$ using Tr-ARPES. The solid red line is the fit using Eq. 1 considering the transient electron and magnetic heat capacity [inset of (B)], whereas the green dashed line considers only the contribution from transient electron heat capacity (see the Supplementary Materials). The yellow-colored region (ΔF_S) is the energy transferred to the spin system within 20 fs. (B) Change in the exchange splitting at 2 ps as a function of pump fluence. The red line represents a fit with an error function. The same critical fluence of $F_c \approx 2.8 \text{ mJ/cm}^2$ is observed for the exchange splitting collapse and the peak electron temperature in (A). The transient electron heat capacity is plotted in the inset. (C) Peak electron temperature calculated using Eq. 1 and $(C_e + C_m)$ Transient [inset of (B)] for the sample temperatures of 300 and 100 K. The red solid line is the same as in (A). (D) Change of exchange splitting at 2 ps as a function of laser fluence at different sample temperatures. The solid lines represent the error function fit of the experimental results. The dashed lines align the critical fluences observed in (C) and (D) for different sample temperatures.

cell) (25).

As noted above, the slow recovery of the magnetization is only observed when the pump fluence is higher than the same critical fluence $F_c \approx 2.8\text{mJ/cm}^2$, which represents the second critical behavior. This can be illustrated if we plot the exchange-splitting collapse ΔE_{ex} at $t_d = 2\text{ ps}$ as a function of pump laser fluence, as shown in Fig. 4.4B. We note that the observed critical fluence here is consistent with that shown in Fig. 4.4A for the electron temperature, corroborating that the observed critical behavior of the transient electron temperature is related to the laser-induced magnetic phase transition in the spin-electron system. Considering that the electron and lattice temperatures are both less than the Curie temperature of Ni at $t_d = 2\text{ ps}$ (see below), our results indicate that a transient paramagnetic-like state exists when the pump fluence is above F_c , which recovers through a path distinctly different from the fast recovery for lower pump laser fluences. We note that the different time scales observed in many magnetic spectroscopy experiments to date (3, 15) can be explained by depth averaging, where parts of the material near the surface undergo a transient magnetic phase transition with slow recovery dynamics, whereas layers deeper within the material exhibit faster recovery dynamics. This was confirmed by comparing an extensive set of fluence-dependent time-resolved ARPES and TMOKE data that show that the same critical behavior can explain the entire data set (26).

To further investigate the driving mechanisms for the observed critical phenomena during ultrafast laser-induced demagnetization, we repeated the same measurements for a sample temperature of 100 K using Tr-ARPES. Figure 4.4D plots the change of exchange splitting at a time delay of 2 ps as a function of pump fluence for sample temperatures of 300 and 100 K. The peak electron temperatures reached for those same sample temperatures are calculated using Eq. 1 and are shown in Fig. 4.4C. For a sample temperature of 100 K, the required critical fluence increases by $\Delta F_T = 0.58\text{mJ/cm}^2$ compared to room temperature (Fig. 4.4D). As shown in Fig. 4.4C, this offset can be precisely captured by Eq. 4.1 using the same transient heat capacity (inset of Fig. 4.4B), thus further validating the extracted value of this transient heat capacity. This result strongly suggests the following criterion for critical behavior in ultrafast demagnetization of

Ni: whether or not the transient electron temperature exceeds the Curie temperature. Hence, in our work, the critical fluence corresponds to the fluence required to drive the transient electron temperature above the Curie temperature. We believe that the fact that the critical temperature observed in ultrafast demagnetization is very close to the Curie temperature under thermal equilibrium cannot be a simple coincidence but underscores the importance of the connection between the nonequilibrium physics and its equilibrium counterpart. Similar ideas were recently explored by studies on the ultrafast spin-density-wave transition in Cr (27). However, in that case, the spin-density-wave phase transition occurs immediately when the transient electron temperature reaches the critical point. In contrast, in our work, critical spin excitations occur within 20 fs, and the ferromagnetic-to-paramagnetic phase transition then happens on a longer time scale that is characteristic of the material. We believe that these mechanisms are broadly applicable to many different materials that undergo phase transitions at a critical temperature, for example, superconductors and charge-density-wave materials.

4.3 Discussion

Our results also shed light on the microscopic time evolution of electron spins during ultrafast demagnetization in Ni. The presence of critical behaviors in the electron temperature and heat capacity shows that, within 20 fs after excitation, the spin system in Ni has already absorbed sufficient energy to go through the ferromagnetic-to-paramagnetic phase transition, without yet exhibiting significant demagnetization. This time scale is much shorter than the time scale of demagnetization (TMOKE) and collapse of the exchange splitting (ARPES) (176 fs). The very large difference between these two time scales indicates the importance of a highly nonequilibrium transient state before the sample reaches maximum demagnetization. The initial transferred energy must be stored in the spin system in the form of high-energy spin excitations, leaving the spin system in a nonequilibrium state. Then, this energy likely decays into low-energy magnons over time, leading to demagnetization of the sample in 176 fs. In this picture, the time scale and critical fluence of the demagnetization is intrinsic to the material itself and is determined by the Curie

temperature, heat capacity, and exchange energy. This is strongly supported by the fact that the time constant of demagnetization in Ni (176 fs) is independent of pump laser fluence, as shown by both the Tr-ARPES and Tr-TMOKE measurements (Fig. 4.2D). It has been suggested both experimentally and theoretically that the emission of low-energy magnons on a time scale often of femtoseconds could have significant contributions to ultrafast demagnetization in ferromagnetic materials (7, 17, 2830). Finally, we note that our results cannot be explained by the models based on spin-flip scattering, because, in those models, the demagnetization of the material occurring in several hundred femtoseconds is driven by the gradual transfer of the energy from hot electrons to electron spins via spin-orbit and electron-phonon interactions (3, 5, 8, 15). Moreover, these mechanisms should give rise to a fluence-dependent demagnetization and recovery times.

Now, an important question remains what is the mechanism that could lead to high-energy spin excitations during the first 20 fs? On this time scale, we believe that superdiffusive spin currents could be an important candidate, considering the significant difference between the lifetimes of the majority and minority electrons at 0.2 eV above EF (10, 11), as well as the extremely short time scale of spin transport (1fs over 1-nm distance). However, it has also been shown both experimentally (31, 32) and theoretically (16, 18, 33) that the spin mixing via spin-orbit coupling can happen in a very short time, which might also contribute.

Furthermore, another interesting finding is that, as evidenced by the critical behavior of ΔE_{ex} in Fig. 4.4B, because the spin system recovers to the ground-state magnetization, two different recovery regimes exist, depending on the pump fluence. We note that this is the first time that such a critical behavior in the ultrafast decay and recovery time scales has been observed in ferromagnetic metals such as Ni. As noted above, the demagnetization and exchange-splitting collapse times are fluence-independent at 176 fs. However, when the pump fluence is lower than F_c , we find that the magnetization of the sample undergoes a fast recovery to the ferromagnetic phase with a time constant of 500 fs (Fig. 4.2A). This fast recovery might be explained by damping of magnons (the precession of the magnetic moment M) under the exchange field (H_{ex}). The typical damping time is given by $\tau_{damp} = \frac{\hbar}{g\mu_B\mu_0|H_{ex}|\alpha}$ using the Landau-Lifshiz-Gilbert equation (34, 35), where μ_B is

the Bohr magneton, $g \approx 2$ is the Land factor, and α is the damping factor. Considering that $\alpha = 0.065$ (36, 37) and $|H_{ex}| = 939$ T for Ni (38), we find $t_{damp} \approx 580$ fs, which is in quantitative agreement with $\tau_{recover1}$ observed in our experiments. On the other hand, when the pump fluence is above F_c , the sample evolves into a transient magnetic state with low magnetization and H_{ex} is melted (see Fig. 4.2A). As a result, the magnetization must recover by coupling to phonons and the lattice, which occurs over much longer times.

In conclusion, by investigating ultrafast laser-induced demagnetization in Ni using fluence- and temperature-dependent ARPES, TMOKE, and EUV transient reflectivity measurements, we unambiguously show that critical phenomena govern the ultrafast demagnetization response. We find that although demagnetization and the collapse of the exchange splitting occur on the same fluence-independent time scale of 176 fs, sufficient energy for the transient magnetic phase transition has been transferred to the spin system already within 20 fs. Our results suggest the existence of a high-energy nonequilibrium transient magnetic state and that the transient electron temperature alone is responsible for crossing the spin electronic phase transition.

4.4 Materials and Methods

4.4.1 Experimental setups

In the ARPES experiment, photoelectrons from the Ni(111) surface are mapped using 16 eV HHG probe pulses at near-normal incidence (5deg) and collected by a momentum-resolved hemispherical analyzer. The output of a Ti:Sapphire laser amplifier system (KM Labs Dragon) is frequency doubled to 390 nm and used to generate high harmonics with 160 meV energy resolution and well-separated (by 6 eV) harmonic orders that allow us to use the fifth harmonic (16 eV) directly (39). For the TMOKE and EUV transient reflectivity experiments, the harmonics are driven directly with the 780-nm laser. Light near HHG orders 43 and 45, at photon energies of 65 and 68 eV, is used to probe the 3p absorption edge of Ni. For this purpose, the HHG probe beam is reflected from the sample at an angle of 48° from normal, spectrally dispersed by a grating, and

recorded with a charge-coupled device (CCD) camera (9, 11, 30). The sample is fully magnetized in-plane by an electromagnet placed in the transverse geometry (see the Supplementary Materials for more details).

4.4.2 Data analysis

In TMOKE, the sample magnetization is characterized by the change in reflected EUV intensity at the 3p absorption edge for opposite orientations of the initial in-plane magnetization vector. The TMOKE asymmetry (A_s) is then calculated from

$$A_s = \frac{I_+ - I_-}{I_+ + I_-} \quad (4.2)$$

where I_+ and I_- are the reflected EUV intensities for two magnetization directions (9, 40, 41). Details of data analysis of ARPES experiments are presented in detail in the Supplementary Materials. The dynamics of TMOKE asymmetry (A_s) and the change of the exchange splitting (ΔE_{ex}) can both be fit to

$$Y(t_d) = \begin{cases} Y_0 \\ Y_0 + ae^{-t_d\tau_{demag}} - be^{-t_d\tau_{recover1}} - (a - b)e^{-t_d\tau_{recover2}} \end{cases}$$

where Y represents either ΔE_{ex} or A_s , Y_0 is the ground-state signal, and a and b are the amplitudes of the collapse and the first fast recovery of the signal, respectively. τ_{demag} , $\tau_{recover1}$, and $\tau_{recover2}$ are the time constants of the collapse, fast recovery, and slow recovery of the signal, respectively.

4.4.3 Model of electronic and magnetic heat capacity

The electronic and magnetic heat capacity $C_e(T) + C_m(T)$ can be modeled with the following power-law function as it passes through the critical temperature (T_c) (42)

$$C_e(t) + C_m(t) = \frac{A}{\beta}|t^{-\beta}| + B + \gamma t \quad (4.3)$$

where $t = \frac{T-T_c}{T_c}$ is the reduced temperature for $T > T_c$. We used the same function with primed parameters (A' , B') for $T < T_c$. The parameters b , γ , and T_c are kept identical on both sides of the

phase transition. The electronic and magnetic heat capacities under thermal equilibrium conditions (25) can be fit to Eq. 5.2, allowing us to extract parameters A, A, and b, which determine the critical behavior of the heat capacities around T_c . The contribution of the electron heat capacity alone can be estimated under the free-electron gas approximation $C_e = \gamma T$ (see the Supplementary Materials) and gives rise to the modeled peak electron temperature using Eq. 4.1, as shown by the dashed line in Fig. 4.4A. We also noted that in Eq. 4.1, we neglected electron-phonon coupling and heat diffusion; however, these effects have negligible influence on our results in the first 20 fs, as shown in the Supplementary Materials.

4.4.4 Statistical analysis

In both Tr-ARPES and Tr-TMOKE experiments, the data were collected with multiple pump-probe delay cycles to achieve a sufficient signal-to-noise ratio. The exchange splitting dynamics were analyzed by fitting the extracted photoemission spectra with multiple Voigt functions and defined as the energy difference between peaks of electrons with majority and minority spins (see the Supplementary Materials for more details). The error bars in Figs. 4.2A and 4.4 (B and D) were due to uncertainties in the fitting procedure. The transient electron temperature was obtained by fitting the photoemission intensity above E_F with Fermi-Dirac distribution, and the error bars in Figs. 4.3B and 4.4A were due to uncertainties in the fitting procedure, as well as the energy resolution (see the Supplementary Materials). The errors on the pump fluence were due to fluctuations of pump power and laser spot size. The error bars of Tr-TMOKE data in Fig. 4.2 (A and D) were defined by the standard deviation of experimental data before pump excitation.

4.4.5 Details of experimental setups

The detailed experimental setup of Tr-ARPES is shown in fig. S1A. We use a multi-pass Ti:Sapphire laser system to generate 28 fs pulses at a wavelength of 780 nm (1.6 eV) with pulse energy of 2.0 mJ and a repetition rate of 4 kHz. Most of the laser energy (95%) is used for high-harmonic generation (HHG), while a small portion (5%) is used to excite the sample as the pump.

To generate HHG, we send 95% of the laser power into a 200 μm thick β -phase barium borate (BBO) crystal, which produces pulses at a wavelength of \approx 390 nm with pulse energy \approx 0.3 mJ. The residual 780 nm light is removed from the beam path using two dichroic mirrors after the BBO. The 390 nm light is then focused using a lens with 50 cm focal distance into a 1-cm-long capillary waveguide. The waveguide has an inner diameter of 150 μm and is filled with Xe at a pressure of \approx 20 Torr or Kr at a pressure of \approx 60 Torr. The HHG beam is focused onto the nickel sample in the UHV chamber using a toroidal BK7 mirror to a spot size of \approx 100 m in full width of half maximum (FWHM). Any residual driving laser light is blocked by a 200 nm thick polycrystalline Al filter. The excited photoelectrons are collected by a hemispherical electron analyzer. The energy resolution is calibrated using the photoemission spectrum from a polycrystalline Cu at the room temperature and yields \approx 160 meV. For ARPES, the atomically clean Ni(111) surface is obtained in-situ using repeated cycles of Argon ion sputtering (0.5 keV) at room temperature, followed by annealing to 900 K for 15 minutes.

The linearly polarized 780 nm pump beam is recombined collinearly with the HHG beam using an annular silver mirror and focused onto the sample surface. The pump fluence is varied by the combination of a half waveplate and a polarizer, as shown in Fig. 4.5A. The pulse durations of the pump-probe experiment is directly measured in-situ using the laser-assisted photoemission (LAPE) method. In the LAPE measurement, p-polarized pump light is focused onto the sample surface. When the pump pulse temporally overlaps with the HHG-probe pulse, a side band can be clearly observed at an energy 1.6 eV away from the main photoemission peak, which allows us to extract the cross-correlation of the pump and probe pulses. The side band intensity as a function of τ_d obtained from LAPE measurement is shown in fig. S1B. We note that in order to avoid the influence of LAPE signals on our measurements of ultrafast charge and exchanging splitting dynamics, we switch to s-polarized IR pump in the other two measurements.

For the Tr-TMOKE experiments, the experimental layout is given in Fig 4.5C. A regenerative Ti:Sapphire amplifier system is used to generate pulses of up to 1.8 mJ at a repetition rate of 5 kHz. The beam is then split with a 10:1 beamsplitter for use in the pump/probe configuration.

The probe beam is focused with a 50 cm lens into a hollow core fiber with a diameter of 150 μm . The hollow core fiber is filled with He gas at a pressure of 1 Torr, where high harmonics of the fundamental beam are generated. After the harmonics are generated, the beam passes through an iris to remove some of the residual fundamental mode, is reflected by a toroid with an effective focal length of 30 cm, and passes through an aluminum filter of thickness 500 nm. Next, the harmonic beam is rejoined by the p-polarized pump beam, and the two are incident on the sample at an angle of 48 degrees measured with respect to the normal. The timing of the pump beam with respect to the probe is controlled by a mechanical delay stage. The power in the pump arm is controlled by a polarizer and mechanical half waveplate combination (for fluence dependent studies). The FWHM of the pump pulse for both the TMOKE and reflectivity measurements at the location of the sample was determined to be 55 fs by in-situ frequency resolved optical gating measurements. After reflecting off the sample, the HHG probe reflects off a grating (500 lines/mm) placed in the conical mount configuration and passes through two more aluminum filters of thickness 200 nm before being measured by an Andor Newton X-ray CCD detector.

In both experiments, the spot sizes of pump are measured using the knife-edge method in-situ at the sample location. The pump fluence in this work is defined as $F = \frac{4Q}{\pi D_x D_y}$, where Q the is the pump-pulse energy and $D_{x/y}$ is the FWHM of the pump spot along two orthogonal axes. In order to compare the fluence-dependent results between two experiments, the difference in the reflectivity at different incident angles has to be taken into consideration. According to the optical constants of Ni (43), the reflectivity R at normal incidence is ≈ 0.74 , which changes to ≈ 0.64 for the p-polarized pump at an incident angle of 48 degrees measured with respect to the normal. This value is also confirmed by reflectivity measurement on site. The fluence reported in the main text for Tr-TMOKE results are scaled considering this difference to preserve the same absorbed fluence as that in Tr-ARPES measurements. In both experiments, the time solution is estimated to be ≈ 10 fs, considering the fastest changes that can be observed from the data.

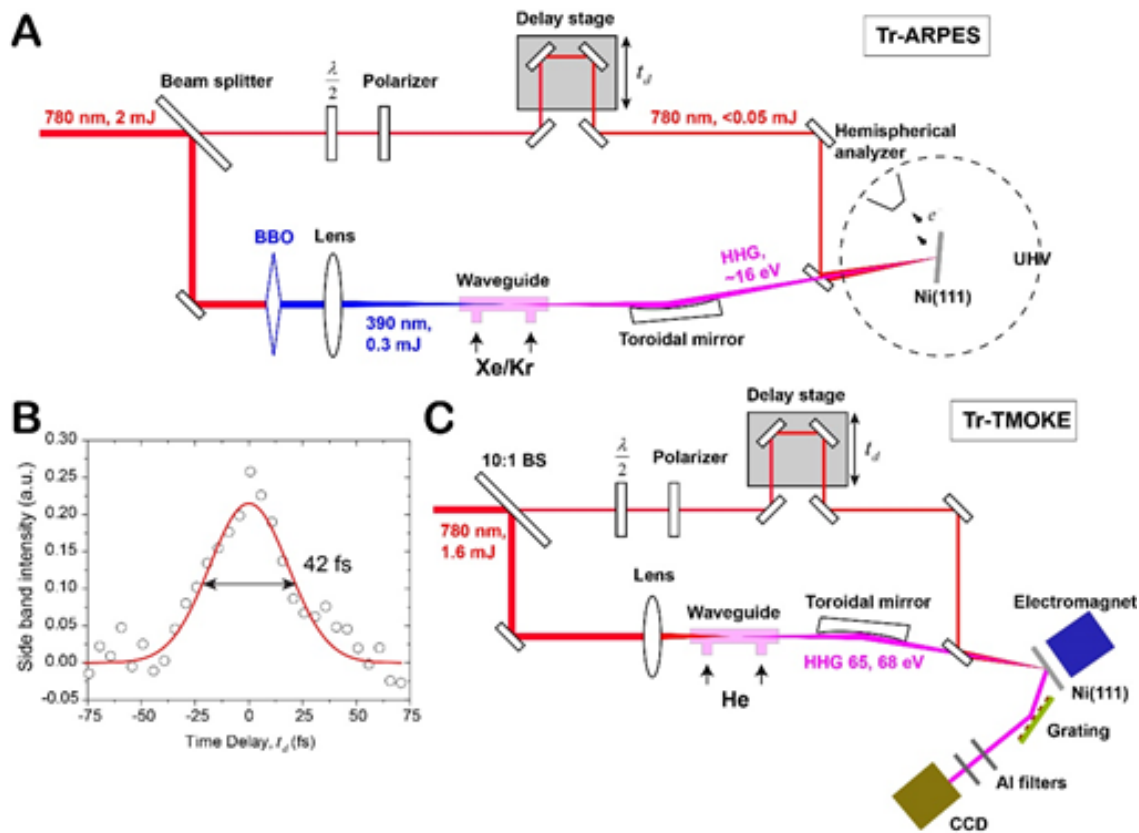


Figure 4.5: Experimental Setup. (A) Experimental setup of Tr-ARPES experiment. (B) Side band intensity as a function of pump-probe time delay in LAPE measurement for Tr-ARPES. The solid line is the fitting result with the Gaussian function with a FWHM of ≈ 42 fs. (C) Experimental setup of Tr-TMOKE experiment.

4.4.6 Dynamics of electron temperature

The photoelectron spectra of Ni(111) along direction are measured using ≈ 16 eV photons from HHG. After Shirley background subtraction (43), the photoemission intensity across E_F can be described by the Fermi-Dirac (FD) distribution multiplied by the density of states of the material. In order to extract the time-dependent electron temperature (T_e), we fit the photoemission intensity (I) integrated from $k \approx 0.85 \text{ \AA}^{-1}$ to $k \approx 1.3 \text{ \AA}^{-1}$ as shown in Fig. 4.6A to the function,

$$I(t_d) = \{A(t_d) \times FD[E_F(t_d), T_e(t_d)] \times DOS[E_F(t_d) - E_B, \sigma_L]\} \times Gauss(\sigma_G) \quad (4.4)$$

where A is the amplitude parameter, FD the Fermi-Dirac function. DOS in Eq. 4.4 is the density-of-states function, modeled as a Lorentzian peak with a peak center at $E_F - E_B$ and a peak width of σ_L . Here, E_B is the binding energy of the state. The function is finally convolved with a Gaussian function (Gauss) with a width σ_G , which represents the energy resolution of ≈ 160 meV in our experiments. The fitting error of the photoemission intensity to Eq. 4.4 is defined as σ_{fit} .

We note that with pump fluences $F \gtrsim 2 \text{ mJ/cm}^2$, the space charge effects caused by surface charging and multi-photon photoemission induced by the IR pump laser are inevitable, and induce time-dependent energy shifts of the photoemission spectra in the Tr-ARPES experiments(45). At the same time, because we are only interested in the photoemission intensity within ≈ 1 eV across EF, the space-charge induced energy shifts in this small energy window can be assumed to be an energy-independent constant. As a result, in Eq. 4.4, we model the Fermi energy E_F as a time-dependent parameter, while the binding energy of the state (E_B) is a time independent parameter. Because the electron temperature T_e is determined by the slope of the FD function across E_F , this fact allows us to mostly decouple T_e from the space-charge induced energy shifts in the fitting procedure.

When fitting the photoemission intensities at different t_d to eq. S1, we first determine the time independent parameters (E_B, σ_L) with the spectrum obtained at t_d before the pump-probe time zero (e.g. $t_d = -500$ fs). Then we can fix these parameters in the following fitting procedures for the other t_d . Typically, $E_B \approx 0.15$ eV and $\sigma_L \approx 0.4$ eV are used for all the data sets. The time

dependent parameters E_F and T_e can be reliably extracted using the fitting procedure described above. The fitting results for $F \approx 6 \text{ mJ/cm}^2$ at $t_d = -500 \text{ fs}$ and 24 fs are shown as an example in Fig. 4.6B and C. The extracted values of E_F also allow us to compensate the pump-induced space charge effect by assuming EF is constant after pump excitation. Indeed, the chemical potential of the majority and minority electrons can be different and shift as the electron temperature varies, but the amount of energy shift is only several meV even with the electron temperature elevated by $\approx 2000 \text{ K}$ (46). The photoemission intensity at different t_d are plotted without the space-charge correction in Fig. 4.6D and with the correction in Fig. 4.6E.

Moreover, the energy resolution of $\approx 160 \text{ meV}$ in our experiments places a lower limit on the electron temperature we can extract from the experiments and this limit has to be considered as part of the errors in our data analysis. In order to determine how much the errors from the energy resolution contribute, we model a FD distribution with a given temperature T_{real} and convolve it with the energy resolution $\approx 160 \text{ meV}$, which is represented by a Gaussian function. A random noise of 2% of the maximum intensity is added to model the realistic data. Then the generated distribution is fit to the same fitting function as Eq. 4.4, but with DOS = 1.0. The electron temperature extracted from this fitting procedure is defined as T_{fit} . We found when the $T_{real} < 200\text{K}$, the fitting procedure we used failed to extract the correct electron temperature, defining the lower limit of the electron temperature we can extract from the experiment with $\approx 160 \text{ meV}$ energy resolution. But this uncertainty is decreased to only $< 10 \text{ K}$ when the electron temperature is above the room temperature (300 K). The energy-resolution-induced uncertainty of electron temperature is also taken into consideration as $\sigma_{res} = |T_{real} - T_{fit}|$ in the final data plotting. The total error of electron temperature (Fig. 4.3B and 4.4A) is defined as $\sigma_{tot} = \sqrt{\sigma_{res}^2 + \sigma_{fit}^2}$. We note that in the temperature range in our experiments ($> 300 \text{ K}$), σ_{tot} has a primary contribution from σ_{fit} .

4.4.7 Dynamics of the electron population at 1.6 eV

The electron population change below and above EF can be directly measured using Tr-ARPES. The change of photoemission intensity taking the ground-state intensity ($t_d = -500 \text{ fs}$)

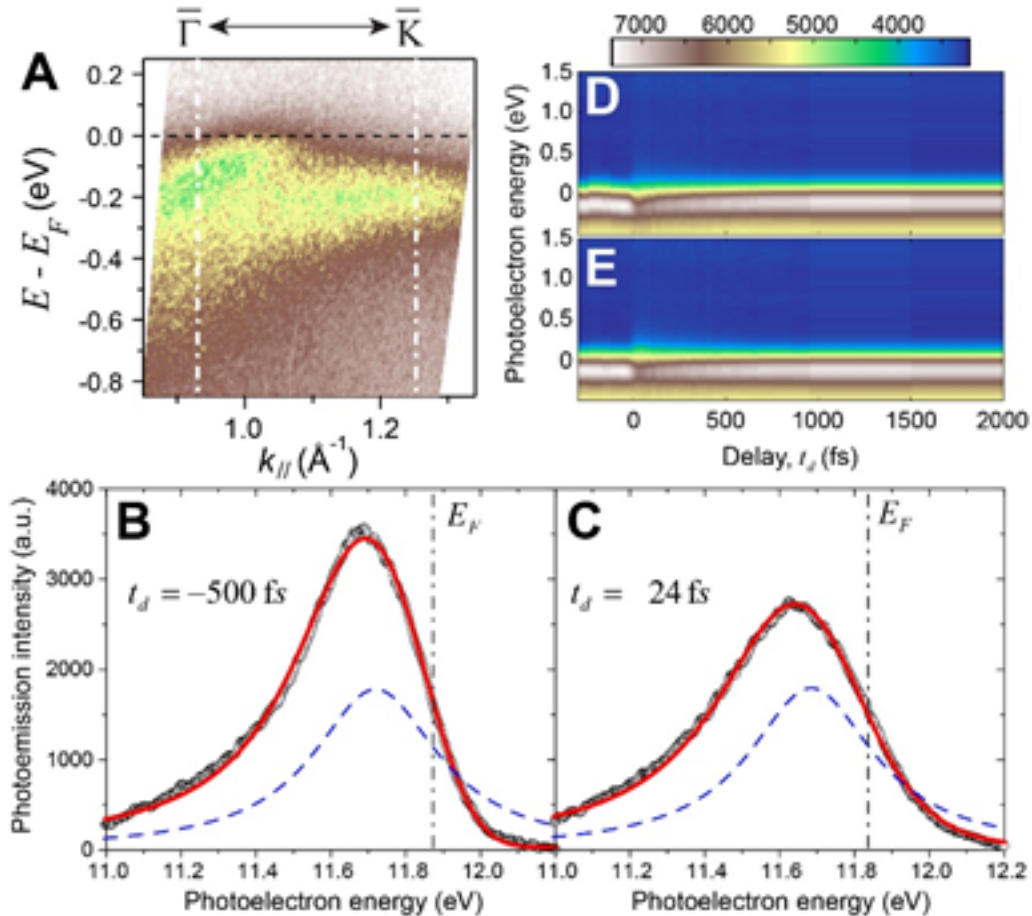


Figure 4.6: Electron temperature fitting. (A) Photoemission spectrum of Ni(111) excited by 16 eV HHG photons at room temperature. The white dash-dotted lines represent the momentum range for the photoemission intensity in the analysis for the transient electron temperature. (B) and (C) Photoemission intensity and fitting results at $t_d = -500$ fs and $t_d = 24$ fs for $F \approx 6$ mJ/cm². The red solid lines are the fitting results using Eq. 4.4 and the blue dashed lines represent the DOS function used in the fitting. The black dashed-dot lines are the Fermi energy obtained from the fitting. (D) Photoemission intensity as a function of pump-probe time delay from the raw experimental data. (E) Same as (D), but the E_F shifts due to pump-induced space charge effects are corrected.

as the reference is plotted in Fig. 4.7A. We extract the electron population dynamics in two different regions with $\Delta E = 0.2$ eV as the size of energy window at: (a) $E = 0.1$ eV and (b) $E = 1.6$ eV, as shown in Fig. 4.7A. The change of electron population is measured by the integrated photoemission intensity in each energy window, taking the values before pump-probe time zero as the reference: $\Delta n(t_d) \propto \int_{\Delta E} I(E, t_d) dE - \int_{\Delta E} I(E, t_d < 0) dE$. We also normalize n to the electron population of nickel in the conduction band before the time zero: $n_0 \propto \int_{\Delta E} I(E = -0.1, t_d, 0) dE$. $\Delta n/n_0$ for regions (a) and (b) with pump fluence $F \approx 6$ mJ/cm² is plotted in fig. 4.8B. We find while the population change at $E=0.1$ eV reaches 8% of the ground state band electron population density, the increment at $E=1.6$ eV is only $\approx 0.8\%$ in maximum.

The electron density directly excited by the IR pump laser can be calculated by $\Delta n = \frac{F(1-R)}{\delta \hbar \omega}$ assuming single-photon excitation, where F is the pump fluence, R the reflectivity, δ the skin depth and $\hbar \omega = 1.6$ eV the photon energy. The values of R and δ are given in table S1. We find the electron density directly excited by pump photons is ≈ 4.5 nm⁻³ for the pump fluence of ≈ 6 mJ/cm². This value corresponds to $\approx 0.55\%$ of the d band electron density in nickel, if we consider there are 9 d electrons per nickel atom, which is in good agreement with the value we obtained at $E = 1.6$ eV above E_F . From Fig. 4.7B, we find that the electron population at $E = 1.6$ eV rises at the same time as those at $E=0.1$ eV and its population is only $\approx 0.8\%$ of the band electrons, excluding strong influence directly from the photo-excited non-equilibrium electron population to our electron temperature measurement. Our results suggest the electron bath in nickel thermalizes in a very short time after pump excitation, consistent with strong electron-electron interactions reported in previous works (23, 24).

4.4.8 Dynamics of Exchange Splitting

The exchange splitting can be clearly resolved at $k \approx 1.05 \text{\AA}^{-1}$ in the photoemission spectra excited by ≈ 16 eV HHG photons as shown in Fig. 4.6C of the main text. In order to extract the exchange splitting and improve the signal to noise ratio in the data analysis, the photoemission intensity is extracted along the direction normal to the band dispersion (≈ 10 deg tilted from the

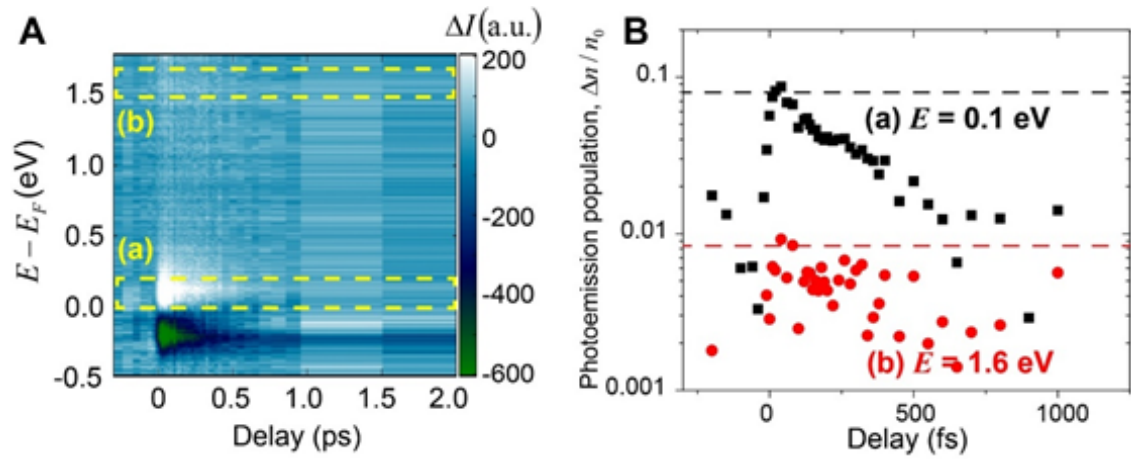


Figure 4.7: Electron population dynamics. (A) The relative change of photoemission intensity as a function pump-probe time delay, taking the intensity before pump excitation ($t_d = -500$ fs) as the reference. The yellow dashed boxes represent the two regions of energy where the changes of electron population are extracted. (B) Normalized electron population as a function of pump-probe time delay extracted from (a) and (b) regions in (A).

constant momentum direction) as shown in Fig. 4.8A and B. The photoemission intensity (I) after Shirley-background subtraction (43) is hence fitted to the function

$$I(E) = \sum_{m=1,2,3} A_m \times V(E; E_m^0, \sigma_m^G, \sigma_m^L) \quad (4.5)$$

where E is the photoelectron energy, m represents the index of the Voigt functions, $V(E; E_m^0, \sigma_m^G, \sigma_m^L)$ is the normalized Voigt function with E_m^0 the center energy, σ_m^G the Gaussian width and σ_m^L the Lorentzian width of the m^{th} Voigt function, and A_m is the amplitude of the m^{th} Voigt function. The typical fitting results of photoemission intensity are shown in Fig. 4.8C-F for fluence below and above F_c and at different times. As shown in Fig. 4.8C, the first Voigt peak ($m=1$) represents a low energy d band with a binding energy of ≈ 0.6 eV, which does not change after pump excitation. The second and third Voigt peaks ($m=2, 3$), on the other hand, correspond to the majority and minority d bands that cross the Fermi energy at $k \approx 1.05 \text{\AA}^{-1}$ (20). When fitting the results to extract the exchange splitting change as a function of pump-probe time delay, we 1) fix the Gaussian width of all Voigt peaks considering the energy resolution of ≈ 160 meV; 2) fix the parameters of the third Voigt function ($m=3$) and the width of the second Voigt function ($m=2$), using the values obtained from the ground-state fitting ($t_d = -500$ fs). As a result, we have 5 fitting parameters ($A_1, E_1^0, \sigma_1^L, A_2, E_2^0$) and the exchange splitting is defined and extracted as $E_{ex} = E_1^0 - E_2^0$. The extracted E_{ex} is 240 meV in the ground state, which is consistent with previous works at a similar Brillouin-zone (BZ) point (20).

We note that our analysis shows that E_{ex} does not vanish after pump excitation. (Same as the sample is heated up across the Curie temperature, see below.) It has been shown that the absolute value of exchange splitting measured in the spin-integrated photoemission depends on the model and the fitting strategy(46). In our work, the 160 meV energy resolution, as well as the fitting model in which two peaks (majority and minority bands) are always assumed to exist, post the limit of our ability to resolve the collapse of the exchange splitting beyond $\Delta E_{ex} = 60$ meV. In order to extract reliable dynamics of the exchange splitting, we consistently used the same fitting strategy as described above for different time delays as well as different fluences.

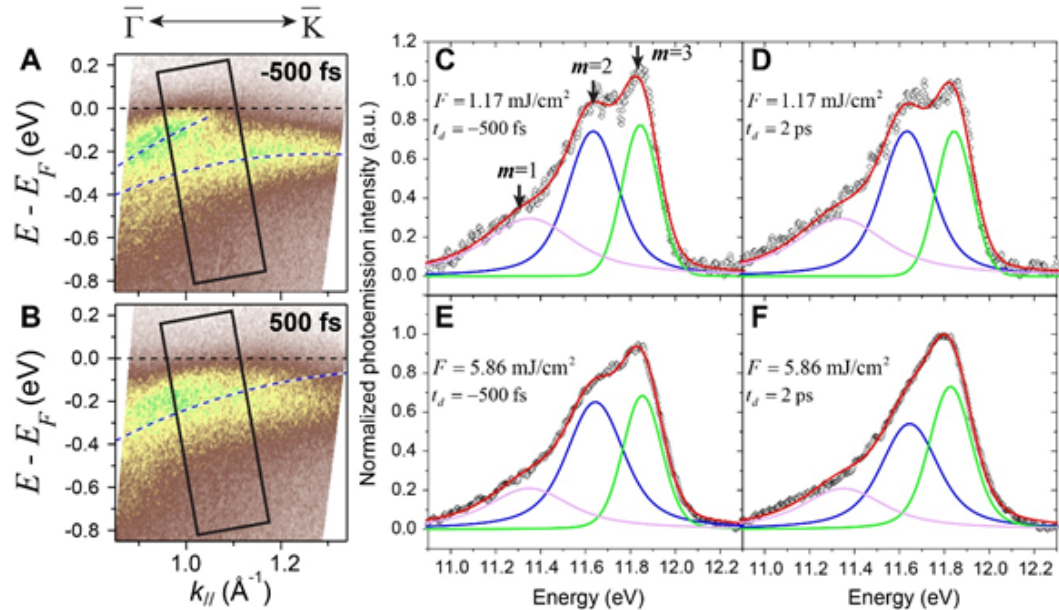


Figure 4.8: Analysis of exchange splitting. (A) and (B) Photoemission spectra of Ni(111) before ($t_d = -500$ fs) and after ($t_d = 500$ fs) pump excitation. The solid black boxes represent the regions the photoemission intensities are extracted for the analysis on the exchange splitting. (C)-(D) The photoemission intensities and the Voigt function fitting (Eq. S2) results for different pump fluences and different pump-probe time delays. The red lines are the overall fitting results. The Cyan, blue and green curves represent the extracted Voigt peaks for $m=1$, 2 (majority band) and 3(minority band).

The fact that the extracted dynamics of exchange splitting can agree with the demagnetization process measured using Tr-TMOKE method (Fig. 4.2A and D) also validates our fitting strategy and strongly suggests that the dynamics of E_{ex} can represent the dynamics of magnetization after pump excitation. At the same time, the difference of exchange splitting for fluence below and above F_c at $t_d = 2$ ps can be clearly resolved from the raw experimental data as shown in Fig. 4.8D and F.

The change of the exchange splitting (ΔE_{ex}) as a function of t_d under different pump fluence are fit to Eq. 3.2. We find the results can be fit with a set of universal time constants: $\tau_{demag} = 176 \pm 27$ fs, $\tau_{recover_1} = 537 \pm 173$ fs and $\tau_{recover_2} = 26 \pm 11$ ps, as plotted in Fig. 4.9.

4.4.9 Temperature dependence of exchange splitting in static ARPES

The static photoelectron spectrum along direction measured using He I α photons ($h\nu = 21.218$ eV) from helium discharge lamp at room temperature is shown in Fig. 4.10A. The exchange splitting (E_{ex}) between the majority and minority bands of Ni can be clearly observed at the momentum $\approx 1.05 \text{ \AA}^{-1}$ where its d band crosses the Fermi energy (E_F). The values of E_{ex} can be quantitatively extracted using the same fitting procedures described in the previous section. We find E_{ex} reduces as the sample temperature approaches the Curie temperature (631 K) as shown in Fig. 4.10B, indicating the quenching of the local magnetic moments (1, 20).

4.4.10 Method for extracting TMOKE asymmetry dynamics from HHG spectra

In the Tr-TMOKE experiment, to extract the asymmetry dynamics at the nickel edge, we use a spectrometer as shown in Fig. 4.5C. We take an average of the signal over an energy range of the spectrometer approximately equal to 1.2 eV for each harmonic, although we note that this width is also convolved with the spot size of the HHG beam after reflection off the grating. We select the harmonics corresponding to the 43rd and 45th harmonic of the fundamental laser (corresponding to energies of 65 and 68 eV) in the data analysis procedure. Finally, we normalize the data before the pump pulse arrives by taking the average value of the static asymmetry. We use the standard

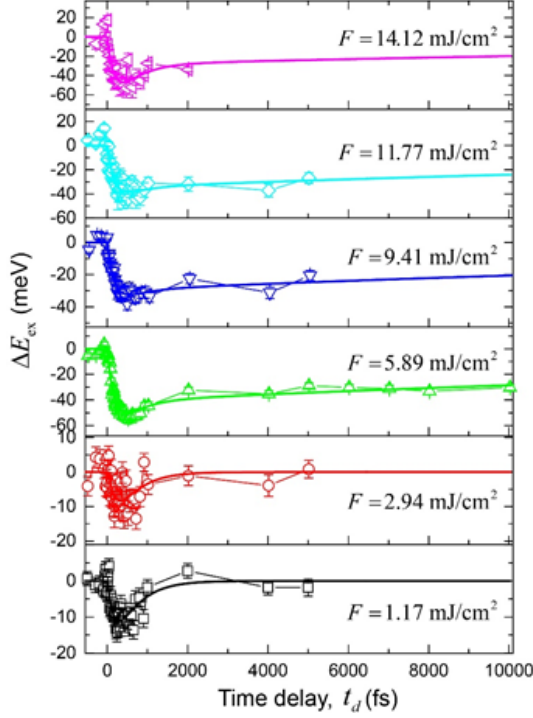


Figure 4.9: Global fitting of the exchange splitting dynamics. The global fitting results of the exchange splitting dynamics to Eq. 4.2 for a range of pump fluences ($F = 1.17 \text{ mJ/cm}^2$ to $F = 14.12 \text{ mJ/cm}^2$).

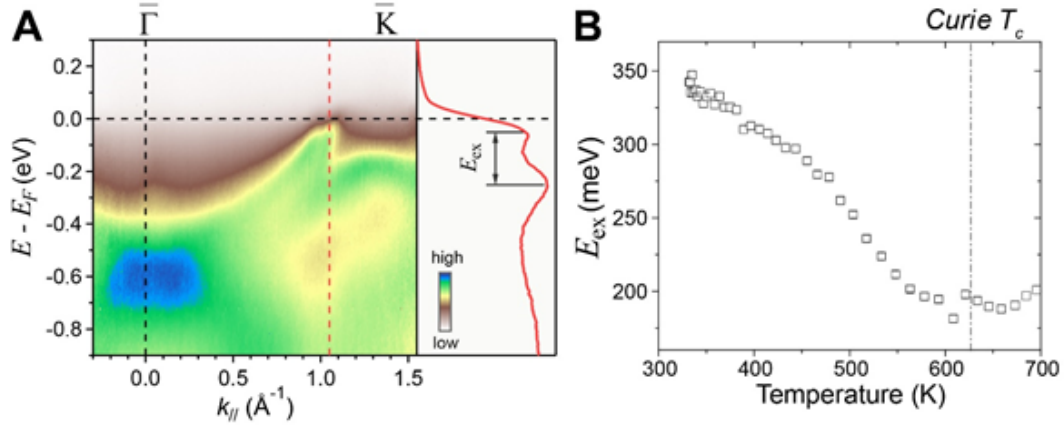


Figure 4.10: Collapse of exchange splitting at the Curie temperature. (A) Static photoemission spectrum excited by He I α photons ($h\nu = 21.218 \text{ eV}$) at the room temperature. Right panel: Energy distribution curve extracted at the momentum where the red dashed line is located. The exchange splitting (E_{ex}) can be clearly extracted using fitting procedure described in the previous section. (B) E_{ex} change reduces as the sample temperature increases.

deviation in values for static asymmetry measured before the sample is pumped to determine the error bars for the TMOKE measurement.

4.4.11 Momentum dependence of TMOKE Measurements

In order to investigate the momentum dependence of the Tr-TMOKE measurements, we took several different time-resolved asymmetry measurements with different crystal lattice orientations relative to the applied field B , with an incident pump fluence of 2.8 mJ/cm^2 . These measurements are shown in Fig. 4.11. These results clearly show the momentum-averaged nature of the Tr-TMOKE measurement.

4.4.12 Transient electron and magnetic heat capacity

The electron and magnetic heat capacity is modeled using Eq. 5.2 with six parameters (A , A' , B , B' , β , γ and T_c). In order to reduce the number of free fitting parameters, we first determine the values of A , A' and β by fitting the electron and magnetic heat capacity under thermal equilibrium (25) to Eq. 5.2. The fitting results are plotted in Fig. 4.12A. By doing so, we assume the order parameters for the critical behavior of heat capacities are preserved in laser-induced phase transition. At the same time, the fact that the total heat capacity at $T=0$ is zero places an additional confinement on the parameters: $\frac{A'}{\beta} + B'\gamma = 0$. As a result, we have in total three free fitting parameters when we fit the experimentally measured T_e (Fig. 4.4) to Eqs. 4.4.2 and 5.2. The critical behavior of the nickel heat capacity represents the energy transfer into the spin bath when the system crosses the ferromagnetic-to-paramagnetic phase transition. In transient ($C_e + C_m$), the contributions of the electron heat capacity can be estimated under the free-electron-gas approximation: $C_e = \gamma' T$, as shown in Fig. 4.12B. We note that when $T < T_c$, γ' is close to the value for thermal equilibrium (25). However, we find γ' is about 3 times larger than its thermal equilibrium counterpart when $T > T_c$, the reason of which requires further investigations. Using the transient C_e and Eq. 4.4.2 in the main text, we can estimate the peak electron temperature without spin contributions, which is shown as the pink dashed line in Fig.

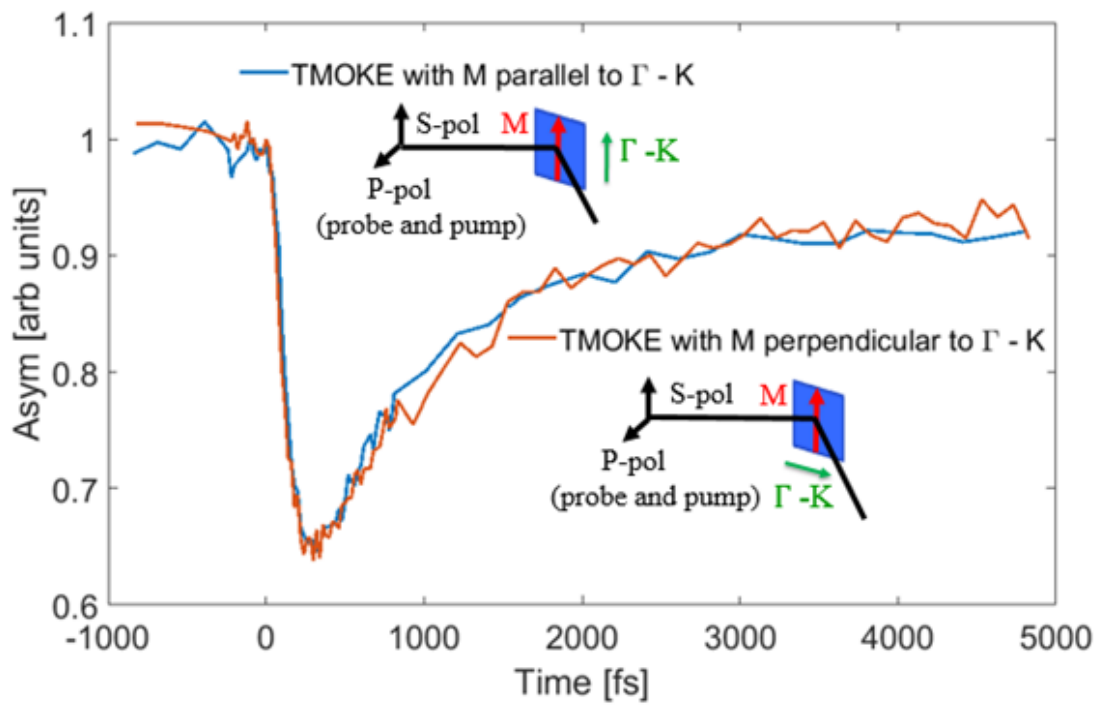


Figure 4.11: Momentum dependence of TMOKE measurements. The TMOKE asymmetry dynamics for different crystal orientations. Inset: Illustrations of the relative orientations of the crystal cut relative to the directions of the magnetic field and light polarizations in the experimental geometry.

4.4A. The offset in fluence of this curve to the experimentally measured peak electron temperature represents the amount of pump energy (ΔF_S) transferred to the electron spin bath in ≈ 20 fs.

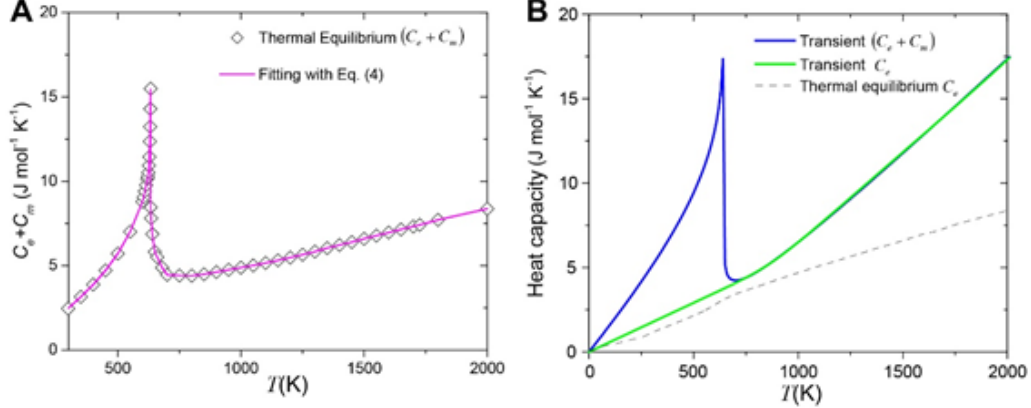


Figure 4.12: Electron and spin heat capacity. (A) The electron and magnetic heat capacity under thermal equilibrium (25). The solid line is the fitting result to Eq. (4) in the main text. (B) The transient electron and magnetic heat capacity extracted from our experimental results. The green line represents the contribution of the electron bath to the total heat capacity. The dashed line is the electron heat capacity under thermal equilibrium for comparison (25).

4.4.13 Effects of electron-phonon coupling and heat diffusion on Eq. 4.1

In Eq. 4.1, we ignored the heat diffusion and electron-phonon coupling that could reduce the electron temperature at the surface measured using Tr-ARPES method. These two effects can be explicitly considered using two-temperature model (TTM)(47). The time (t)- and space (z)-dependent evolution of the electron (T_e) and lattice temperatures (T_l) is described by

$$\begin{aligned} C_{em} - \frac{\partial T_e}{\partial t} &= -\frac{\partial}{\partial z} Q_e - G(T_e - T_l) + S(z, t) \\ \tau_e \frac{\partial Q_e}{\partial t} + Q_e &= \kappa_e \frac{\partial}{\partial z} T_e \\ C_l \frac{\partial T_l}{\partial t} &= G(T_e - T_l) \end{aligned}$$

where Q_e is the heat flux of electrons, G the electron-phonon (e-ph) coupling constant, τ_e the electron energy relaxation time, $\kappa_e = \kappa_{e0} \frac{T_e}{T_l}$ the electron thermal conductivity and C_l the lattice

heat capacity. In Eq. 4.6, the heat diffusion through lattice is neglected, because the lattice thermal conductivity (κ_l) is much smaller than κ_e . The values of τ_3 , κ_{e0} and C_l of Ni can be determined by previous literature(48) as well as material parameters, and are listed in Table S1. We note that τ_e varies from ≈ 20 fs to 1 fs as the electron energy rises from 0.2 eV to 1.5 eV above E_F (23). This value is shorter than the pump pulse duration (≈ 28 fs). As a result, the dynamics of electron and lattice temperature have very weak dependence on the choice of τ_e . For convenience, we use $\tau_e = 10$ fs in all the simulations. In Eq. 4.6, the pump laser pulse is modeled as

$$S(z, t) = \sqrt{\frac{4 \log 2}{\pi}} \frac{(1 - R)F}{t_p \delta} \times \exp \left[-\frac{z}{\delta} - 4 \log 2 \left(\frac{t}{t_p} \right)^2 \right] \quad (4.6)$$

where F is the pump fluence, R the reflectivity, δ the IR-light penetration depth and t_p the pump pulse FWHM width. The values of δ and t_p are also listed in Table S1. The heat capacity C_{em} in Eq. 4.6 is defined as the total heat capacity of the electron and spin systems ($C_e + C_m$). In the simulation, we use the temperature-dependent transient ($C_e + C_m$) as plotted in the inset of Fig. 4.4B. This choice is validated by the fact that the electron and spin systems are found to be strongly coupled in short time after pump excitation, evidenced by the critical behavior of the electron temperature at ≈ 24 fs as shown in Fig. 4.4A. The coupled differential equations in Eqs. 4.6 and 4.6 are numerically solved using MacCormack method. In Fig. 4.13A, the simulation results of T_e averaged over 1 nm under the sample surface are plotted in direct comparison with the electron temperature measured using Tr-ARPES in our experiments. We find very good agreement can be achieved for a range of pump fluence when a proper temperature dependent e-ph coupling constant G is implemented. The value we used here is a factor of 3 stronger than values reported in Ref. (49). Very interestingly, we find the TTM simulations results show that there exists a kink in the recovery dynamics of the electron temperature, whenever the electron temperature reduces to the critical temperature. This reproduces our experimental data very well, which in the time domain strongly supports that the transient electron and magnetic heat capacity influences the laser-induced dynamics. On the other hand, in order to account for the dynamics of the EUV reflectivity, the electron temperature averaged across the EUV probing depth (10 nm) has to be

taken into consideration, as shown in Fig. 4.13B.

The calculations using TTM also allow us to investigate the contributions from heat diffusion and electron-phonon coupling to the model in Eq. 4.1. In Fig. 4.13C, we plot the T_e obtained from TTM simulation for 1) thermally isolated, same as Eq. 4.1, by setting $\kappa_e = 0$ and $G = 0$, 2) heat diffusion only, by setting $G=0$ and $\kappa_e \neq 0$ and 3) heat diffusion and e-ph coupling with $G \neq 0$ and $\kappa_e \neq 0$. From the results, we can see that the surface electron temperature could be reduced by less than 100 K within 20 fs through heat diffusion when the sample is pumped by a relatively high fluence (5.8 mJ/cm^2). This value is expected to be much smaller at lower pump fluences. In contrast, the e-ph coupling has negligible effects on electron temperature in 20 fs, because the characteristic time of e-ph coupling is on a time scale of $\approx 100 \text{ fs}$. At the same time, we can also investigate whether the convolution with the time-resolution of our measurement could affect the electron temperature measurements (dashed line in Fig. 4.13C). We find the time resolution of our experiment is sufficient to precisely capture the electron temperature in very short time scales.

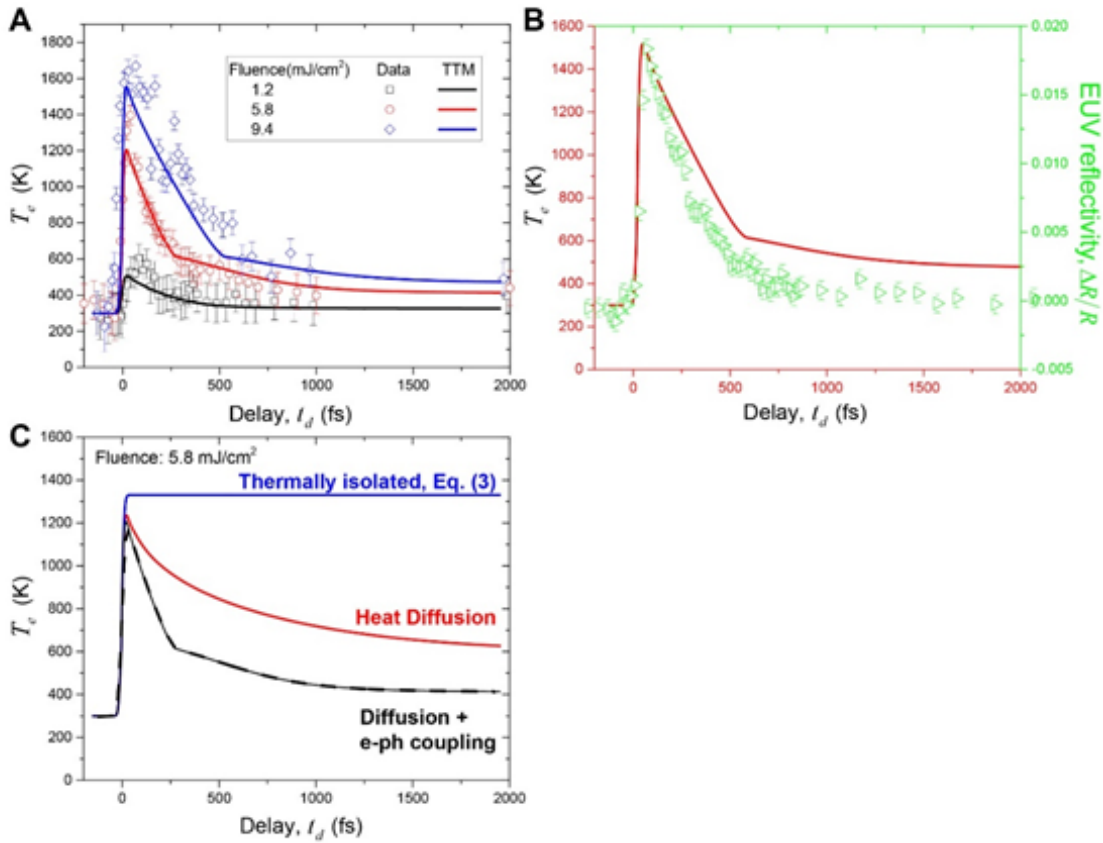


Figure 4.13: Two-temperature model. (A) The electron temperature measured using Tr-ARPES in comparison with the simulation results from TTM for the top 1nm thick layer of Ni with different pump fluence. (B) The transient EUV reflectivity results in comparison with the TTM simulation considering the average over a EUV probing depth of ≈ 10 nm. (C) The electron temperature simulated by TTM considering the situations: 1) thermally isolated, same as Eq. 4.1; 2) only heat diffusion; 3) heat diffusion + e-ph coupling. The dashed line represents the simulation results convolved with the experimental time resolution.

Chapter 5

Quantitative Correlation of Extreme Ultraviolet Magneto-Optic and Photoemission Spectroscopies

In this chapter, we investigate the ultrafast magnetic phase transition in Ni using time-resolved transverse-magneto-optical Kerr effect (TR TMOKE) spectroscopy based on high harmonic generation. Using the critical behavior and the timescales of demagnetization and recovery processes observed from TR ARPES, and by taking the depth-dependent signal contributions in TR TMOKE into account, we show that critical phenomena are also key for the correct interpretation and a full understanding of ultrafast optical or x-ray magnetic spectroscopies. With this knowledge, we can now fully explain the TR-TMOKE response of Ni over the full range of laser fluences, using only three universal timescales to describe the demagnetization and recovery dynamics in distinct physical regions. Although the spin system absorbs all the energy required to proceed through a magnetic phase transition within 20 fs, the spectroscopic signatures of demagnetization take 176 fs to develop. Moreover, these timescales are fluence independent. In contrast, the speed of remagnetization dynamics depends on whether the applied laser fluence is below or above the critical fluence. Our data show that the demagnetization amplitudes scale linearly with pump fluence. Finally, we observe a competition between the fast and slow recovery channels with distinct timescales, suggesting a potential coexistence of ferromagnetic and paramagnetic phases during the phase transition.

A schematic of the physics studied in the experiment is shown in Fig. ???. The sample used in our experiments was a 400 nm Ni(111) single-crystal film. We intentionally chose a thick film

sample to minimize nonlocal effects due to interfaces or poor substrate thermal conduction [29,30] and also verified that the observed dynamics were not dependent on the orientation of the sample (see the Supplemental Material [31]). In both the TR-TMOKE and TR-ARPES experiments, the sample was excited by 45 fs pulses from a Ti:sapphire laser amplifier system at a wavelength of 800 nm. In the TR-TMOKE measurements, the subsequent change of the sample magnetization was probed by extreme ultraviolet (EUV) pulses produced by high harmonic generation (HHG). The sample magnetization can be quantitatively determined by recording the asymmetry of the reflected HHG spectrum at the 3p edge of Ni [6,7,11]. In the TR-ARPES measurements, the magnetization dynamics was probed by monitoring the magnitude of the exchange splitting at different time delays [2,8,27].

In order to determine if Tr-TMOKE and Tr-ARPES give spectroscopic signatures that are consistent with the same microscopic physics and interactions, we measured the de- and remagnetization dynamics in Ni excited by a wide range of fluences, with the highest fluence sufficient to fully suppress the TR-TMOKE asymmetry (i.e., demagnetize the sample). The pump penetration depth in Ni is $\delta L \approx 13$ nm [41], which is comparable to the probing depth of the EUV light used in the TR-TMOKE experiments (10 nm). In contrast, the probing depth of photoelectrons is close to a monolayer for the photon energy (16 eV) used in the TR- ARPES experiments [42], which suggests that the TR- ARPES signal can probe the elementary magnetization dynamics in an individual surface layer of the sample. In Fig. ??(b), we conceptually summarize the electron, spin, and magnetization dynamics after laser excitation, with the critical behavior taken into consideration [27].

In Fig. 5, we plot the change of the exchange splitting (ΔE_{ex}) at the transverse momentum $k \approx 1.05 \text{ \AA}^{-1}$ along the $\Gamma - K$ direction of Ni (inset of Fig. 5) observed in the TR-ARPES measurements [27]. Due to <1 nm probing depth, TR ARPES probes the elementary magnetization dynamics in a monolayer of the material, which can be well described by an exponential decay and biexponential recovery function as shown in Fig. 5:

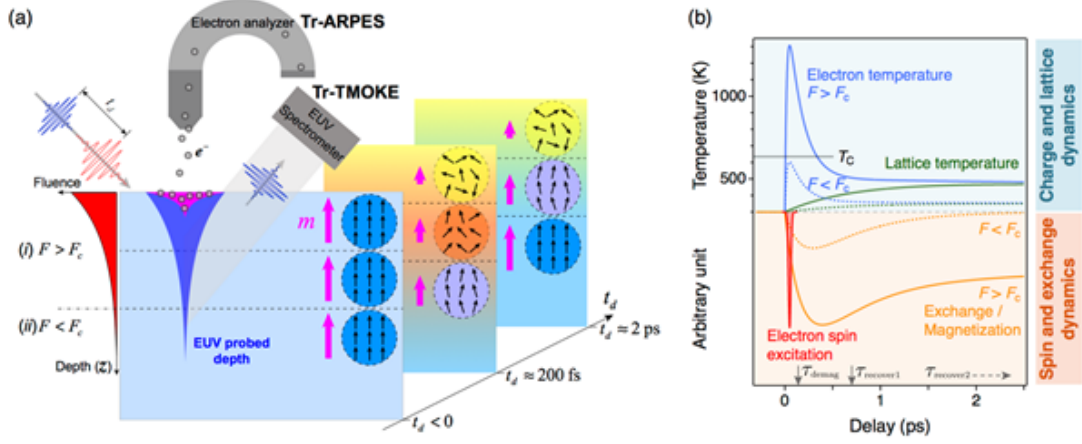


Figure 5.1: (a) Schematic of EUV ARPES and TMOKE measurements on Ni(111). The fluence profile of the laser excitation below the sample surface separates the magnetization response into two different regions (i) and (ii), depending on whether the in-situ fluence is above the critical fluence F_c . Using TR ARPES, the probed depth is on the order of a monolayer, while TR-TMOKE probes the entire laser-heated depth of ≈ 10 nm. (b) Schematic of the excitation present in the laser-induced phase transition in Ni when critical phenomena are taken into consideration [27]. When the laser fluence exceeds the critical fluence F_c , the electron temperature exceeds T_c and the sample rapidly undergoes a magnetic phase transition, as evidenced by multiple critical phenomena.

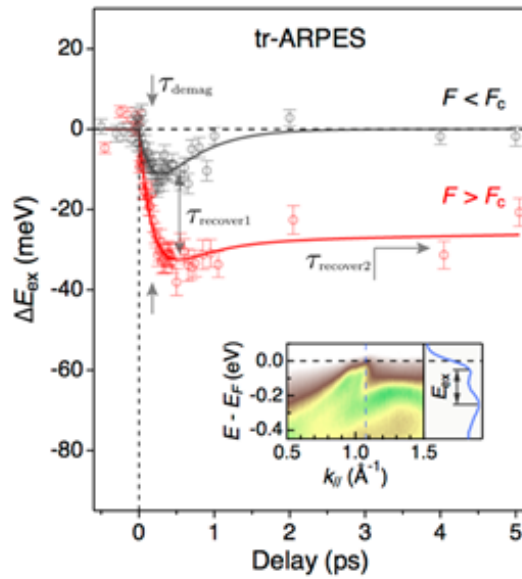


Figure 5.2: Change in the exchange splitting (ΔE_{ex}) in Ni measured using TR ARPES, for the absorbed laser fluence below ($0.21 \text{ mJ} = \text{cm}^2$, grey) and above ($1.7 \text{ mJ} = \text{cm}^2$, red) the critical fluence F_c . The solid lines are the fits to Eq. 5. Inset: Static ARPES spectrum plot along the Γ -K direction recorded using He I_α photons.

$$Y(t_d) = \begin{cases} 1 & (t_d < 0) \\ 1 + a_1(z)e^{-t_d\tau_{demag}} - a_2(z)e^{-t_d\tau_{recover1}} - a_3(z)e^{-t_d\tau_{recover2}} & (t_d \geqslant) \end{cases}$$

Here we obtain three time constants that correspond to the following physical processes: the collapse of the exchange splitting $\tau_{demag} = 176 \pm 27$ fs, a fast recovery time $\tau_{recover1} = 537 \pm 173$ fs, and a slow recovery time [31] for data supporting the extraction of the time constants. $\tau_{recover2} = 76 \pm 15$ ps [27]. See the Supplemental Material In Eq. , a_1 , a_2 , and a_3 are the amplitudes of these amplitudes are independent since the magnetization will processes, with $a_1 = a_2 + a_3$. Note that only two of the recover fully at long times. Their values depend on the strength of the laser fluence and, hence, are depth dependent due to the profile of the optical pump below the sample surface [Fig. 5(a)]. From the ARPES results, we map the dynamics in monolayers of the materialwe can now test whether this understanding can fully explain the TR- TMOKE results.

The magnetization dynamics in the same sample excited by fs laser irradiation were also measured using TR TMOKE. In the inset of Fig. 5, we present the bulk-averaged hA2i, and hA3i) as a function of pump fluences, by fitting averaged amplitudes of de- and remagnetization ($\langle A_1 \rangle$, $\langle A_2 \rangle$, $\langle A_3 \rangle$) as a function of pump fluences, by fitting the TR-TMOKE results presented in Fig. 5 with the same exponential decay and bi-exponential recovery function. Here the amplitudes represent the change of the sample magnetization normalized to the magnetization of the ground state. Even from the raw data traces, the presence of three timescales is very apparent: a fast and universal demagnetization time followed by fast and slow recoveries depending on the fluence. From these results, we find that the slow-recovery process ($\langle A_3 \rangle$) only turns on when the absorbed laser fluence (F_{abs}) is above the critical fluence ($F_c \approx 0.59$ mJ/cm²), which highlights the importance of the critical behavior to the interpretation of the Tr-TMOKE results (Note that in [25] we quoted the incident fluence of 2.8 mJ/cm², which is consistent with an absorbed fluence of 0.59 mJ/cm² within error bars). Moreover, a linear response of the slow-recovery amplitude can be clearly observed, as highlighted in the inset of Fig. 5.

Under the assumption of linear absorption, in both experiments the in-situ laser fluence F

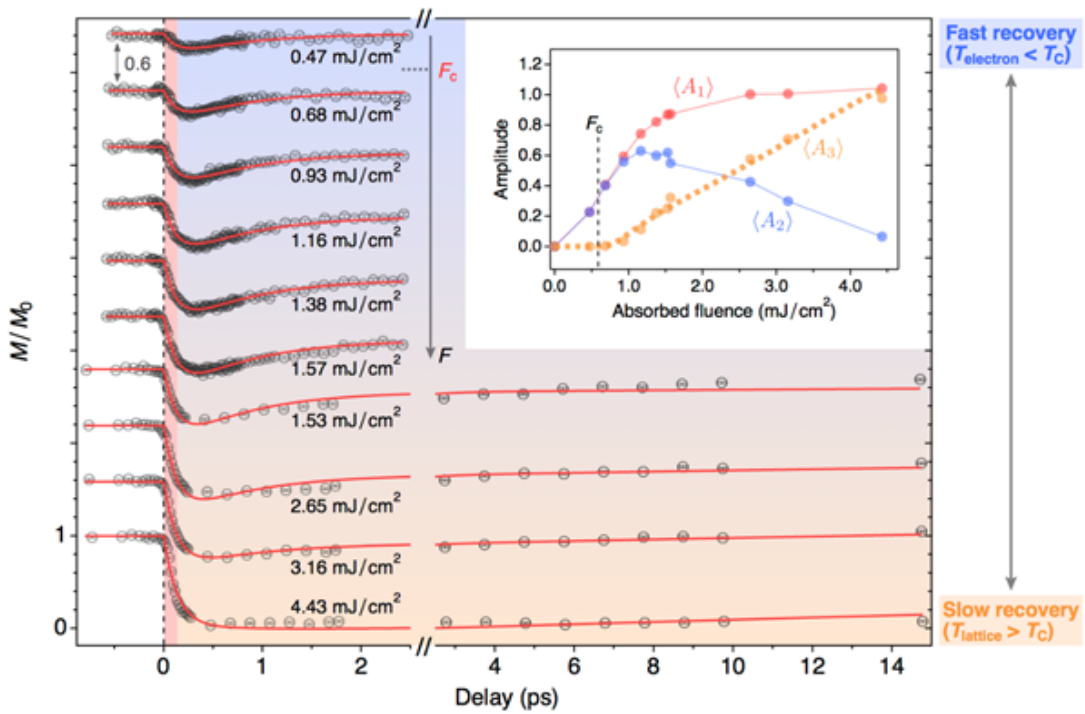


Figure 5.3: Magnetization dynamics in Ni measured using TRTMOKE over a full range of laser fluences. The highest fluence is sufficient to fully suppress the sample magnetization. The data are offset for clarity. Red curves: Fits to our microscopic model which considers the critical behavior, as well as the depth-average effects in the TR-TMOKE measurements. Inset: Fluence-dependent amplitudes of the demagnetization and recovery processes directly extracted from the TR-TMOKE results. In the TR-TMOKE results, the magnetization $\langle M \rangle$ and the extracted amplitudes $\langle A_1 \rangle$, $\langle A_2 \rangle$, and $\langle A_3 \rangle$ are averaged over the entire probed depth (see text). The dashed yellow line highlights the linear relation of the amplitude $\langle A_3 \rangle$ to the absorbed fluence when the fluence is above the critical fluence.

decays exponentially with the depth z i.e. $F(z) = F_0 e^{z/\delta_L}$, where F_0 is the fluence at the surface. To take into account the true absorption at different depths, the heat source q can be calculated by $q(z) = F(z)/\delta_L$. When $F_0 > F_c$, the Tr-TMOKE signal arises from different regions, each exhibiting different recovery dynamics depending on whether the laser excitation is above or below the critical fluence (Fig. 5a). In Region (i) where the in-situ fluence is always lower than the critical fluence, and the sample re-magnetizes through the fast recovery channel. In contrast, in Region (ii), the in-situ fluence is above F_c , and re-magnetization occurs through both slow and fast recovery channels. Here, we further assume that the change of magnetization is a linear function of the in-situ fluence, which is strongly supported by our experimental results (inset of Fig. ??) and previous work [28]. Given this linear relation, we have

$$a_1(z) = \min[b_1 F(z), 1] \quad (5.1)$$

and

$$a_3(z) = \begin{cases} 0 & [F(z) < F_c] \\ \min[b_3 [F(z) - F_c]] & ; [F(z) \geq F_c] \end{cases}$$

where b_1 and b_3 are the proportionality constants. The Tr-TMOKE signals can be modeled as the bulk-averaged magnetization $\langle M \rangle$, given by the integral of the unit magnetization $m(t_d, z)$ over the probed depth z :

$$\langle M \rangle (t_d) = \frac{\int_0^\infty m(t_d, z) W(z) dz}{\int_0^\infty W(z) dz} \quad (5.2)$$

Here, $W(z)$ is the depth sensitivity function of TMOKE [44], which is explicitly calculated for Ni (see the Supplemental Material [31] for details).

Using the model described above, we now fit the TR-TMOKE results for the different fluences shown in Fig. 5 to Eqs. 5 - ??, taking b_1 , b_3 , and F_c as the fitting parameters. We use the characteristic times obtained from the TR-ARPES measurements as the time constants in Eq. ??(see the Supplemental Material [31]). As shown in Fig. 5, there is excellent agreement between

the model (solid lines) and experimental data (symbols) over the full range of pump fluences, even though the limited number of fitting parameters places a strong constraint on our fitting. We note that the extracted value of F_c is in good agreement with values obtained from the TR-ARPES experiments [27], which further validates our model. From these results, we find that the apparent presence of a fluence-dependent remagnetization time is a direct result of the bulk-averaged signal in TR-TMOKE: the surface layers of the material undergo a phase transition and exhibit slow recovery dynamics, while layers deeper within the material do not undergo a magnetic phase transition and as a result, exhibit only fast recovery dynamics. We note that similar fluence-dependent remagnetization times have been often observed in previous TR-TMOKE experiments on ferromagnets these were interpreted as a frustration-induced slowdown of the spin dynamics [28] or were regarded as important evidence supporting the Elliott-Yafet spin-phonon interaction as the relevant microscopic mechanism [9,16]. In contrast, our model provides an alternative interpretation validated over the full demagnetization parameter space: there indeed exists a transient magnetic phase transition in Ni when the excitation laser fluence is higher than a critical value, which can completely explain the observed TR-TMOKE data. The optimum values of fitting parameters are listed in Table I.

From our model which correlates the TR-TMOKE and TR-ARPES results, we can extract the time- and depth- dependent magnetization dynamics in Ni. In Fig. 5(a), we plot the amplitudes of the exponential functions in Eq. 5 for a monolayer Ni as a function of the heat source. A complete temporal and spatial profile of the laser- induced ultrafast demagnetization in Ni is plotted in Fig. 5(b). Physically, the characteristic fast and slow recovery timescales ($\tau_{recover1}$ and $\tau_{recover2}$) indicate the existence of two distinct physical mechanisms. The fast remagnetization timescale ($\tau_{recover1}$) can be explained by the damping of magnons under the strong exchange field in Ni [28], which yields a damping time of 580 fs (see the Supplemental Material [31]), in quantitative agreement with the observed fast recovery timescale ($\tau_{recover1}$, within experimental error) [27]. On the other hand, from molecular field theory, the exchange field is dissolved when the sample crosses the critical point and enters the paramagnetic state. In this case, we can expect the damping time

to approach infinity and cooling of the spin system can only be achieved via other mechanisms, e.g., coupling to the lattice and thermal transport. The latter is consistent with the appearance of the slow remagnetization process ($\tau_{recover2}$), when the fluence is above the critical fluence. As a result, the distinct timescales in our ultrafast measurement provide a way to probe the exchange field present on microscopic scales. Our results, hence, suggest the competition and coexistence of paramagnetic (slow recovery) and partially suppressed ferromagnetic (fast recovery) phases during the ultrafast demagnetization process, as well as the variation of their relative contributions as a function of pump fluence [Fig. 5(c)]. Indeed, it has been shown by simulations based on atomic level classical spin Hamiltonian that the recovery from a highly disordered magnetic state involves the growth of many small magnetically ordered and disordered regions, with a size comparable to the magnetic correlation length [28]. Very interestingly, the fluence for which the fast-remagnetization contribution completely disappears [F_c' in Fig. 5(a)] coincides with the fluence that drives the lattice temperature above the Curie temperature (see the Supplemental Material [31]). This is consistent with the thermodynamic limit. We note, however, that we cannot simply conclude that the variation of sample magnetization is only determined by the temperature of electron-lattice system. One obvious evidence is that the magnetization at long delay times (a3) increases linearly as a function of the laser fluence (and, hence, of the temperature), as shown in Fig. 5(a); this cannot be explained by the typical nonlinear relationship between the sample magnetization and temperature under thermal equilibrium conditions (see the Supplemental Material [31]). This result suggests that the spin system is far from thermal equilibrium on time-scales of picoseconds, a finding which is consistent with previous theory [28]. By separating the different d.o.f. in the time domain, our results suggest that the single critical point under thermal equilibrium is expanded into a critical region for the nonequilibrium magnetic phase transition in Ni [Fig. 4(a)], spanning critical fluences that first drive the electron temperature above the Curie temperature (F_c) and then the lattice to the Curie temperature (F_c').

Finally, another interesting conclusion we can make from our work is how to achieve very fast manipulation of spins, which has been an important goal ever since the first observation of ultrafast

demagnetization [1]. The fundamental speed of the demagnetization process we study is limited by the slow recovery dynamics, which typically occur on picosecond-to-nanosecond timescales [111]. From our data, one way to achieve faster all-optical spin control on sub-ps timescales is to apply a laser fluence lower than F_c to take advantage of a faster recovery timescale although in this case, the maximum demagnetization is <50% in Ni, as shown in Fig. 5(a). Another alternative would be to use a nanostructured magnetic material, with adjustable magnetic interactions and more optimal thermal transport.

In conclusion, we show that by correlating TR-ARPES and TR-TMOKE measurements on Ni, we obtain new insights into the laser-induced magnetic phase transition. All results consistently reveal a critical behavior associated with a true magnetic phase transition and universal timescales for spin excitation, demagnetization, and recovery. Moreover, the linear response and two competing channels observed in the recovery process suggest the possible presence of coexisting phases in the material.

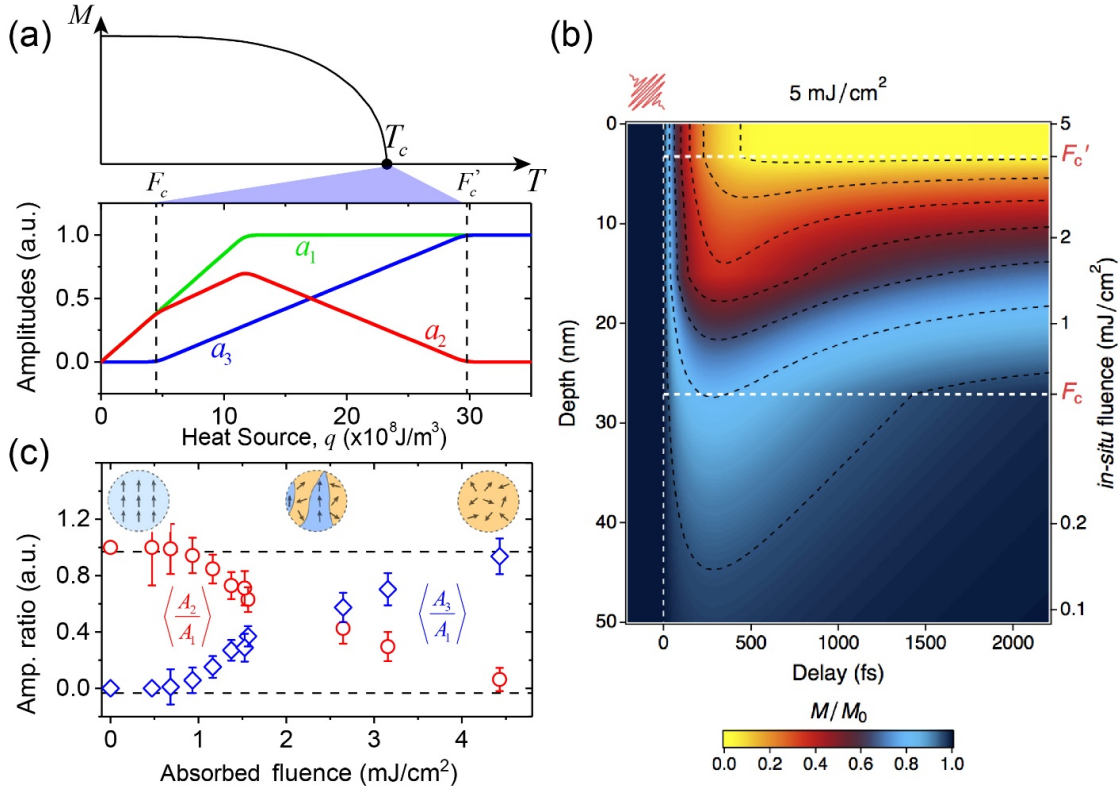


Figure 5.4: (a) Top panel: Schematic magnetization of a ferromagnet as a function of temperature under thermal equilibrium with a single critical point (T_c). Bottom panel: Extracted amplitudes of the change of magnetization in a monolayer of Ni as a function of in-situ fluence and heat source. The correspondence of T_c to the two critical fluences (F_c and F_c') is highlighted. (b) The laser-induced magnetization variation in Ni as a function of time and depth. The black dashed lines represent the contours of equal magnetization. The white dashed lines separate different regions for the in-situ fluence relative to the two critical fluences F_c and F_c' . (c) The relative contributions of the fast ($\langle A_3 \rangle$) recovery process directly extracted from the TR-TMOKE results in Fig. 5. Inset: Potential scenarios for the coexistence of ferromagnetic and paramagnetic phases in different fluence regions.

Chapter 6

Direct light-induced spin transfer between elemental sublattices in a spintronic Heusler material via femtosecond laser excitation

Ultralow-power, high-performance nonvolatile memory and logic devices based on magnetic spin (spintronics) are starting to make inroads into conventional computing and represent prime candidates for practical quantum technologies. However, fully exploiting the capabilities of new materials and technologies will require a detailed understanding of the underlying physics, as manifested by nanoscale dynamic magnetization properties. At present, our understanding of spin interactions is crude and predominantly phenomenological: a comprehensive, self-consistent, microscopic model that rigorously includes the spin, electronic, photonic and phonon-degrees of freedom and their interactions does not yet exist. This understanding is fundamentally constrained in large part by a limited ability to directly observe magnetism on all relevant time and length scales. While the fundamental length- and time-scales for magnetic phenomena are nanometers (exchange length) and femtoseconds (exchange splitting), tools that enable the exploration of dynamics at these scales have only recently become available.

Band structure engineering can significantly enhance the capabilities of quantum materials by controlling their magnetic and transport properties [2, 3]. One particular focus is the development of materials with the ability to efficiently generate and sustain pure spin currents for use in spintronics devices. Half-metallic Heusler compounds are particularly promising candidates for this application due to their unique band structure [4, 5]: one spin-channel (the majority band) is metallic in nature, but the other spin-channel (minority) is insulating, with a band-gap at the Fermi energy (see Fig.

1). This property is of intense interest for spintronics applications because it enables spin-based logic devices such as transistors, diodes, and gates [6]. It also puts unique restrictions on the spin excitation pathways that can be driven by a coherent laser pulse in each element of the compound, which can lead to exciting new dynamics, such as manipulating the magnetic state of elements in a compound ([7, 8]). Although all-optical switching has been demonstrated experimentally in both ferrimagnetic and ferromagnetic materials using circularly and linearly polarized light, the response of the material is not instantaneous, but takes place on picosecond timescales long after the laser excitation pulse [9], and in some cases also requires the cumulative effect of many pulses [10, 11].

To date, researchers have investigated several Heusler alloys using ultrafast femtosecond laser pulses to drive the system into a nonequilibrium state while monitoring the response of the system with magneto-optics [4, 5, 8, 12]. These experiments can help to reveal the rate at which the total magnetization dynamics evolve in a material and estimate how different microscopic mechanisms contribute, driving further development of functional materials. However, visible lasers probe the net magnetization averaged over all elements in the material. Very recent theoretical papers exploring laser-excited Heusler compounds have suggested the possibility of light-induced spin transfer from one element to another on extremely fast (<10 fs) timescales [13, 7]. This could in theory enable the ultimate goal of ultrafast direct optical manipulation of the magnetic state of a material, provided these dynamics can be observed.

Ultrafast extreme ultraviolet (EUV) high harmonic pulses make it possible to uncover the element-specific spin dynamics in multi-component magnetic systems, providing rich new information not accessible using visible light. Recent work has explored ultrafast laser-induced spin dynamics in ferromagnetic alloys and multilayers, where distinct responses such as the existence of a time lag between the quenching of the magnetization of different elements in an FeNi alloy were observed [14]. Other recent work has shown that light-induced spin dynamics in simple ferromagnets can occur on timescales ten times faster than previously suspected, within tens of femtoseconds [15, 16].

In this chapter, we show that a single ultrafast laser pulse can directly transfer spin po-

larization from one magnetic sublattice to another in the half-metal heusler compound Co_2MnGe within 55 fs. Using extreme ultraviolet high harmonic light resonant at the 3p edges of cobalt and manganese to measure the transverse magneto-optical Kerr effect of each element simultaneously and independently, we observe a surprising disparity between the response of the two magnetic sublattices: the magnetization of cobalt is transiently enhanced during the laser pump pulse, while that of manganese quenches rapidly. This extremely fast enhancement of the average magnetization of Co represents the fastest change in magnetization observed to date and is a unique property that stems from the half-metallic nature of the Heusler material. Through density functional theory (DFT) calculations [17, 18], that compute the density of states for each element in the compound, we show that optical excitations are preferentially enhanced in the majority spin channel of Mn and in the minority spin channel of Co. This imbalance of allowed excitation pathways for each element then induces a direct and instantaneous transfer of spin polarization from Mn sites to Co sites that occurs during the entire duration of the laser pulse. As a control, we observe no enhancement of magnetization or transfer of spin polarization in the disordered non-half-metallic (A2) phase of the same material. This is consistent with electronic structure theory that does not support any imbalance in the excited spin population of manganese in this phase. The observed transient enhancement of ferromagnetic ordering demonstrates direct manipulation of spins via light, thus providing a path towards spintronic logic devices such as switches that can operate on few femtosecond or even faster timescales. It also establishes band structure engineering as an efficient method of selecting for specific desirable behaviors in a quantum material.

Figure 6A illustrates the ultrafast spin dynamics that occur in the B2 (semi-ordered) half-metallic phase of Co_2MnGe . Before the pump pulse arrives, the material is ferromagnetically ordered, with a B2 structure (the CsCl structure), where Co occupies the corner sites, and the body centered position is randomly occupied by Mn or Ge. Note that the Mn atoms carry $\approx 3x$ as much magnetic moment as the Co atoms. As shown in Figs. 1 and 2, within the timescale of the laser pump pulse, there is a direct transfer of magnetization from the Mn atoms to the Co atoms: the magnetization of the Mn atoms decreases, while the magnetic moment of the Co

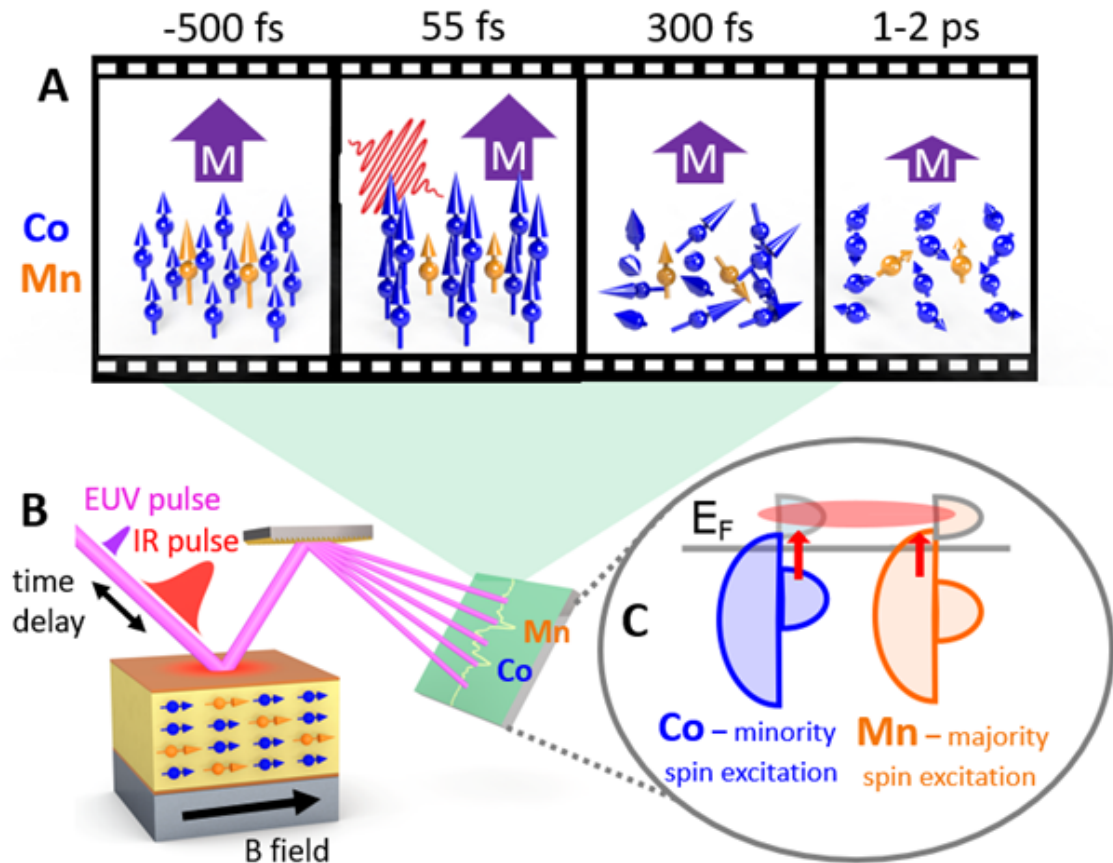


Figure 6.1: (A) Representation of spin dynamics in Co_2MnGe . Before excitation, Mn atoms (orange arrows) have a 3x larger magnetic moment than Co atoms (blue arrows), which are 2x more abundant in the bcc lattice. The purple arrow represents the net magnetic moment of the compound. Upon excitation, the Mn moment begins to decrease and the Co magnetic moment immediately grows by 10%. This occurs within the duration of the pump pulse. Hundreds of femtoseconds later, the Mn and Co atomic spins become disordered, and the angular momentum begins to transfer to the lattice. The net magnetic moment begins to decrease. After 1-2 ps, the spins have reached their maximum quenching. (B) Schematic of the experimental apparatus. Ultrafast femtosecond infrared pulses are used to excite the sample, while the magnetization dynamics are tracked with femtosecond EUV pulses recorded on a spectrometer. (C) Density of states for each element in the half metal. Note that the minority spin channel is gapped, with no available states at the Fermi level for the minority channel. Critically, this gap is larger for Mn than for Co. After excitation, the conduction band states are hybridized, as illustrated by the shared red wavefunction.

atoms increases. After the pump pulse, the material continues to demagnetize, dissipating the angular momentum into the lattice within a ps, with a \approx 120 fs lag between the response of Mn and Co. We emphasize that the initial magnetic response of the system is completely dominated by a direct optical excitation process, while rotation of atomic magnetic moments enters at a second stage. This is corroborated by a theoretical analysis based on the atomistic Landau-Lifshitz-Gilbert equation [19] (presented in the supplementary information), that fails to describe the initial phase of the magnetic response (< 250 ps) but provides the correct trend for longer time scales (> 500 fs).

Figure 6B shows the experimental setup used to simultaneously measure the response of Co and Mn after ultrafast excitation. We excite the sample with an infrared laser pulse with a photon energy of 1.55 eV and 55 fs full width half maximum (FWHM) in duration. To record the magnetic response, part of the laser light is directed into a He-filled hollow waveguide to generate 10 fs high harmonic EUV pulses that are simultaneously resonant with the 3p edges of Co (59 eV) and Mn (47 eV). The EUV transverse magneto optical Kerr effect (TMOKE) signal is constructed by a differential asymmetry [A] measurement with $A = \frac{I_+ - I_-}{I_+ + I_-}$ where I_+ and I_- are the intensities of the EUV light that is reflected from the sample for opposite directions of magnetization. The responses from individual elements are separated via a spectrometer. A more detailed schematic of the experimental layout is given later in the chapter.

Figure 6A plots the experimentally measured asymmetry of Co and Mn in the half-metallic B2 phase as a function of pump probe time delay. During the laser pulse, the Co magnetization transiently increases by $\approx 10\%$, while that of Mn immediately decreases. Although the initial dynamics are markedly different, the decay rates of the two magnetic sublattices are similar, and occur on timescales similar to the average values measured by visible MOKE [5]: Mn demagnetizes with an exponential decay constant of 328 ± 37 fs while Co does so with a decay constant of 323 ± 86 fs (after a lag due to the initial transient enhancement). As the timescale for this process is longer than in pure ferromagnets (see SI), we can unambiguously decouple the direct optically generated spin dynamics (that occur over the entire laser pulse duration of 55 fs) from the dissipation of angular momentum in the system (that follows in the next ps). As yet another control to test

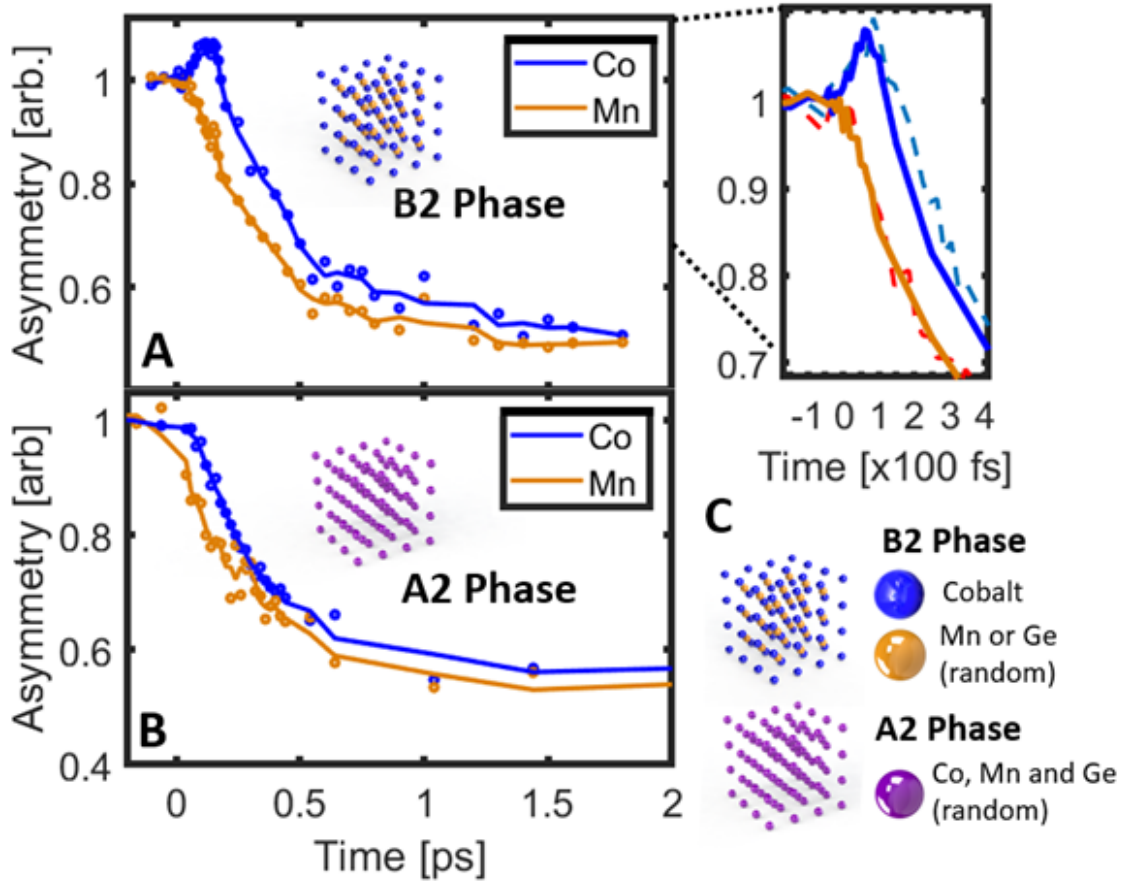


Figure 6.2: Element resolved ultrafast magnetization dynamics following excitation by femtosecond laser in the (A) half-metallic B2 phase. Note that the Co magnetization increases as the Mn decreases, followed by a lag of 100 fs between the demagnetization of the Co and Mn sublattices. Inset: Dynamics of ultrafast spin transfer. Solid lines are the element specific dynamics after excitation by a 55 fs (full width half maximum) pump pulse. Dashed lines indicate the dynamics after excitation by a 90 fs pump pulse. Note that the location of the peak of the enhancement is shifted in time by 25 fs for the enhancement driven by a 90 fs pump (half the difference between the duration of the two pulses), underlining that this process is a direct optical manipulation. (B) Element resolved ultrafast magnetization dynamics in the non half-metallic A2 phase. There is no enhancement of the Co magnetization. The subsequent lag in demagnetization dynamics between the Co and Mn sublattices decreases to 57 fs. (C) Atomic structure of compounds studied. In the B2 phase, the Co atoms have ordered so that they occupy sites at the edges of the bcc structure, while the centers are randomly interspersed between Mn and Ge. In the A2 phase, the material has formed the ordered bcc structure, but the location of the atoms within the structure are random.

the time sequence of spin transfer, we increased the pump pulse duration from 55 fs to 90 fs. As shown in dashed lines in the inset of Fig. 2A, this resulted in an increase of the delay in the demagnetization between the Co and Mn sublattices: from 120 ± 33 fs (55 fs pump pulse) to 157 ± 27 fs (90 fs pump pulse). This is consistent with a spin transfer process from Mn to Co that occurs only during the laser pump pulse.

Figure 6B plots the element specific dynamics in the metallic A2 phase of the material driven by a 90 fs excitation pulse. In this phase, the lag in response of the magnetic sublattices (Mn and Co) is much less, only 56 ± 32 fs, and no transient increase in the Co magnetization is observed. As discussed below and in the SI, this is because the optical pathways to excitation in the minority band of manganese is not blocked in this phase. Fig. 6C shows the elemental crystal structure of the material in the two phases studied (B2 and A2). The details of sample growth are given in ???. In contrast to the B2 phase, the A2 phase is disordered, does not have a half-metallic gap for the minority spin state (as shown in Fig. 3B), and serves as a control from which to understand the effect of half-metallicity on the element specific magnetization properties of Co_2MnGe .

It is clear from a comparison between the dynamics observed in the A2 and B2 phases that ordering and emergence of a half-metallic gap in the minority band play a fundamental role in the optical magnetic response of Co_2MnGe . The transient enhancement observed is a coherent process driven directly by the optical excitation pulse, as demonstrated by the shift in the peak of the Co excitation when driven by a longer laser pulse. Moreover, our measurements also show that elemental specificity is critical for revealing the underlying magnetic dynamics of this material: as shown in Fig. 6 and the SI, when the Co and Mn responses are averaged (as is the case for visible MOKE), no difference in the behavior of the A2 and B2 phases can be detected.

Figures 6A and B plot the element specific spin resolved density of states (DOS) calculated using DFT for the two phases of the material. In the B2 phase (Fig. 6A) a gap has formed for the minority carriers, while the majority has full mobility across the Fermi level. Critically, this gap is larger for the Mn states than the Co states. In contrast, the crystal has a fully metallic characteristic in the A2 phase (Fig. 6B) for both the majority and minority states. When a 1.55

eV IR photon is absorbed, the density of states of each phase results in several key differences in the transition probabilities for the material. As shown in Fig. 6 and the SI, in the B2 phase, most of the minority carriers that are excited come from Co states, but very few minority excitations can take place for Mn states. One must bear in mind that both initial and final states of this optical excitation involve wavefunctions that are shared across hybridizing Mn and Co orbitals. Due to an imbalance in how Co and Mn projected orbitals contribute to the initial and final states, direct and spin conserving transitions lead to an effective transfer of spin angular momentum from Mn to Co.

Figures 6A and B plot the calculated imbalance of the transition probabilities from each sublattice that give rise to the spin transfer from Mn to Co. The combination of these effects results in a direct transfer of spin polarization from Mn sublattices to Co as observed experimentally in the B2 phase and illustrated in Fig. 1C. In Fig. 6C, we illustrate the basic mechanism that allows for an effective angular momentum transfer from Mn d-states to Co d-states. The initial state wavefunction that is involved in the optical transition is hybridized and composed of both Mn and Co d-states, with a larger contribution from the Mn atom (initial state). For the final state, the situation is reversed, and the Co d-states dominate. Hence, when an electron is optically excited from the initial to the final state wavefunction, this is associated with a transfer of d-state population from Mn to Co. A higher probability of transitions for the spin-up electrons compared to the spin-down electrons in Mn (Fig. 6A) then causes an effective spin-transfer from Mn to Co, as observed in the data of Fig. 6A. In the A2 phase (Fig. 6B), excitation in the minority valence band of Mn is now optically allowed, and direct optical transfer of spin polarization does not occur (see SI for these calculations).

We emphasize that the transient enhancement of the magnetic signal shown in Fig. 6A for the B2 phase has no contribution from the change in refractive index due to electronic changes in the reflectivity. We demonstrate this by measuring the change in reflectivity for the B2 and A2 phases at the Co edge, and showing that the magnitude of these changes is equal in the two phases of the material (see SI for more information). The mechanism responsible for the magnetization dynamics of Co_2MnGe in the B2 phase involves direct optical transitions, that leads to an initial

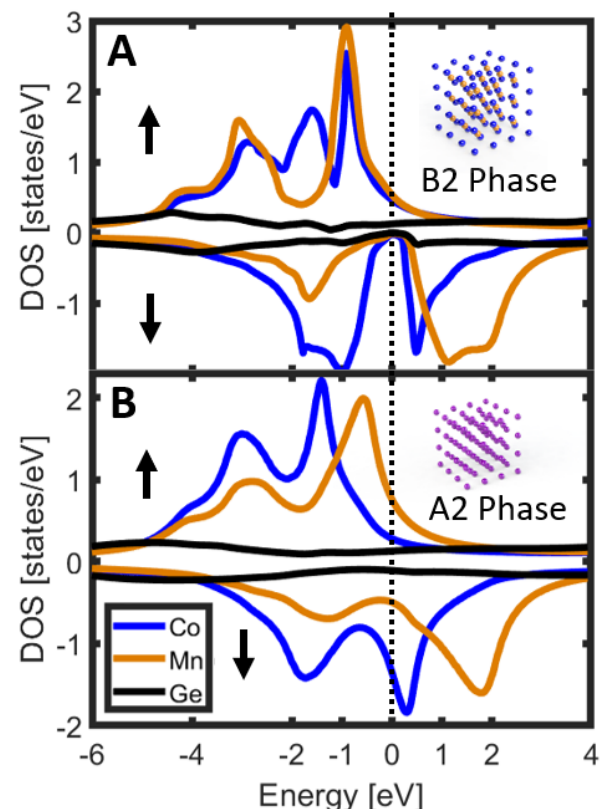


Figure 6.3: Density of states for Co_2MnGe in the (A) B2 and (B) A2 phases. Note that the half-metallic character is only present in the B2 phase.

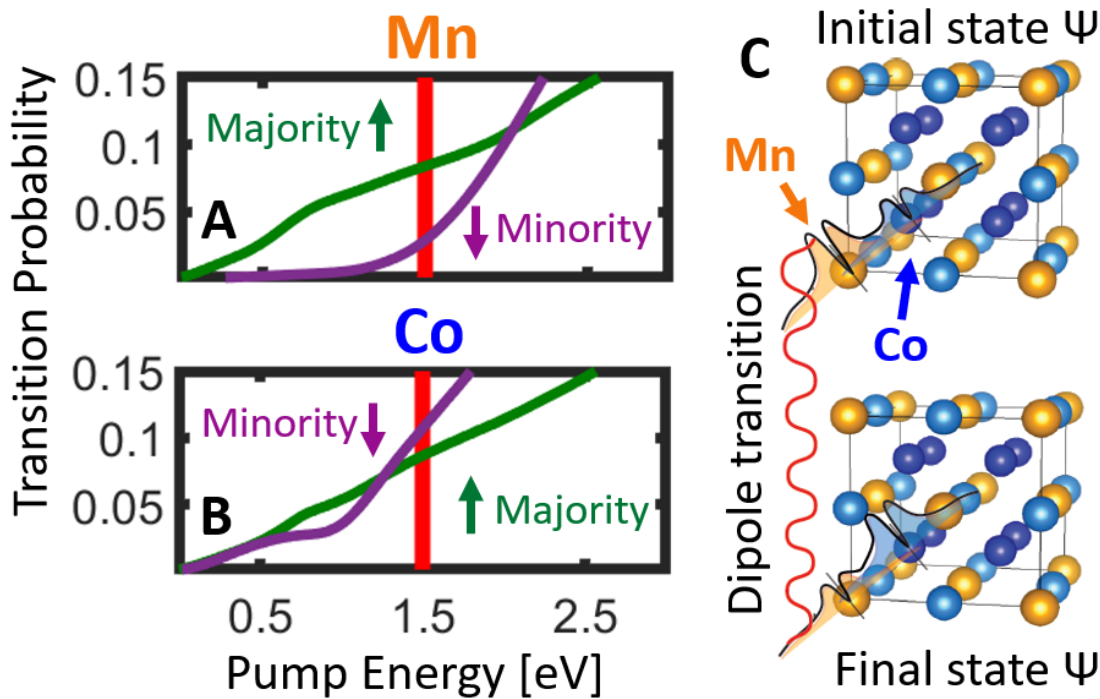


Figure 6.4: The probability for exciting a spin up (majority) vs. spin down (minority) electron from the valence band in the B2 phase for different pump energies in (A) Mn sites. Note that for a 1.55 eV pump, the probability is higher for spin up electrons to be excited from Mn. (B) Probability for excitations in Co sites. In contrast to the Mn result, the probability is higher for minority electrons to be excited in Co. (C) Illustration of process that leads to direct optical transfer of spin polarization from Mn to Co. The initial state wavefunction is hybridized and composed of both Mn and Co d-states, with a larger contribution from the Mn atom. In the final state, the situation is reversed, and the Co d-states dominate. Hence, when an electron is optically excited from the initial to the final state wavefunction, this is associated with a transfer of spin polarization from Mn to Co.

transfer of spin moment from Mn to Co. This purely electronic mechanism is necessary in addition to a description based on the atomistic Landau-Lifshitz-Gilbert (aLLG) equation, that sometimes is employed to analyze the kind of experiments presented here [20, 21]. As shown in the SI, the aLLG equation captures some features of the observed magnetization dynamics, especially at longer timescales (≈ 250 fs and longer), but it fails to explain the initial phase of the demagnetization process. We also note that a similar enhancement to that shown in Fig. 6A was predicted via time dependent DFT calculations for the related compound Co_2MnSi , with the mechanism in this case also attributed a transfer of spin polarization between Co and Mn[7].

Given that we now understand how to measure and predict all-optical spin transfer based on the electronic structure and the density of states of the material, future experiments can explore how changing the pump photon energy or tailoring the bandgap (i.e. density of states)[3] in other materials can be used to tune the demonstrated spin manipulation. Since the enhancement is only observed in the half-metallic phase of the material, the presence of the band gap in the minority channel of both elements may help to enable the spin polarization enhancement in Co; after majority electrons are excited in Mn and shared with Co via hybridized orbitals, these electrons may not be able to decay via spin-flip scattering into the minority band [8]. We also note here that the B2 phase of Co_2MnGe , where the large spin-transfer between two atom types is observed, is characterized by hybridizing states, as well as a low-spin state of one of the atoms (Co) that has a high spin state available at not too large energies. Indeed, Co occupies this higher spin state for the A2 phase. We speculate that these material characteristics are important when trying to find other materials that may have similar characteristics as those of Co_2MnGe and the results shown in Fig. 2A. The L21 phase shares these characteristics with the B2 phase of Co_2MnGe , and is therefore expected to have similar magnetization dynamics. There are several other materials that also have these characteristic properties. For instance, the meta-magnetic Laves phase YCo_2 , when doped with Fe or Ni, as well as fcc Fe doped with Co or Ni, are all systems that can be characterized in this way. Although direct spin transfer is likely the dominant mechanism in this material, we note that other sub 50 fs demagnetization mechanisms have recently been uncovered, and could cause different

kinds of spin dynamics that operate on the same timescales as direct spin transfer in these other materials [15, 16]. Finally we note that a similar lag in spin dynamics was previously observed in alloys of FeNi [14], therefore our element-resolved measurements of a lag in a fundamentally different system suggest that these phenomena may be ubiquitous.

Our time- and element- resolved EUV MOKE method will have useful applications for selecting spintronic materials, to understand which materials are good candidates for spin injection. In the past several decades, various techniques for spin injection have emerged, but all have degrees of spin polarization <100%. Pursuing the goal of a pure spin current source, ferromagnetic half-metals were developed to ideally provide conduction of a single spin state. However, 100% spin polarized conduction has not yet been demonstrated in these compounds [22]. Although many techniques are used to characterize the properties of half-metallic materials such as Andreev reflection [23, 24], spin-polarized tunneling, spin-polarized photoemission [25], and visible MOKE[4], these all rely on surface measurements. However, device applications require coherence and functionality through a finite nanoscale depth, and bulk and surface properties can be significantly different [26, 27, 28]. A strong advantage of using EUV MOKE as a probe of these materials is the larger penetration depth of EUV light, more than twice that of visible light, which can in addition to providing elemental specificity, probe the magnetization state of the material more deeply inside of a device. To utilize the potential of our findings in a functional spintronics device, the transfer of spin must occur across finite distances. According to DFT calculations, such a transfer process may be possible for a thin film stack [13]. Additionally, several new breakthroughs have recently reported miniaturizing spin current devices to the nanoscale [29, 30]. Considering these recent developments, we anticipate that the femtosecond spin transfer demonstrated in this work could be used for information processing utilizing spin currents on few fs timescales.

In conclusion, we experimentally demonstrate the first direct optical manipulation of the magnetic moment of an individual element in a compound material. Ultrafast transfer of magnetization takes place over sub-nanoscale spatial dimensions and sub-55 fs timescales. The timescale for transient enhancement depends on the duration of the excitation pulse, further confirming that

the light directly transfers the spin. Theory based on atomistic spin-dynamics as well as density functional theory show that electronic excitations drive the magnetization dynamics in the initial phase of the demagnetization, and that these excitations directly transfer spin from Mn to Co, via preferred spin-polarized excitation pathways. Rotation of atomic moments, as calculated by atomistic spin-dynamics and that result in significant non-collinear orientations, become relevant at a later stage of the dynamics. We confirm the predictions of the DFT calculations and importance of the half-metallic (B2) band structure of the material by a further lack of enhancement in the (A2) phase of the material (that lacks half-metallicity). This work represents the first optical manipulation of its kind and demonstrates a route to sub-femtosecond all-optical logical operations in magnetic recording media.

Bibliography

- [1] J.J. Sakuri. Modern Quantum Mechanics, Revised Edition. 1994.
- [2] Shikun He, Yifan Liu, Yuhong Zheng, Qing Qin, Zhenchao Wen, Qingyun Wu, Yi Yang, Yupu Wang, YuanPing Feng, Kie Leong Teo, and Christos Panagopoulos. Tunable magnetization relaxation of $\text{Fe}_2\text{Cr}(1-x)\text{Co}_x\text{Si}$ half-metallic Heusler alloys by band structure engineering. Physical Review Materials, 1(064401):064401, 2017.
- [3] P. Klaer, M. Kallmayer, C. G.F. Blum, T. Graf, J. Barth, B. Balke, G. H. Fecher, C. Felser, and H. J. Elmers. Tailoring the electronic structure of half-metallic Heusler alloys. Physical Review B - Condensed Matter and Materials Physics, 80(14):1–13, 2009.
- [4] Georg M. Müller, Jakob Walowski, Marija Djordjevic, Gou Xing Miao, Arunava Gupta, Ana V. Ramos, Kai Gehrke, Vasily Moshnyaga, Konrad Samwer, Jan Schmalhorst, Andy Thomas, Andreas Hütten, Günter Reiss, Jagadeesh S. Moodera, and Markus Münzenberg. Spin polarization in half-metals probed by femtosecond spin excitation. Nature Materials, 8(1):56–61, 2009.
- [5] Andreas Mann, Jakob Walowski, Markus Münzenberg, Stefan Maat, Matthew J. Carey, Jeffrey R. Childress, Claudia Mewes, Daniel Ebke, Volker Drewello, Günter Reiss, and Andy Thomas. Insights into ultrafast demagnetization in pseudogap half-metals. Physical Review X, 2(4):1–9, 2012.
- [6] Gary A. Prinz. Spin-Polarized Transport. Physics Today, 48(4):58–63, 1995.
- [7] P. Elliott, T. Müller, J. K. Dewhurst, S. Sharma, and E. K. U. Gross. Ultrafast laser induced local magnetization dynamics in Heusler compounds. Scientific Reports, 6(1):38911, 2016.
- [8] Daniel Steil, Sabine Alebrand, Tobias Roth, Michael Krau??, Takahide Kubota, Mikihiko Oogane, Yasuo Ando, Hans Christian Schneider, Martin Aeschlimann, and Mirko Cinchetti. Band-structure-dependent demagnetization in the Heusler alloy $\text{Co}_2\text{Mn}_{1-x}\text{Fe}_x\text{Si}$. Physical Review Letters, 105(21):17–20, 2010.
- [9] K C Kuiper, R R J C De Wit, B Koopmans, and A J Schellekens. Ultrafast spin-transfer torque driven by femtosecond pulsed-laser excitation. Nature Communications, 5:1–7, 2014.
- [10] C. H. Lambert, S. Mangin, B. S.D.Ch S. Varaprasad, Y. K. Takahashi, M. Hehn, M. Cinchetti, G. Malinowski, K. Hono, Y. Fainman, M. Aeschlimann, and E. E. Fullerton. All-optical control of ferromagnetic thin films and nanostructures. Science, 345(6202):1337–1340, 2014.

- [11] S. Mangin, M. Gottwald, C. H. Lambert, D. Steil, V. Uhlí, L. Pang, M. Hehn, S. Alebrand, M. Cinchetti, G. Malinowski, Y. Fainman, M. Aeschlimann, and E. E. Fullerton. Engineered materials for all-optical helicity-dependent magnetic switching. *Nature Materials*, 13(3):286–292, 2014.
- [12] Jan Peter Wüstenberg, Daniel Steil, Sabine Alebrand, Tobias Roth, Martin Aeschlimann, and Mirko Cinchetti. Ultrafast magnetization dynamics in the half-metallic Heusler alloy Co₂Cr_{0.6}Fe_{0.4}Al. *Physica Status Solidi (B) Basic Research*, 248(10):2330–2337, 2011.
- [13] John Dewhurst, Peter Elliott, Sam Shallcross, Eberhard K. U. Gross, and Sangeeta Sharma. Laser induced inter-site spin transfer. *Nano Letters*, 18:18421848, 2018.
- [14] S. Mathias, C. La-O-Vorakiat, P. Grychtol, P. Granitzka, E. Turgut, J. M. Shaw, R. Adam, H. T. Nembach, M. E. Siemens, S. Eich, C. M. Schneider, T. J. Silva, M. Aeschlimann, M. M. Murnane, and H. C. Kapteyn. Probing the timescale of the exchange interaction in a ferromagnetic alloy. *Proceedings of the National Academy of Sciences*, 109(13):4792–4797, 2012.
- [15] R. Gort, K. Bühlmann, S. Däster, G. Salvatella, N. Hartmann, Y. Zemp, S. Holenstein, C. Stieger, A. Fognini, T. U. Michlmayr, T. Bähler, A. Vaterlaus, and Y. Acremann. Early Stages of Ultrafast Spin Dynamics in a 3d Ferromagnet. *Physical Review Letters*, 121(8):087206, 2018.
- [16] Phoebe Tengdin, Wenjing You, Cong Chen, Xun Shi, Dmitriy Zusin, Yingchao Zhang, Christian Gentry, Adam Blonsky, Mark Keller, Peter M Oppeneer, Henry C Kapteyn, Zhensheng Tao, and Margaret M Murnane. Critical behavior within 20 fs drives the out-of-equilibrium laser-induced magnetic phase transition in nickel. *Science Advances*, 4(eaap9744):eaap9744, 2018.
- [17] P Hohenberg and W. Kohn. The Inhomogeneous Electron Gas. *Phys. Rev.*, 136(3B):B864–B871, 1964.
- [18] W. KOHN and L. J. SHAM. Self-Consistent Equations Including Exchange and Correlation Effects. *PHYSICAL REVIEW*, 140(4A):A1133–A1138, 1965.
- [19] O. Ericksson, A. Berman, L. Bergqvist, and J. Hellsvik. *Atomistic spin-dynamics; foundations and applications*. 2017.
- [20] R. F.L. Evans, U. Atxitia, and R. W. Chantrell. Quantitative simulation of temperature-dependent magnetization dynamics and equilibrium properties of elemental ferromagnets. *Physical Review B - Condensed Matter and Materials Physics*, 91(14):1–7, 2015.
- [21] M. Hofherr, S. Moretti, J. Shim, S. Häuser, N. Y. Safonova, M. Stiehl, A. Ali, S. Sakshath, J. W. Kim, D. H. Kim, H. J. Kim, J. I. Hong, H. C. Kapteyn, M. M. Murnane, M. Cinchetti, D. Steil, S. Mathias, B. Stadtmüller, M. Albrecht, D. E. Kim, U. Nowak, and M. Aeschlimann. Induced versus intrinsic magnetic moments in ultrafast magnetization dynamics. *Physical Review B*, 98(17):174419, 2018.
- [22] X. Y. Dong, C. Adelmann, J. Q. Xie, C. J. Palmstrøm, X. Lou, J. Strand, P. A. Crowell, J. P. Barnes, and A. K. Petford-Long. Spin injection from the Heusler alloy Co₂MnGe into Al_{0.1}Ga_{0.9}AsGaAs heterostructures. *Applied Physics Letters*, 86(10):1–3, 2005.

- [23] A.F. Andreev. The Thermal Conductivity of the Intermediate State in Superconductors. *Soviet Physics JETP*, 19(5):1228–1231, 1964.
- [24] Joern N. Kupferschmidt and Piet W. Brouwer. Andreev reflection at half-metal/superconductor interfaces with nonuniform magnetization. *Physical Review B*, 83(1):014512, 2011.
- [25] Z. Sun, Q. Wang, J. F. Douglas, H. Lin, S. Sahrakorpi, B. Barbiellini, R. S. Markiewicz, A. Bansil, A. V. Fedorov, E. Rotenberg, H. Zheng, J. F. Mitchell, and D. S. Dessau. Minority-spin t_{2g} states and the degree of spin polarization in ferromagnetic metallic La_{2-2x}Sr_{1+2x}Mn₂O₇(x = 0.38). *Scientific Reports*, 3:1–5, 2013.
- [26] J. J. Attema, L. Chioncel, C. M. Fang, G. A. de Wijs, and R. A. de Groot. Half-Metals: Challenges in Spintronics and Routes Toward Solutions. *Lect. Notes Phys.*, 678(January 2014):201–216, 2005.
- [27] M E Fisher. The theory of equilibrium critical phenomena. *Rep. Prog. Phys.*, 30:615–730, 1967.
- [28] T Pincelli, V Lollobrigida, F Borgatti, A Regoutz, B Gobaut, C Schlueter, T Lee, D J Payne, M Oura, K Tamasaku, A Y Petrov, P Graziosi, F Miletto Granozio, M Cavallini, G Vinai, R Ciprian, C H Back, G Rossi, M Taguchi, H Daimon, G Van Der Laan, and G Panaccione. Quantifying the critical thickness of electron hybridization in spintronics materials. *Nature Communications*, 8(May):1–8, 2017.
- [29] V. V. Kruglyak, S. O. Demokritov, and D. Grundler. Magnonics. *Journal of Physics D: Applied Physics*, 43(26):264001, 2010.
- [30] K. Wagner, A. Kákay, K. Schultheiss, A. Henschke, T. Sebastian, and H. Schultheiss. Magnetic domain walls as reconfigurable spin-wave nanochannels. *Nature Nanotechnology*, 11(5):432–436, 2016.